# Development of Next-Generation Data Processing for X-ray Space-Based Missions

**Dissertation**

der Mathematisch-Naturwissenschaftlichen Fakultät

der Eberhard Karls Universität Tübingen

zur Erlangung des Grades eines

Doktors der Naturwissenschaften

(Dr. rer. nat.)

vorgelegt von

Xianqi Wang

aus Hainan, V.R. China

Tübingen

2025

Gedruckt mit Genehmigung der Mathematisch-Naturwissenschaftlichen Fakultät der Eberhard Karls Universität Tübingen.

| | |
|---|---|
| Tag der mündlichen Qualifikation: | 18.06.2025 |
| Dekan: | Prof. Dr. Thilo Stehle |
| 1. Berichterstatter/-in: | Prof. Dr. Andrea Santangelo |
| 2. Berichterstatter/-in: | Prof. Dr. Klaus Werner |

路漫漫其修远兮，吾将上下而求索。

—*Li Sao*

Ich erkläre, dass ich die zur Promotion eingereichte Arbeit mit dem Titel “Development of Next-Generation Data Processing for X-ray Space-Based Missions” selbstständig verfasst, nur die angegebenen Quellen und Hilfsmittel benutzt und wörtlich oder inhaltlich übernommene Stellen als solche gekennzeichnet habe. Ich versichere an Eides statt, dass diese Angaben wahr sind und dass ich nichts verschwiegen habe. Mir ist bekannt, dass die falsche Abgabe einer Versicherung an Eides statt mit Freiheitsstrafe bis zu drei Jahren oder mit Geldstrafe bestraft wird.

| | |
|---|---|
| Ort/Place, Datum/Date | Unterschrift/Signature |

# Acknowledgements

The completion of this thesis would not have been possible without the help and support of many people. I would like to express my gratitude to all of them in the following paragraphs.

To start with, I would like to express my deep gratitude to Professor Andrea Santangelo for welcoming me into his group at IAAT, University of Tübingen, and for his support and advice throughout the thesis process.

I am sincerely grateful to Dr. Jan-Christoph Tenzer for his generous support, not only in providing academic guidance but also in offering invaluable assistance in various ways. I also appreciate his efforts in organizing cycling challenge, which added an extra layer of enjoyment to my doctoral study.

I would like to express my gratitude to Dr. Jörg Bayer for his unwavering support throughout my doctoral journey. His selfless assistance, whether in discussions on circuit designs, reviewing texts, or offering invaluable suggestions, has been immensely beneficial to me.

I would like to thank my office colleagues, my 'English teacher' Paul Hedderman, and my 'electronics teacher' Samuel Pliego Caballero. Your presence has made the office a lively and enjoyable place. I also cherish the unforgettable and delightful moments spent at the office and the beer garden next to the Neckar Bridge. And my new office mate, Christian Pommranz, for all the interesting discussions and shared experiences.

I would also like to thank Dr. Alejandro Guzmán Cabrera for his invaluable assistance in completing this thesis and for the many discussions and shared experiences.

I am also deeply grateful to all the students who have shared wonderful moments with me and supported me in our group over the past few years, including Heiko Salzmann, Enza Magaudda, Camille Diez, Inga Saathoff, Charles Thorpe-Morgan, Marvin Neumann, Moritz Klawin, Wilhelmina Joseph, Antonio Armeni, Bastian Heß, Hao Xiong, Artur Avakyan, Fabian Leuschner, etc.

I would like to thank my colleagues in the workshop for their contributions to the

machining work related to my thesis. I would also like to express my gratitude to Ms. Sabine Lauer, the secretary of our department, for her generous help and support.

Finally, I would like to thank my parents and family for their unwavering support, and my fiancée Chunyu Zhong for her love, support, and understanding.

*Xianqi Wang*
Tübingen, August 31, 2024

# Abstract

This thesis work is part of The enhanced X-ray Timing and Polarimetry Mission (eXTP), a space-based high-energy physics mission led by the Chinese Academy of Sciences (CAS) and co-participated by many European countries. It aims to explore celestial objects such as Black Holes (BHs) and Neutron Stars (NSs) through X-ray observations, and to measure the timing and polarization properties of the radiation they emit. To achieve this goal, the mission is equipped with four scientific instrument payloads. Among them, the Large Area Detector (LAD), as one of the important payloads contributed by Europe consortium, is a high-throughput instrument focusing on energy spectrum-timing research. The LAD utilizes state-of-the-art large-area Silicon Drift Detectors (SDDs). With the continuous advancement of detector technology, its dead time has been reduced to the nanosecond level, enabling the LAD to achieve exceptionally high time resolution in the detection of X-ray sources. To accurately handle the rapid output of high-throughput data, it is essential to develop corresponding data processing components to accommodate the high time resolution of X-ray detection. This thesis presents the development of the Panel Back-End Electronic (PBEE) for the data handling chain of the LAD instrument aboard the eXTP, as well as the testing of PBEE and energy calibration of the LAD's data handling chain.

The first part of the thesis focuses on the development of the PBEE of the LAD payload. Based on the systematic review of X-ray astronomical observation principles and the current state of high-energy detector technology, the LAD-PBEE is designed to fulfill the scientific objectives of the eXTP mission.

The second part systematically presents the testing of the LAD prototype. The PBEE system was functionally verified through integrated testing, and the experimental results demonstrated that the electronic system's performance indicators met the design specifications. During the 'first-light' testing phase, the initial spectral curve was successfully obtained, and spectral calibration was carried out based on the measured data.

This thesis is composed of 6 chapters. Chapter 1 provides an overview of the fundamental principles of X-rays and their detection technologies, along with a list of several representative high-energy astronomical missions. Chapter 2 discusses the core scientific objectives and overall mission design of the eXTP mission, with a focus on its key payloads. Chapter 3 examines the design details and technical implementation of the LAD, one of the payloads of the eXTP mission. Chapter 4 centers on the core work of this thesis—the development of the PBEE, covering hardware design, software development, and the creation of a communication protocol tailored for the LAD. Chapter 5 systematically introduces various testing activities for the PBEE, including electrical performance tests and functional verification tests. Additionally, this chapter details the debugging process of the LAD data handling chain and presents preliminary energy calibration results. Chapter 6, as the concluding section, provides a comprehensive review and outlook on the research content.

# Zusammenfassung

Diese Doktorarbeit ist Teil der enhanced X-ray Timing and Polarimetry Mission (eXTP), einer weltraumgestützten Hochenergiephysik-Mission unter der Leitung der Chinesischen Akademie der Wissenschaften (CAS) und mit Beteiligung zahlreicher europäischer Länder. Ihr Ziel ist die Erforschung von Himmelskörpern wie Schwarzen Löchern und Neutronensternen durch Röntgenbeobachtungen sowie die Messung der zeitlichen und Polarisations-Eigenschaften ihrer abgestrahlten Emission. Um diese Ziele zu erreichen, ist die Mission mit vier wissenschaftlichen Instrumenten als Nutzlast ausgestattet. Der Large Area Detector (LAD), ein wichtiger Beitrag eines europäischen Konsortiums, ist ein Instrument mit hohem Durchsatz für die Erforschung von Energiespektren und zeitlicher Variation. Der LAD nutzt modernste, großflächige Silizium-Drift-Detektoren (SDDs). Durch kontinuierliche Fortschritte in der Detektortechnologie wurde die Totzeit auf das Nanosekundenniveau reduziert, was dem LAD eine außergewöhnlich hohe Zeitauflösung bei der Detektion von Röntgenquellen ermöglicht. Um die schnelle Ausgabe der Hochdurchsatzdaten präzise zu verarbeiten, ist die Entwicklung entsprechender Datenverarbeitungskomponenten essenziell, um der hohen Zeitauflösung der Röntgendetektion gerecht zu werden. Diese Arbeit präsentiert die Entwicklung der Panel Back-End Electronic (PBEE) für die Datenverarbeitungskette des LAD-Instruments an Bord von eXTP, sowie die Tests der PBEE und die Energiekalibrierung der LAD-Datenverarbeitungskette.

Der erste Teil der Arbeit konzentriert sich auf die Entwicklung der PBEE für die LAD-Nutzlast. Basierend auf einer systematischen Übersicht über die Prinzipien der Röntgenastronomie und den aktuellen Stand der Hochenergie-Detektortechnologie wurde das Systemdesign der LAD-PBEE entworfen, um die wissenschaftlichen Ziele der eXTP-Mission zu erfüllen.

Der zweite Teil stellt systematisch die Tests des LAD-Prototyps vor. Das PBEE-System wurde durch integrierte Tests funktional verifiziert, und die experimentellen Ergebnisse zeigten, dass die Leistungskennwerte des Elektroniksystems die Designspezifikationen erfüllten. Während der ”First-Light”-Testphase wurde die erste Spektralkurve erfolgreich aufgenommen, und eine spektrale Kalibrierung wurde auf Grundlage der

Messdaten durchgeführt.

Diese Arbeit gliedert sich in 6 Kapitel. Kapitel 1 bietet einen Überblick über die grundlegenden Prinzipien von Röntgenstrahlung und deren Detektionstechnologien, zusammen mit einer Auflistung mehrerer repräsentativer Missionen der Hochenergieastronomie. Kapitel 2 erörtert die zentralen wissenschaftlichen Ziele und den gesamten Missionsentwurf der eXTP-Mission, mit einem Fokus auf ihren Hauptnutzlasten. Kapitel 3 untersucht die Designdetails und die technische Implementierung des LAD, einer der Nutzlasten der eXTP-Mission. Kapitel 4 konzentriert sich auf den Kernbeitrag dieser Arbeit – die Entwicklung der PBEE, einschließlich Hardware-Design, Software-Entwicklung und der Erstellung eines für den LAD maßgeschneiderten Kommunikationsprotokolls. Kapitel 5 führt systematisch verschiedene Testaktivitäten für die PBEE ein, einschließlich elektrischer Leistungstests und funktionaler Verifikationstests. Darüber hinaus beschreibt dieses Kapitel den Debugging-Prozess der LAD-Datenverarbeitungskette und präsentiert vorläufige Energieeichungsergebnisse. Kapitel 6, als abschließender Abschnitt, bietet eine umfassende Zusammenfassung und einen Ausblick auf den Forschungsinhalt.

# Acronym

**ADC** Analog-to-Digital Converter

**AGN** Active Galactic Nuclei

**ASI** Italian Space Agency

**ASIC** Application-Specific Integrated Circuit

**BEE** Back-End Electronics

**BH** Black Hole

**BHAD** Black Hole Accretion Disc

**BHXB** Black Hole X-ray Binarie

**CAE** French Alternative Energies and Atomic Energy Commission

**CAS** Chinese Academy of Sciences

**CBK PAN** Space Research Center of the Polish Academy of Sciences

**CCD** Charge-Coupled Device

**CMD** Telecommand

**CRC** Cyclic Redundancy Check

**DA** Detector Assembly

**DHU** Data Handling Unit

**DM** Detector Module

**EoS** Equation of State

**ECSS** European Cooperation for Space Standardization

**EGSE** Electrical Ground Support Equipment

**ESA** European Space Agency

**eXTP** The enhanced X-ray Timing and Polarimetry Mission

**FDIR** Failure Detection, Isolation, and Recovery

**FBK** Fondazione Bruno Kessler

**FEE** Front-End Electronics

**FoV** Field of View

**FPGA** Field Programmable Gate Array

**FWHM** Full Width at Half Maximum

**GEM** Gas Electron Multiplier

**GPD** Gas Pixel Detector

**GRB** Gamma-ray Burst

**GSPC** Gas Scintillation Proportional Counter

**HAC** High-accuracy Clock

**HK** Housekeeping

**HTRS** High Time Resolution Spectroscopy

**HV** High Voltage

**IAAT** Institute for Astronomy and Astrophysics in Tübingen

**ICU** Instrument Control Unit

**IPC** Imaging Proportional Counter

**IHEP** Institute of High Energy Physics

**INFN** Italian National Institute of Nuclear Physics

**INAF** National Institute for Astrophysics

**IR** Infrared

**IXPE** Imaging X-ray Polarimetry Explorer

**LAD** Large Area Detector

**LOFT** Large Observatory for X-ray Timing

**LVDS** Low-Voltage Differential Signaling

**MCP** Microchannel Plate

**MBEE** Module Back-End Electronic

**DM** Detector Module

**MOC** Mission Operation Center

**MPSU** Module Power Supply Unit

**MV** Medium Voltage

**NS** Neutron Star

**NSSC** National Space Science Center

**OBDH** Onboard Data Handling

**OGS** Operational Ground Segment

**OM** Optical Module

**PBEE** Panel Back-End Electronic

**PCB** Printed Circuit Board

**PDPU** Payload Data Processing Unit (S/C level)

**PDU** Power Distribution Unit

**PFA** Polarimetry Focusing Array

**PMT** Photomultiplier Tube

**PPS** Periodic Pulses per second

**PPSU** PBEE Power Supply Unit

**PSU** Power Supply Unit

**PUS-C** Packet Utilisation Service - C

**QCD** Quantum Chromodynamics

**QPO** Quasi-Periodic Oscillation

**S/C** Spacecraft

**SFA** Spectroscopy Focusing Array

**SDC** Science Data Center

**SDD** Silicon Drift Detector

**SGS** Science Ground Segment

**SMU** Spacecraft Management Unit

**SNR** Supernova Remnant

**SOC** Science Operation Center

**SSC** Science Support Center

**STROBE-X** The Spectroscopic Time-Resolving Observatory for Broadband Energy X-rays mission

**SVOM** Space Variable Objects Monitor

**ToO** Target of Opportunity

**TT&C** Telemetry, Tracking, and Command

**UART** Universal Asynchronous Receiver/Transmitter

**UV** Ultraviolet

**VHF** Very High Frequency

**VHDL** VHSIC Hardware Description Language

**WFM** Wide Field Monitor

**XRB** X-ray Binary

# Contents

# Introduction

Astronomy can be traced back to the dawn of human civilization, when ancient peoples turned their gaze to the vast night sky, relying solely on the naked eye to observe its celestial objects. However, modern urban light pollution obscures the night sky, making it difficult for contemporary observers to appreciate the stellar visibility experienced by ancient civilizations. As one of the oldest natural sciences, astronomy retains clear traces of its ancient origins: from prehistoric rock art to historical texts, civilizations systematically documented celestial phenomena. Beyond documentation, these societies applied celestial observations to practical purposes—developing calendars for agriculture and using stellar motions for navigation, thereby integrating cosmic patterns into societal organization.

China has a long tradition of systematic astronomical observation; as early as the Warring States Period (4th century BCE), astronomers documented detailed records of astronomical phenomena. Furthermore, nearly every Chinese dynasty thereafter established specialized astronomical bureaus. Although these institutions primarily fulfilled political and astrological functions, their existence underscores the central role of astronomy in imperial governance and cultural life. Etymologically, the term 'astronomy' is derived from the Greek words *astron*, meaning 'star', and *nomos*, meaning 'law'. This indicates that ancient astronomers recognized the motions of stars in the sky are not random but governed by specific laws. This recognition laid the groundwork for the discipline' s scientific evolution: the ancient Babylonians were among the first to formalize astronomy as a mathematical science, developing frameworks to explain the laws underlying celestial motion, and this approach was later further refined and advanced in ancient Greece.

Today, astronomy has matured into a fundamental scientific discipline, applying mathematics, physics, and chemistry to study the origin and evolution of celestial objects. It employs cutting-edge technologies to collect and process full-spectrum electromagnetic radiation and other cosmic messengers (e.g., neutrinos, gravitational waves), thereby continuously refining and transforming our understanding of the cosmos. As a leading frontier of contemporary natural science, astronomy captures electromagnetic radiation across an exceptionally broad energy range—from below

$10^{-4}$ eV in the radio band to over $10^{9}$ eV in the gamma-ray region. The energy range of X-rays is from 0.1 to 100 keV, usually expressed as a wavelength range of 0.01 to 10 nm.

X-ray astronomy, a specialized branch of this field, studies high-energy phenomena and extreme environments, thereby illuminating the evolution of stars, galaxies, and the cosmos. Due to their short wavelengths, X-rays reveal physical phenomena undetectable at other wavelengths, effectively opening a window to a 'hidden universe' . Through X-ray observations, scientists study extremely hot and energetic processes that are inaccessible at other wavelengths. Its primary observational targets include compact celestial bodies such as BHs, NSs, and Active Galactic Nucleis (AGNs), Supernova remnants, X-ray Binary systems, as well as Galaxy clusters.

X-ray astronomical observations began in the 1960s. Prior to this period, it was known that the Sun emits radiation across nearly all wavelengths; however, atmospheric absorption prevented ground-based X-ray observations. It was only with the advent of rockets and balloons that cosmic X-ray observations became feasible. Later, stable satellite platforms enabled longer observations and the ability to host more instruments, providing astronomers with powerful tools for X-ray exploration.

In recent decades, numerous X-ray observatories have been launched, and eXTP —a next-generation mission jointly developed by China and Europe—is scheduled to join them. The University of Tübingen has been actively involved in the eXTP project, contributing two advanced instruments: the LAD and the Wide Field Monitor (WFM), whose design concepts are inherited from the earlier Large Observatory for X-ray Timing (LOFT) project. This thesis focuses on this contribution, with its core investigation centered on the design and development of the PBEEs. Notably, the development of the PBEE for the LAD, led by IAAT, represents a key contribution to future X-ray missions and forms the central focus of this thesis. Additionally, the PBEE concept which was realized and tested in this work is also a part of this development project at IAAT.

# 1 X-Ray Astronomy

The main motivation for X-ray astronomy is that the most violent and energetic extreme events in the universe emit X-rays. These events either release extremely high total energy, such as supernova explosions and radiation from active galactic nuclei, or the matter involved is extremely hot or the energy of individual nucleons is extremely high, such as matter falling into black holes, hot plasmas, and relativistic interactions of electrons with magnetic or photon fields. By observing X-rays, we can study these most violent energy processes in the universe (Giacconi, 2002; Bambi and Santangelo, 2024). Observing these high-energy phenomena enables astronomers to investigate the physical conditions in these extreme environments-natural laboratories that cannot be replicated on Earth-in greater detail. At the same time, the strong penetrating power of X-rays allows them to pass through interstellar gas and dust clouds, revealing sometime hidden celestial objects, such as BHs and X-ray Binarys (XRBs). X-ray astronomy not only uncovers many hidden and extreme phenomena in the universe but also offers new perspectives and tools to enhance understanding of the universe's evolution. Typical X-ray astronomical sources include BHs, XRBs, Pulsars, Gamma-ray Bursts (GRBs), AGN, Supernova Remnants (SNRs), and high-temperature gas in galaxy clusters, among others. The detailed description of the scientific objectives will be provided in the next chapter.

X-ray astronomy, a significant and relatively young branch of astronomy, focuses on studying celestial X-ray radiation from the universe. It began with the unexpected discovery of the bright X-ray source Sco X-1, first reported by Giacconi et al. (1962); Bambi and Santangelo (2024). X-rays are high-energy electromagnetic photons, typically originating from NSs and Black Hole X-ray Binaries (BHXBs), AGN, galaxy clusters, and other extreme astrophysical environments characterized by high density, gravity, and magnetism.

The Earth's atmosphere selectively filters electromagnetic radiation across different wavelengths, with particular effectiveness in absorbing high-energy photons, including those in the ultraviolet (UV), X-ray, and gamma-ray bands. X-ray photons, which carry more energy than visible light photons, can ionize oxygen and nitrogen atoms in

the atmosphere, which acts as a barrier that prevents X-rays from reaching the ground. This process, known as photoelectric absorption, occurs when an X-ray photon is absorbed by an atom, resulting in the release of a free electron and the disappearance of the X-ray photon. For centuries, astronomers were restricted to the extremely limited range of visible wavelengths (about 380 to 750 nm) to which the human eye responds. The first detection of astronomical radio waves from the Milky Way was reported by Karl Jansky (1933) of Bell Telephone Laboratories. This has expanded astronomical observations to the range from 1 mm to several meters. Even in the early 20th century, significant advancements were made in optical and radio astronomy, yet the fundamental barrier of atmospheric absorption at other wavelengths remained. It was only when humans were able to launch astronomical instruments beyond Earth's atmosphere that a new era of full-spectrum observation in astronomy began, enabling us to observe the universe across the entire electromagnetic spectrum, from radio waves to gamma rays.

## 1.1 Method

This section describes the working principles of X-ray detectors, briefly overviews the relevant electromagnetic interactions, and highlights the two primary detection mechanisms: the photoelectric effect and Compton scattering. Additionally, it introduces detector types based on these mechanisms, such as proportional counters and SDDs. Finally, the section concludes with an overview of various optical systems employed in X-ray detection.

X-rays are electromagnetic radiation with extremely short wavelengths, typically ranging from $10^{-8}$ to $10^{-12}$ meters, corresponding to an energy range of 0.1 to 100 keV. Therefore, the energy of an X-ray photon is given by Equation 1.1, where $h$ denotes Planck's constant ($h \approx 6.626069 \times 10^{-34}\ Js$), $c_0$ is the speed of light ($c_0 \approx 2.99792 \times 10^5\ ms^{-1}$) and $\lambda_p$ is the wavelength of the radiation. The photon energy is inversely proportional to its wavelength $\lambda_p$ and is typically expressed in electron volts (eV).

$$E_p = \frac{hc_0}{\lambda_p} \tag{1.1}$$

Electromagnetic radiation is categorized by energy into radio waves, microwaves, Infrared (IR), visible light, Ultraviolet (UV) light, X-rays and gamma rays, as illustrated in Figure 1.1. Figure 1.1 shows the electromagnetic spectrum, with the top axis indicating the ranges of these categories.

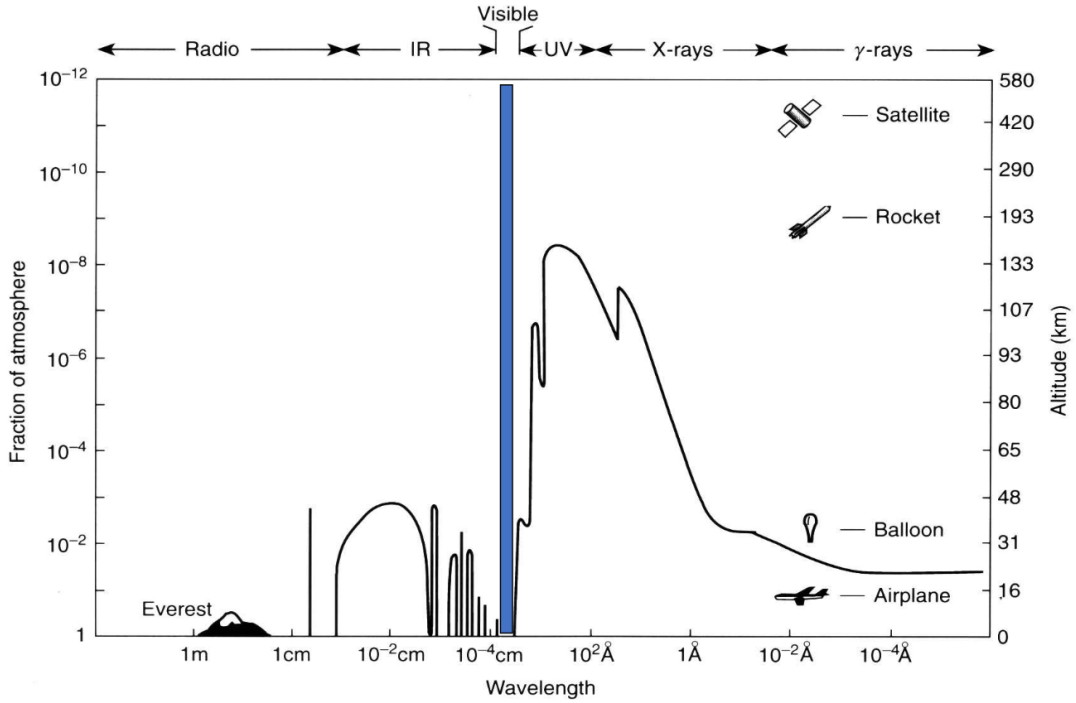


Figure 1.1: Attenuation of electromagnetic radiation in the atmosphere by Giacconi et al. (1968a) and Santangelo et al. (2023a). The bottom axis represents the electromagnetic wavelength in Angstroms (Å), where one Angstrom equals equal to $10^{-10}$ m. The left vertical axis denotes the fraction of the atmosphere at standard atmospheric pressure, while the right vertical axis corresponds to the respective altitude.

In X-ray astronomy, photons in the range of 0.1 to 10 keV are typically referred to as soft X-rays, while those in the range of 10 to 100 keV are known as hard X-rays. Soft X-rays are typically emitted by high-temperature gas with temperatures ranging from $10^7$ to $10^8$ K. The sources include the surfaces of NSs, the inner regions of Black Hole Accretion Discs (BHADs), and the accretion of compact stars (Longair, 2011). In contrast, Hard X-rays are often produced by non-thermal processes, such as inverse Compton scattering, bremsstrahlung and synchrotron radiation. Inverse Compton scattering occurs when relativistic electrons scatter low-energy photons, transferring energy to the photons. In this process, the photons gain energy while the electrons lose energy. This is termed the 'inverse' process because the energy flow (from electrons to photons) is opposite to that in the standard Compton effect (Jones, 1968).

### 1.1.1 Electromagnetic Interactions of High-Energy Photons

The three primary processes through which high-energy photons interact with atoms, nuclei, and electrons are photoelectric absorption, Compton scattering and electron positron pair production. These processes play a crucial role in detecting high-energy

particles and photons.

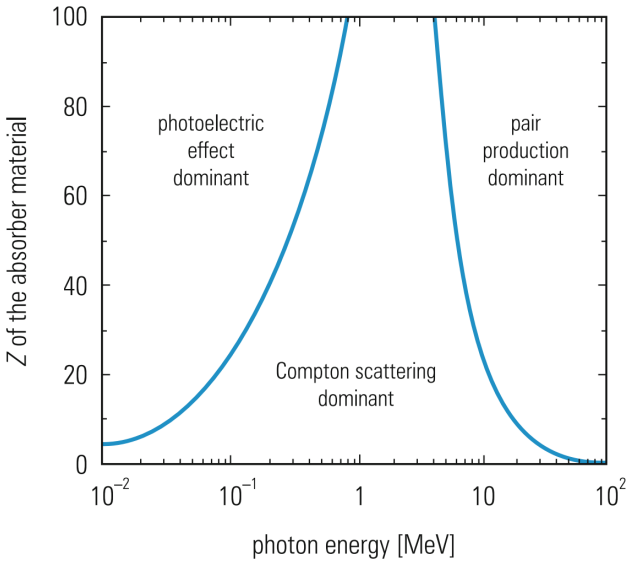


Figure 1.2: The chart illustrates the dominant photon-matter interaction mechanisms across different energy ranges. The horizontal axis represents the photon energy in megaelectronvolts (MeV), while the vertical axis shows the atomic number Z of the absorber material, which corresponds to the number of protons in the nucleus of the substance. (Source: Grupen (2020))

As illustrated in Figure 1.2, photoelectric absorption is typically observed in the spectra of most X-ray sources with energies below approximately 1 keV. Compton scattering, on the other hand, dominates in various astrophysical environments, ranging from stellar interiors to the spectra of binary X-ray sources. When the energy of the detected exceeds 1.022 MeV, it can interact with the electric field of the nucleus, resulting in the production of a positron and an electron pair. This process is known as pair production.

### Photoelectric Absorption

The photoelectric absorption process generally occurs in the low-energy range (0.01 to 0.1 MeV). The main principle of the photoelectric effect is that at low energies, X-ray photons interact with atoms in a material, transferring nearly all of their energy to the ejected atomic electrons. It primarily occurs in elements with higher atomic numbers, and as the atomic number (Z) increases, the significance of the photoelectric effect becomes more pronounced. In astronomy, low-energy X-rays are typically detected through focal plane imaging using detectors based on the photoelectric effect. The detectors used for X-ray focal detection include multi-wire proportional chambers filled with inert gases (such as krypton or xenon), single-channel electron multipliers (channel multipliers), and devices such as semiconductor counters or X-ray Charge-Coupled Devices (CCDs).

### Compton scattering

Compton scattering generally occurs in the medium energy range (0.1 to 10 MeV) when X-ray or gamma-ray photons interact with matter. During this process, the photons lose energy and their wavelength increases. The change in wavelength can be calculated using the Compton formula:

$$\Delta\lambda = \frac{h}{m_e c_0}(1 - \cos\theta) \tag{1.2}$$

where:
- $\Delta\lambda$ is the change in wavelength
- $h$ is Planck's constant
- $m_e$ is the electron rest mass
- $c_0$ is the speed of light
- $\theta$ is the scattering angle of the photon.

According to the relationship between energy and wavelength given in Equation 1.1, the change in photon energy after scattering $E'$ can be determined from the change in wavelength during scattering (Blumenthal and Gould, 1970).

$$E' = \frac{hc_0}{\lambda + \frac{h}{m_e c_0}(1 - \cos\theta)} \tag{1.3}$$

The formula can be further simplified to yield a more explicit expression for the energy lost by the photon during the scattering interaction.

$$E' = \frac{E}{1 + \frac{E}{m_e c^2}(1 - \cos\theta)} \tag{1.4}$$

where $E$ is the energy of the initial photon.

In high-energy astrophysics, inverse Compton scattering is a process opposite to the previously described Compton scattering. In inverse Compton scattering, photons gain energy from high-energy electrons. This phenomenon is typically described as the interaction between a non-relativistic thermal electron gas, with temperature $T_e$, and incident photons. The average energy transfer $\langle\Delta E\rangle$ per scattering event can be approximately described by the following formula (Titarchuk, 1994):

$$\langle\Delta E\rangle \approx \frac{4k_B T_e}{m_e c^2} E_{\text{photon}} \tag{1.5}$$

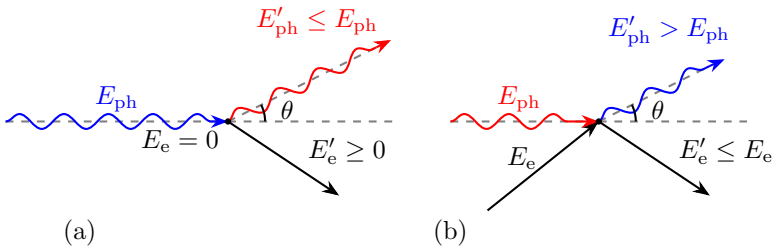


Figure 1.3: Compton and Inverse Compton Scattering. (a) Scattering in the rest frame of the electron before the interaction: the photon loses energy, and the electron gains energy. (b) Scattering in the laboratory frame: the photon gains energy due to the motion of the high-energy electron.

where:

- $\langle \Delta E \rangle$ represents the average energy gained by a photon per inverse Compton scattering event
- $k_B$ is the Boltzmann constant
- $T_e$ is the temperature of the electron gas
- $m_e$ is the rest mass of the electron
- $c$ is the speed of light
- $E_{\rm photon}$ is the energy of the incident photon.

Comptonization refers to the repeated Compton scattering of photons by high-temperature electrons, where the spectrum of an X-ray source is significantly altered due to repeated inverse Compton scattering. This process results in the modification, or "Comptonization" of the original photon spectrum. Comptonization is particularly important in high-temperature plasmas and high-energy radiation environments, such as in X-ray binary systems and AGN (Illarionov and Siuniaev, 1975; Sunyaev and Titarchuk, 1980).

### 1.1.2 X-ray Detectors

The operation principles of most X-ray detectors are based on the fundamental physical interactions described in the previous section. A typical X-ray astronomy experiment is equipped with a detector that converts incident X-rays into measurable electrical signals for subsequent analysis. These electrical signals typically encode information about the astronomical source, including the energy and arrival time of individual photons, their flux, interaction position within the detector, and polarization state.

The design of astronomical detectors involves carefully balancing performance parame-

ters such as energy resolution, spatial resolution, temporal resolution, and sensitivity to meet specific scientific requirements. For example, for spectral analysis, energy resolution is a key factor that determines the detector's ability to distinguish X-ray photons of different energies, thus affecting the accuracy of the spectrum and the level of detail of the detection results. To discern the detailed structures of celestial bodies, spatial resolution will be optimized to achieve varying levels of imaging clarity, tailored to specific observational requirements. Temporal resolution is critical for research to study time-variable phenomena (e.g., pulsars, X-ray bursts), and is often required at the microsecond level.

### Proportional Counters

The proportional counter, developed in the 1940s, is one type of detector that later became widely used in the early stages of X-ray astronomy. Proportional counters served as the workhorse for X-ray detection for nearly four decades. As technology developed, there was a continuous performance enhancement in them. In the 1960s, it became possible to introduce an Imaging Proportional Counter (IPC) which would record the position of each incident X-ray photon and would build up two-dimensional images. The IPC achieved a linear resolution of $200 - 500$ $\mu$m within the energy range of $0.2 - 5$ keV. Devices of this kind have flown on several X-ray astronomy satellites, including the Einstein Observatory, EXOSAT, and ROSAT. With the advancement of science and technology, solid-state detectors have emerged, such as X-ray CCDs, SDDs, and microcalorimeters. These detectors have played an important role in missions such as the Chandra X-ray Observatory and XMM-Newton.

### Gaseous Ionization Detectors

The gas ionization detectors commonly used in astronomical detection include mainly Geiger counters and proportional counters. These detectors apply the principle behind their construction when using the photoelectric effect of the radiation on gas to detect X-rays or other types of radiation. The gas used is typically a combination of an inert gas, such as Argon (Ar) or Helium (He), and a quenching gas, such as Ethanol ($C_2H_5OH$) or Isobutane ($C_4H_{10}$), or sometimes with a mixture of these gases. The specific mixing ratio is related to the application scenario and requirements of detection, achieved by best performance, stability, and sensitivity of the detector.

In early X-ray astronomy experiments, Geiger counters were used as detectors. Its working principle is based on gas ionization. Under the influence of high voltage, the primary ionized electrons initiate avalanche ionization, resulting in the formation of a strong pulse signal. Almost every event will trigger an avalanche effect, causing the gas molecules in the tube to be completely ionized. The anode voltage is high

enough that the avalanche effect reaches saturation. However, Geiger counters cannot distinguish the energy of radiation particles and only record the number of events. Therefore, they were soon replaced by proportional counters.

In a proportional counter, when a high-energy photon enters the inert gas, it first liberates a photoelectron via the photoelectric effect. This free electron moves towards the anode under the applied electric field. As it moves, it accelerates and gains energy. At the time of approaching the anode, the electron causes further ionization in the gas molecules, thereby producing secondary ion pairs. This process is known as the avalanche amplification effect. Since the electron multiplication is proportional to the number of electrons generated through main ionization after being amplified by the avalanche process, it forms the basis for the name given to this type of detector—the "proportional counter."

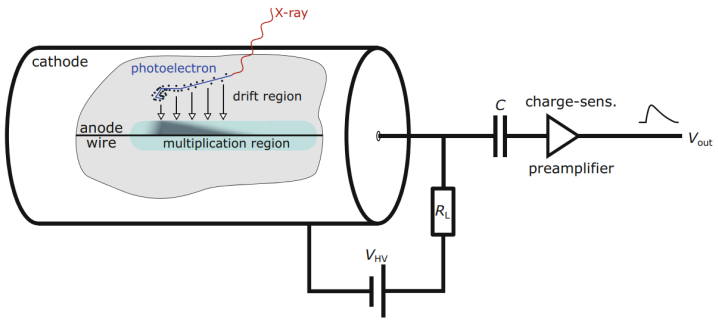


Figure 1.4: The working principle of a proportional counter for the measurement of X rays. (Source: Santangelo et al. (2023b))

Another technical development is the Gas Scintillation Proportional Counter (GSPC), a variant of the proportional counter. The GSPC operates similarly to a proportional counter, but instead of electron avalanche and charge collection, it utilizes a scintillation region and Photomultiplier Tubes (PMTs). Its energy resolution is approximately twice that of a conventional proportional counter, achieving a minimum resolution of around 7% at 6 keV. In the GSPC, incident X-rays ionize atoms in the detector' s gas volume, producing a primary photoelectron. This photoelectron collides with other atoms, creating a cloud of secondary electrons that migrate toward the bottom of the detector under the influence of an electric field in the drift region. When these secondary electrons enter the high electric field of the scintillation region, they gain sufficient energy to excite gas atoms, typically xenon, which subsequently collide to form diatomic molecules. As these molecules return to their ground state, they emit ultraviolet photons, which pass through an exit window and are detected by the PMTs. The light detected by each PMT can then be used to estimate the position of the incident X-ray, providing both spatial and energy information. This technology

has also been successfully flown on satellites like Tenma (Makino and Team, 1987), EXOSAT (White and Peacock, 1988), ASCA (Ohashi et al., 1996) and the BeppoSAX HPGSPC (Manzo et al., 1997).

**Scintillator Detectors**

As the energy of X-rays increases, gas detectors gradually become impractical. At X-ray energies above 50 keV, the penetrating power of photons increases significantly. The density and thickness of the gas cannot effectively block these high-energy photons. To detect such high-energy photons, one would need deeper gas detectors or higher gas pressures to increase the gas column density and thereby enhance the probability of photon – gas interactions. However, a more practical and efficient alternative is the use of scintillation detectors.

Scintillation detectors work by utilizing scintillators (e.g., NaI and CsI), which emit visible light after absorbing X-rays, and then convert the visible light into an electrical signal via a PMT or photodiode, which collects and amplifies the signal to detect the radiation event. In practice, NaI and CsI are often combined to make phosphor stack detectors. Due to the different scintillation times of these two crystals, it is possible to distinguish in which crystal the interaction has occurred, thus effectively distinguishing between the effective signal and the background noise. For example, a phosphor composed of NaI(Tl) layered over CsI(Na) was utilized in the HEXTE instrument on RXTE (Rothschild et al., 1998) and in the PDS instrument on BeppoSAX (Frontera et al., 1997).

**Microchannel Plates**

The Microchannel Plate (MCP) detector is a very sensitive electron-multiplying detector basically applied for the low-energy photon detection, especially in the field of ultraviolet rays, soft X-rays, and particle flows of electrons and ions. It consists of a plate composed of many small holes or tubes, arranged next to each other, usually these small holes are inclined to the normal direction of the plate, so that the incident X-rays or ultraviolet radiation enter from one side of the hole.

Its operating principle relies on the interaction of high-energy particles (or photons) with the microchannel walls, which releases secondary electrons. These secondary electrons are continuously multiplied in a cascade process within the microchannel to obtain an amplified signal, as schematically indicated in the right-hand part of Figure 1.5. This in turn produces a current or voltage signal measurable at the anode. The signal is collected by the anode wire, and its incident position can be determined very accurately, thus forming an imaging detector with high spatial resolution.

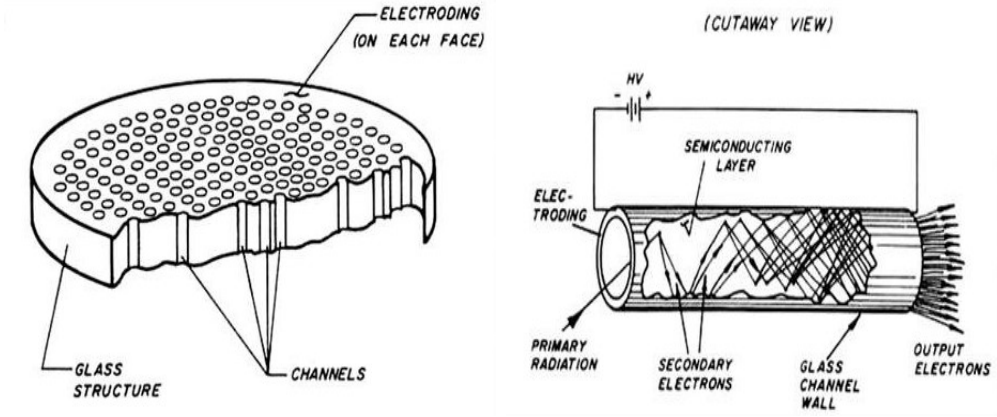


Figure 1.5: Schematic of a microchannel plate detector (Left) and the generation of an electron avalanche with a single incident electron (Right). (Source: Wiza et al. (1979))

However, this type of detector has several limitations. First, since the X-rays cause an electron avalanche in the glass walls of the tubes, almost all the spectral information is lost. Another point is due to the space charge effect in the hole wall glass. When too much charge is extracted, the remaining positive space charge will make it difficult for the electrons to be released (Edgar, 2011).

**Microcalorimeters**

In the 1990s, NASA proposed microcalorimeters to address the limitations of traditional X-ray gratings when observing fainter and extended sources. The working principle is to obtain information by measuring the temperature change after a small piece of material absorbs X-rays. When an X-ray photon hits the absorber, it will knock out electrons in the absorbing material, which move inside the absorber and eventually raise the temperature of the absorber by a few millikelvin. The temperature change is measured by a thermistor, and the measured temperature increase is approximately proportional to the energy of the X-ray photon, thus achieving energy measurement. However, the X-rays from celestial bodies are very weak, resulting in a very small temperature rise in the instrument, so the instrument needs to be cooled to near absolute zero. This requires a complex cryogenic system and extremely sensitive thermometers to accurately detect tiny temperature changes. For example, the microcalorimeter on Suzaku XRS (Kelley et al., 2007) has a very complex cooling system to achieve low temperature control.

### Silicon Drift Detector

SDDs are a type of silicon-based semiconductor detector first proposed by Gatti and Rehak (1984). While the detectors were initially fabricated for position measurement of particles, but Rehak et al. (1985) soon realized that the low noise and high charge collection efficiency obtained in SDDs made them exceptionally well-suited for spectroscopy measurements requiring very high energy resolution. For conventional semiconductor detectors, normally high capacitance leads to high electronic noise, which in turn results in poor energy resolution. On the other hand, SDDs use innovative design features to actually cut down the capacitance of the detector, noise levels, and hence secondarily increase the accuracy and quality during the process of detection. In the 1990s, with advancements in manufacturing processes and electronic integration technologies, SDDs became increasingly practical and saw widespread adoption.

The operating principle of the SDD relies on the use of drift fields to guide charge carriers toward the collector, allowing for the anode to have an arbitrary shape. This design enables a small-capacitance anode to read out the charge generated by an incident photon over a large active area. The two opposing p+ contacts (see Figure 1.6) are maintained at the same voltage, while the voltage applied to the adjacent p+ contacts gradually decreases from one contact to the next in the direction of the anode. This design creates a potential gradient within the detector, with the lowest potential at the anode (from the perspective of electrons). This gradually decreasing voltage gradient directs the electrons to drift along a predetermined path towards the anode, thus enabling efficient charge collection. When a X-ray photon strikes the detector, a cloud of electron-hole pairs are generated in proportion to the energy of the photon. The holes are quickly collected by the nearby p+ contact, while the electrons drift gradually along a predetermined path to the anode, driven by the drift electric field within the detector. Due to the extremely small capacitance of the anode, the accumulated electrons are efficiently collected and processed by a preamplifier, resulting in an electrical signal that is proportional to the energy of the incident photon.

With the development of a large-area SDD for the ALICE Experiment Internal Tracking System (ITS) of the Large Hadron Collider (LHC) by Zampa et al. (2009), SDD have taken an important step towards larger area applications. These detectors optimized for position sensing have a large effective area of 52 $cm^2$, significantly improving position resolution and detection efficiency, making them more practical and capable of detection in large-scale experiments. The SDDs used in the eXTP LAD were originally designed for the ALICE Inner Tracking System at CERN's Large Hadron Collider (Rashevsky et al., 2001, 2002), and optimized for the eXTP. These optimized

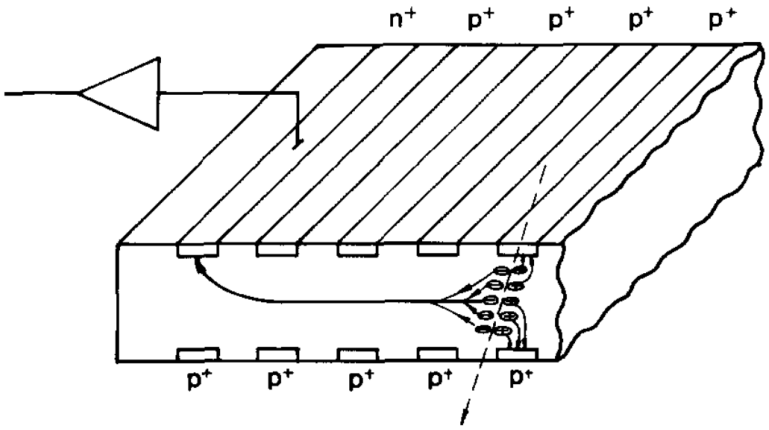


Figure 1.6: The Working principle of SDD. (Source: Rehak et al. (1985))

SDDs have sensitive area dimensions of 10.86 × 7.00 $cm^2$ with a thickness of 450 $\mu$m (Rachevski et al., 2014). The SDD used for eXTP is described in Section 3.2.1.

### 1.1.3 X-ray Optics

As previously noted, the short wavelength and high energy of X-rays give them strong penetrating power. This renders traditional refractive lenses ineffective for focusing. For most materials, the refractive index for X-rays is almost equal to 1, meaning that conventional refraction cannot focus X-rays effectively. Furthermore, their high energy causes most X-rays to either penetrate through or be absorbed by materials, making traditional reflection-based focusing impractical.

Therefore, X-ray optics is developed for focusing the X-rays onto detectors with the aim of improving the sensitivity of detectors and spatial resolution. Using specially designed mirror systems or other optical elements, such as capillary optics, Wolter optics, and coded masks, high-energy rays like X-rays can be effectively imaged and detected.

#### Capillary Optics

X-ray capillary optics operate on the principle of total external reflection. They use hollow glass capillaries as waveguides to channel X-rays via multiple reflections. This concept was first established in the late 1920s (Hoffman et al., 1994). X-ray capillaries are often used in conjunction with collimators to reduce the Field of View (FoV), helping to avoid source confusion and minimize background noise.

X-ray capillary optics are primarily categorized into two types: aggregate X-ray capillary optics and single X-ray capillary optics. The former, also known as the

Kumakhov lens (see Figure. 1.7 ) or X-ray lens (Kumakhov and Komarov, 1990), can focus a larger X-ray beam over a relatively shorter distance.

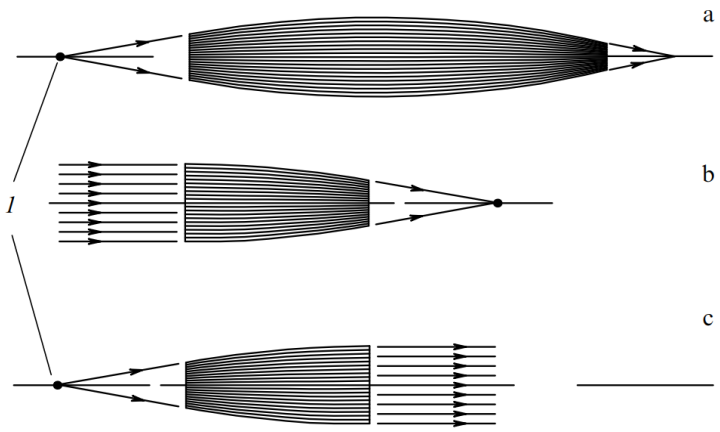


Figure 1.7: The Three types of Kumakhov X-Ray optics. (Source: Lider (2018))

Capillary optics has evolved from a single capillary to a multi-capillary array, which is called a capillary plate. The diameter of each capillary hole can range from a few microns to hundreds of microns, and multiple capillary channels work in parallel, significantly improving photon flux and focusing efficiency. Capillary plates can effectively collect and focus more X-ray photons than a single capillary tube.

### Coded Mask

The coded aperture technique, also known as spatial aperture modulation, enables imaging of high-energy radiation such as X-rays and gamma rays. It was independently proposed by Ables (1968) and Dicke (1968). Coded aperture modulates the incident radiation by placing a mask with a specific pattern in front of the detector. The mask is made of X-ray absorbing material and contains transparent and opaque areas to form a specific coded pattern. When radiation passes through the mask, a projected pattern ('image') is generated on the position-sensitive detector. This enables simultaneous measurement of the flux and position of multiple sources in the field of view. By mathematically decoding the image, the original image of the radiation source can be reconstructed.

### Wolter Optics

The Wolter optical system is an optical system used to focus X-rays and high-energy radiation. It mainly achieves focusing and imaging by combining specific curved mirrors (usually parabolic mirrors and hyperbolic mirrors) to achieve grazing incidence ($<1°$) reflection. As the energy of the incident photon increases, the required grazing incidence angle decreases to ensure the reflection effect. The X-ray focusing optical design originally proposed by Wolter (1952) was used for X-ray microscopy, while Giacconi

and Rossi (1960) first explored the application of these geometries in X-ray astronomy, and later they were widely used in high-energy astronomical imaging observations. In the Wolter-I optical system, the X-rays are first reflected on the parabolic mirror, followed by a second reflection on the hyperbolic mirror, and finally imaged at the focal plane, as shown in Figure 1.8. In order to increase the effective aperture, a nested structure of mirrors of different sizes is usually used.

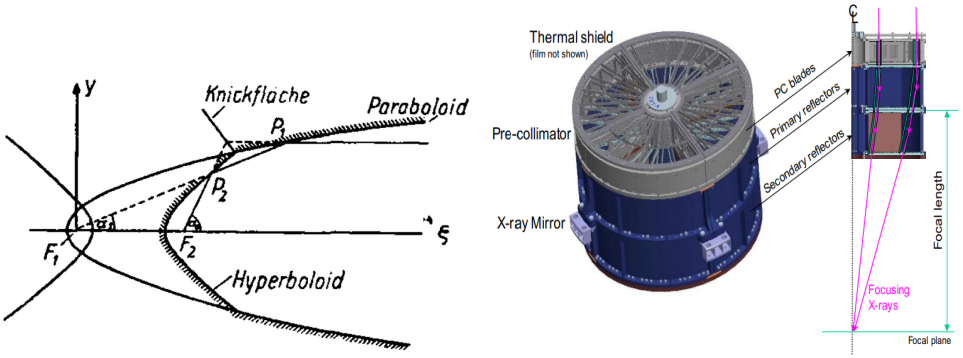


Figure 1.8: X-ray optics of Wolter's type I by Wolter (1952)(Left). Flight Models of the X-ray Mirror Assembly (XMA) for the X-ray Imaging and Spectroscopy Mission (XRISM). (Right). (Mori et al., 2022)

This configuration has been successfully applied in many X-ray missions, such as Chandra (Weisskopf et al., 2002), NuSTAR (Harrison et al., 2010), XRISM (Mori et al., 2022), and other observatories.

## 1.2 History and Status of X-ray Instruments and Missions

This section introduces the development of X-ray astronomical observations, a field whose progress is closely tied to the advancement of human space technology. This section outlines the role and development of key X-ray observatory satellites across different historical stages, including an overview of the past, present, and future prospects. As mentioned earlier, the Earth's atmosphere is opaque to X-ray radiation, making X-ray observations dependent on the advancement of space technology to enable stable and continuous observations. After World War II, rockets captured from Germany were initially used to send X-ray detection instruments outside the atmosphere for short-term, limited observations. As technology advanced, satellites gradually became the ideal observation platforms and were widely adopted. This shift made long-term, stable X-ray observations the norm and led to an explosive growth in the number of detected X-ray sources.

Nowadays, satellite platforms are widely recognized as the primary means of X-ray observation worldwide. Balloons and rockets are now primarily used as technology verification platforms and are seldom employed to send detection instruments into space. As of the writing of this thesis, numerous iconic high-energy physics detection instruments are operating in space, and several flagship international cooperation projects are under development. The eXTP project discussed in this thesis is one such project. New space-based observatories and more advanced detection instruments are indispensable and powerful tools for humanity's exploration of the universe.

This section provides a concise overview of the history of scientific observations in X-ray spectroscopy, followed by an introduction to the current status of in-orbit X-ray observation instruments. The concluding part offers a perspective on potential future missions for X-ray timing observatories.

### Sounding Rockets

After World War II, the U.S. military provided scientific institutions with the opportunity to launch scientific instruments using V-2 rockets. On September 29, 1949, a V-2 rocket launched from White Sands carried a set of photon counter tubes, which were sensitive to very narrow frequency ranges. The experiment, conducted by Friedman et al. (1951), confirmed that the ionization of the atmosphere above 87 kilometers was caused by solar X-rays emitted by the Sun's corona, the hot outer layer of the Sun's atmosphere. This marked the first time X-ray instruments were ever launched beyond the Earth's atmosphere.

In June 1962, a group led by Riccardo Giacconi at American Science & Engineering (AS&E) successfully launched an astronomical instrument for X-ray observations. Its primary goal was to detect X-rays from the Moon using an Aerobee rocket that operated for more than five minutes. The onboard large-area Geiger counter instead detected a strong X-ray source from the constellation Scorpius (Giacconi et al., 1962), along with a smooth background glow(see Figure 1.9). This event marked the birth of a new field of astronomy. However, no X-ray radiation was detected from the Moon[1].

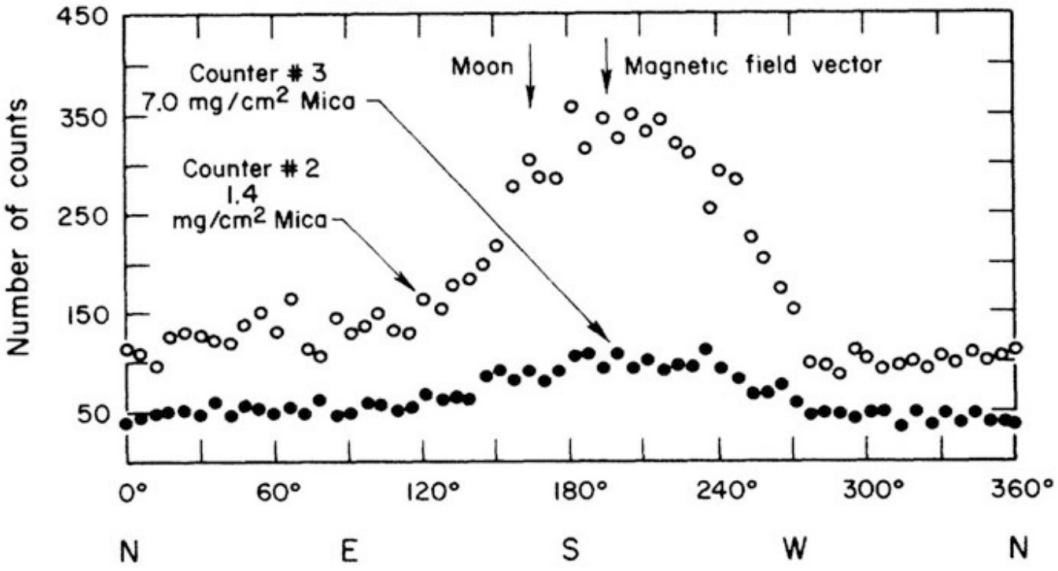


Figure 1.9: The azimuthal distribution of the count rates from Geiger counters #2 and #3 of the 1962 mission shows a peak at 195°, and the count never reaches zero, indicating the presence of a diffuse X-ray background. (Source: Giacconi et al. (1962))

Rocket-assisted X-ray astronomy activities developed rapidly after the successful detection of an X-ray source in 1962. The United Kingdom also joined the early race in X-ray astronomy, notably through the Skylark project, which conducted the first survey of the southern hemisphere. For a list of comprehensive X-ray rocket exploration activities, see Santangelo et al. (2023c)。

### Balloons

As early as the period around World War I, scientists realized that balloons could be used to send observational instruments above the atmosphere. The use of balloons for scientific research can be traced back to 1912, when Austrian scientist Victor Hess carried an electroscope on a balloon to an altitude of 5 kilometers and confirmed the existence of rays emitted from space to Earth that could cause gas ionization (Hess,

[1]X-ray emission from the Moon was not detected until 1990, when it was observed by the Roentgen Satellite X-ray Observatory (ROSAT).

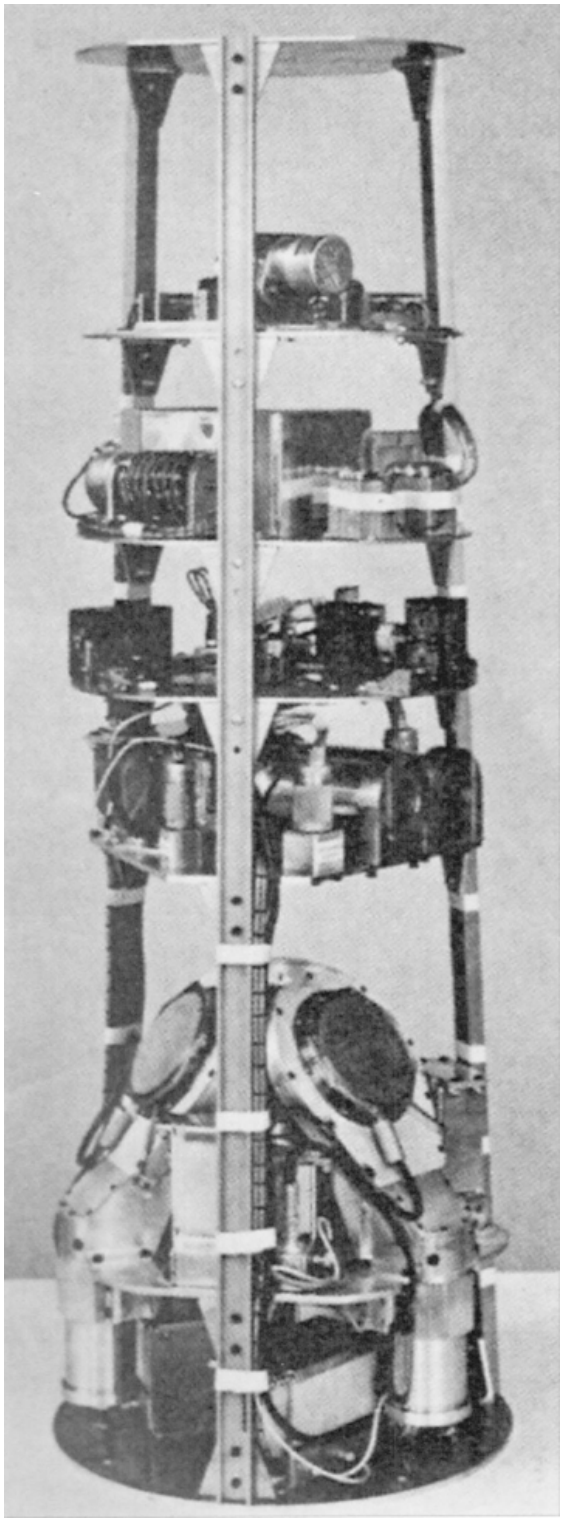

Figure 1.10: The payload of the June 12, 1962 AS&E mission, launched by an Aerobee 150 rocket capable of reaching an altitude of 200 km, contained three Geiger counters, each with an active area of approximately 10 cm $^2$. The counters were equipped with Mica windows of two different thicknesses, 1.4 and 7 mg cm$^{-2}$, resulting in peak efficiencies of 10% and 20%, respectively, in the wavelength range of 2 to 8 Å. (Source: Giacconi et al. (1974))

1912). In 1965, the first balloon observation of a cosmic X-ray source, the Crab Nebula, was made by Clark (1965). The detector carried by the balloon typically consisted of a large-area NaI or CsI scintillation counter, equipped with an anti-coincidence collimator to eliminate interference from charged particles and scattered X-rays.

Of particular note are the successful balloon campaigns carried out between 1973 and 1980 by the Institute of Astronomy and Astrophysics (AIT) at the University of Tübingen, in close cooperation with the Max Planck Institute for Extraterrestrial Physics (MPE) in Garching. These campaigns primarily observed X-rays in the high-energy range (20-200 keV) using scintillation counters with NaI(Tl) crystals, as reported by Arnold et al. (1974); Staubert et al. (1981).

**The First X-ray Satellite**

Although the above two methods could lift the detector outside the atmosphere, the observation sensitivity remained very poor (Morrison, 1967; Giacconi et al., 1968b) due to the short duration of exposure in rocket-based experiments and the residual Earth's atmosphere, which limited the energy range of observations in balloon-borne experiments. The true maturation of X-ray astronomy was not realized until the launch of the UHURU satellite.

UHURU (freedom or independence in Swahili) was launched in 1970 and was originally named the Small Astronomical Satellite 1 (SAS-1). It was a small astronomical satellite developed by NASA, dedicated to observing cosmic X-ray sources. This is the AS&E group's follow-up project after its rocket project. Uhuru was launched into a nearly equatorial circular orbit with an apogee of about 560 km and a perigee of 520 km, with an inclination of 3°. The instrument onboard UHURU consisted of two sets of argon-filled proportional counters, sensitive to X-ray photons in the range of 2-20 keV. These instruments used collimators to limit the field of view to 5×5 degrees and 5×0.5 degrees, respectively, in order to improve angular resolution.

UHURU operated in scanning mode and conducted the first complete all-sky X-ray survey, detecting a total of 339 X-ray sources of various types, including X-ray pulsars, X-ray binaries, the black hole X-ray binary Cyg X-1, supernova remnants, and massive extragalactic objects, as shown in the Figure 1.11.

**Einstein Observatory**

The Einstein Observatory, launched in 1978, was the first imaging X-ray observatory. Since X-rays cannot be focused directly like normal optics, it used a Wolter type-I grazing-incidence X-ray focusing optics system (Wolter, 1952) for imaging and was launched into an orbit of 465-476 km with an inclination of 23.5°. Its scientific

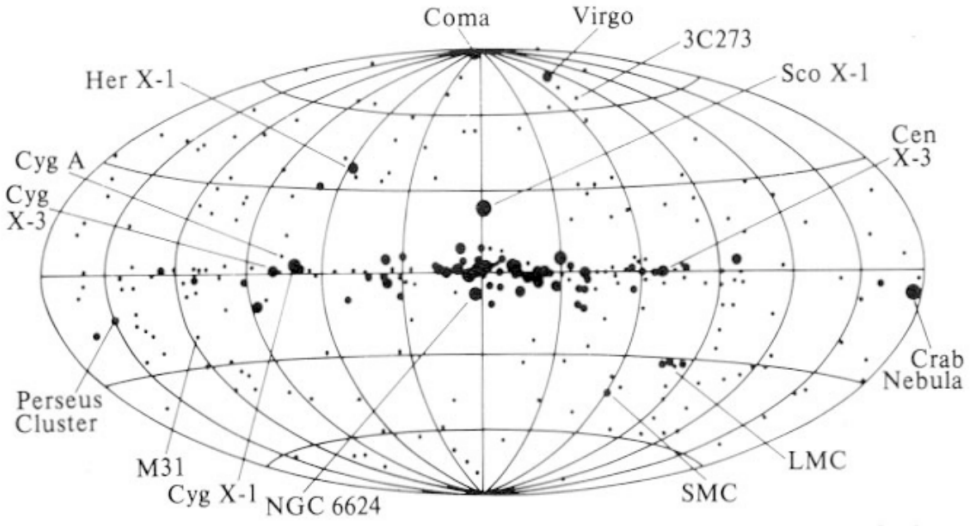


Figure 1.11: The X-ray sources detected after UHURU, according to the fourth UHURU catalog. (Source: Forman et al. (1978))

payload consists of four instruments that can be rotated sequentially into the focal plane, covering the energy range of 0.2-20 keV: a High Resolution Imager (HRI) (Grindlay et al., 1980), an IPC (Gorenstein et al., 1981; Giacconi et al., 1979), and two spectrometers (Holt, 1975; Lum et al., 1992).

The Einstein Observatory made numerous groundbreaking discoveries in X-ray astronomy. It was the first X-ray observatory capable of resolving detailed images of observed sources and the first to conduct high-resolution studies of supernova remnants, revealing that the coronal radiation of normal stars is stronger than previously expected. During its operation, the Einstein Observatory identified approximately five thousand X-ray emission sources (Schlegel, 2002).

**EXOSAT**

The European X-Ray Observatory Satellite (EXOSAT) was the European Space Agency's first X-ray observatory, operational from May 1983 to April 1986. It was launched into a highly eccentric Earth orbit, with an apogee of 191,000 km, a perigee of 350 km, and an equatorial inclination of 72.5°. The payload of the mission consisted of two low-energy (LE) telescopes and one medium-energy (ME) telescope, which produced spectra, images, and light curves across different EUV and X-ray energy bands (Taylor et al., 1981).

One of the most significant discoveries made by EXOSAT was the detection of Quasi-Periodic Oscillation (QPO) in the X-ray intensity of several low-mass X-ray binaries (LMXRB) (White and Peacock, 1988). ME also provides a rich survey of large areas

of the X-ray sky called the Medium Energy Slew Survey.

### ROSAT

The Roentgen Satellite (ROSAT) is a collaborative project between Germany, the United Kingdom, and the United States, launched into orbit in 1990. It was launched into a nearly circular orbit with a perigee of 539 km, an apogee of 554 km, and an inclination of 53°. The satellite carries two imaging telescopes, operating in the soft X-ray (0.1-2.4 keV) and EUV (0.06-0.2 keV) bands, which are equipped with four nested Wolter type-I mirrors. To construct the X-ray telescope's mirror, which was the largest and most precise of its kind at the time, engineers used Zerodur, a material characterized by zero thermal expansion and extremely low surface roughness. The telescope features a rotating disk at the focal plane with three installed imaging X-ray detectors, position sensitive proportional counters (PSPC) with a spatial resolution of 20 arcseconds, and one high resolution imager (HRI) with a spatial resolution of 5 arcseconds. The primary components of the imaging X-ray telescope (XRT) were manufactured by Germany, while the United Kingdom built and operated the EUV telescope, and the United States provided the launch and the High Resolution Imager (HRI).

ROSAT conducted the first all-sky survey using XRT and EUV imaging telescopes, leading to the discovery of 150,000 X-ray objects and 479 EUV objects (Trümper, 1984). Additionally, ROSAT provided detailed morphological data on supernova remnants and galaxy clusters. It also detected the shadowing effect of molecular clouds on diffuse X-ray emission.

### Chandra X-ray Observatory

The Chandra X-ray Observatory (Weisskopf et al., 2002) is one of the most important X-ray observatories still in operation this century. Initially named the Advanced X-ray Astrophysics Facility (AXAF), it later renamed in honor of Indian-American scientist Subrahmanyan Chandrasekhar, who won the Nobel Prize in Physics in 1983 for his work on stellar evolution and black hole theory. The unique feature of the Chandra Observatory is its high-resolution mirror assembly, a Wolter type I X-ray telescope consisting of four pairs of high-precision parabolic and hyperbolic mirrors. X-rays need to "graze" the mirrors at a very shallow angles to be properly focused onto the scientific instruments. The satellite was launched by the United States in July 1999, and as of the writing of this thesis, the observatory remains operational in orbit. The Chandra Space Telescope is equipped with instruments that cover an X-ray energy range from 0.1 keV to 10 keV, enabling it to detect both low- and high-energy X-ray sources. It carries four scientific instruments, including the High-Resolution Camera (HRC), which

uses two sets of MCP detectors to capture X-rays and produce ultra-high-resolution images (with a full width at half maximum, FWHM, of less than 0.5 arcseconds). The Advanced CCDs Imaging Spectrometer (ACIS) consists of 10 X-ray CCDs arranged in two arrays: one for imaging and the other for spectroscopy. This configuration allows it to simultaneously produce X-ray images and collect spectral data. It is also equipped with the High Energy Transmission Grating Spectrometer (HETG) and the Low Energy Transmission Grating Spectrometer (LETG), which are used to measure the spectral data of X-rays (Weisskopf et al., 2000a). See Figure 1.12 for detailed instrument configuration.

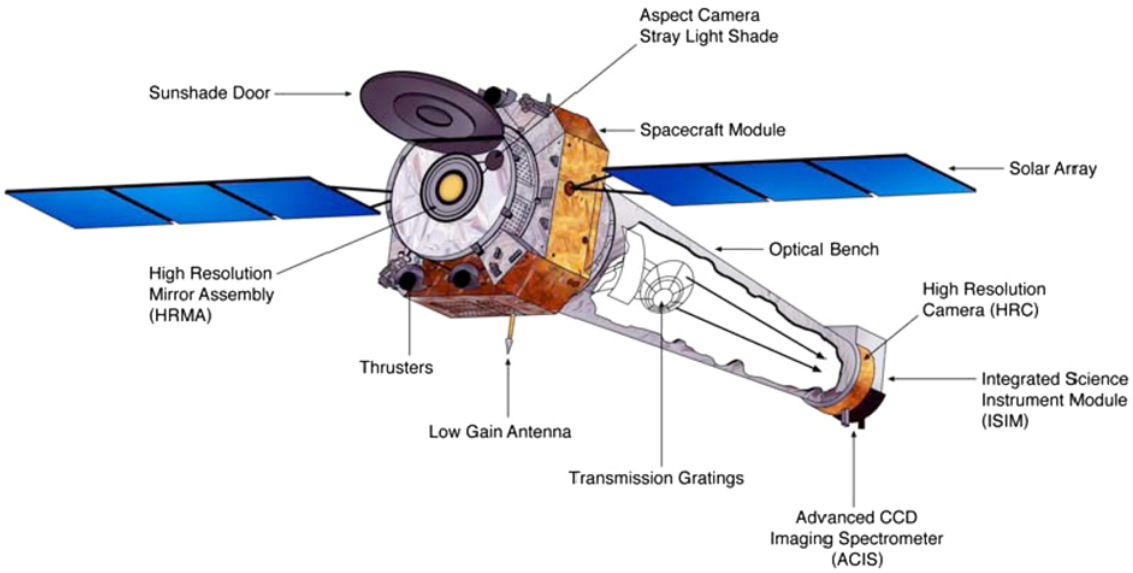


Figure 1.12: Schematic representation of the Chandra X-ray Observatory (Source: (Weisskopf, 2012; Schwartz, 2004)).

More importantly, the data from Chandra greatly enriched the developing field of X-ray astronomy. This telescope discovered a new ring around the central pulsar and its jets, partly visible by other telescopes, within Supernova Remnant Crab Nebula (Weisskopf et al., 2000b). Chandra has proved to show exceptional capabilities in the study of black holes. It detected the first X-ray emission from the super-massive black hole, Sagittarius A*, at the center of the Milky Way (Baganoff et al., 2001), and discovered a new kind of black hole in the galaxy M82 (Griffiths et al., 2000).

**XMM-Newton**

Around the same time as Chandra, the European Space Agency (ESA) launched one of its most successful telescopes, XMM-Newton, also known as the High Throughput X-ray Spectroscopy Mission and the X-ray Multi-Mirror Mission. This X-ray space observatory, launched in December 1999 and named after the physicist and astronomer Sir Isaac Newton, remains operational. Its primary mission is to study interstellar

X-ray sources, conduct both narrow-band and broadband spectroscopy, and, for the first time, simultaneously image objects in X-ray, optical (visible), and ultraviolet wavelengths (Pierre et al., 2016).

XMM-Newton carries three instruments, namely European Photon Imaging Camera (EPIC), Reflection Grating Spectrometer (RGS), and Optical Monitor (OM), whose detailed descriptions are shown in Figure 1.13.

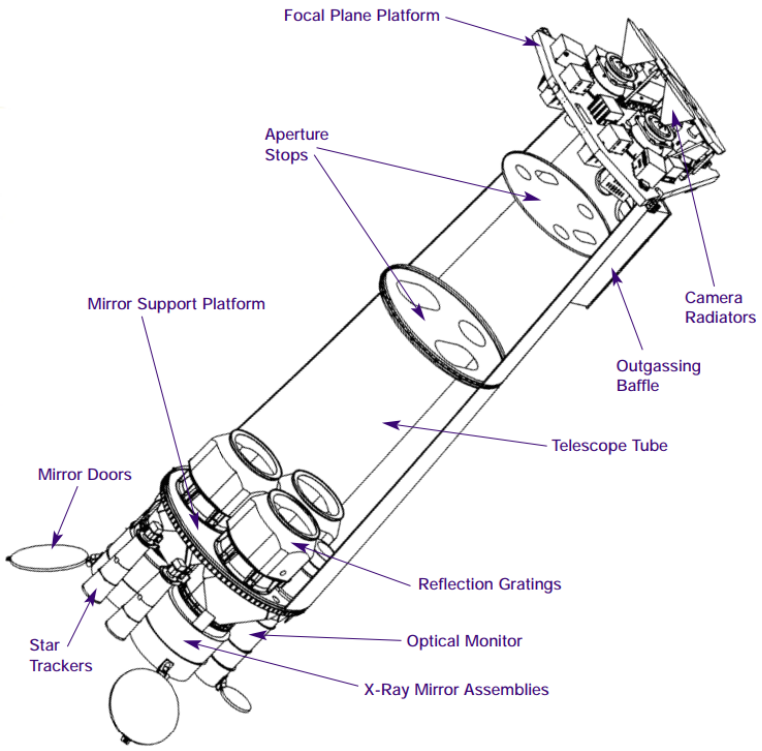


Figure 1.13: The physical design of the XMM telescopes illustrates the X-ray mirror assemblies and the focal-plane cameras positioned at opposite ends of the telescope tube. The main components include three Wolter I-type grazing incidence telescopes, two of which are equipped with Reflection Grating Spectrometer (RGS) assemblies for spectroscopy. These three telescopes operate at a focal length of 7.5 meters and cover an energy range from 0.1 to 12 keV. At the prime focus is the European Photon Imaging Camera (EPIC). The third instrument on XMM-Newton is the Optical Monitor (OM), a conventional but highly sensitive optical/UV telescope. (Source: Barré et al. (1999))

XMM-Newton observed planets in the solar system and found that the X-rays emitted from their atmospheres are produced by interactions between the solar wind and neutral atoms in the planetary atmospheres (Bhardwaj et al., 2007). It also studied several binary pulsar systems, providing important evidence for the study of strong-field gravity and the state of dense matter. Additionally, XMM-Newton made significant contributions to understanding the formation and evolution of galaxy clusters (Snowden et al., 2008).

### XRISM

XRISM (Tashiro et al., 2018, 2020), known as the X-Ray Imaging and Spectroscopy Mission, is a collaborative project between JAXA and NASA, with ESA also participating. It is the successor to Hitomi, which was lost due to multiple failures in its attitude control system, leading to its disintegration. The mission aims to study X-ray celestial objects in the universe through high-throughput imaging and high-resolution spectroscopy. XRISM was successfully launched in Japan on September 7, 2023.

The XRISM observatory carries two scientific instruments: Resolve and Xtend. Resolve is the core instrument of XRISM, providing non-dispersive energy resolution of 5-7 eV in the 0.3-12 keV bandpass, with a field of view of approximately 3 arcminutes. It is capable of performing spectroscopic imaging. This high-resolution X-ray microcalorimeter array achieves its high-resolution spectroscopic imaging through the X-ray Mirror Assembly (XMA). Another important instrument is Xtend, a wide-angle X-ray imaging system that uses the same X-ray Mirror Assembly (XMA) as Resolve, thus covering the same energy band. Xtend consists of four CCDs arrays that extend its field of view to 38 arcminutes per side, covering the energy range of 0.4 to 13 keV. It was originally designed for Hitomi's Soft X-ray Imager (SXI) and was slightly adapted for the XRISM mission (Tashiro, 2022; Ishisaki et al., 2022) .

### Athena

Advanced Telescope for High ENergy Astrophysics (Athena) is a next-generation X-ray observatory that combines the largest X-ray telescope ever built with the most advanced scientific instruments. It is the second-largest mission in ESA's "Cosmic Vision 2015-2035" program and will enable deeper exploration beyond what XMM-Newton and Chandra have achieved, specifically to address the "Hot and Energetic Universe" science theme (Nandra et al., 2013). Athena uses a single telescope with a 2.5-meter aperture and a focal length of 12 meters, with an effective area of approx. 1.4 $m^2$ (at 1 keV) and 0.25 $m^2$ (at 6 keV) (Bavdaz et al., 2021).

The mission's payload includes an X-ray Integral Field Unit (X-IFU) and a Wide Field Imager (WFI). The X-IFU uses a microcalorimeter array based on Transition Edge Sensors (TES), operating at temperatures below 100 millikelvin (mK), enabling an X-ray energy resolution of 2.5 eV for energies below 7 keV. It is designed for high-resolution X-ray spectroscopy observations. The WFI uses a DEPFET (Depleted P-channel Field Effect Transistor) active pixel sensor, providing an energy resolution between 120 and 150 eV (Barcons et al., 2017).

### Insight-HXMT

The Hard X-ray Modulation Telescope (HXMT) is China's first X-ray astronomy satellite. It can achieve both wide-band, large-field-of-view X-ray surveys and study short-timescale variability and broad-band energy spectra of high-energy celestial objects like BHs and NSs. Simultaneously, it serves as an all-sky monitor (~60% of the sky) for gamma-ray bursts with a large effective area (0.2-3 MeV, ~1000 $cm^2$). The mission is equipped with three telescope payloads, corresponding to the high, medium and low energy bands, to achieve full coverage of the 1-250 keV energy range. The low-energy X-ray telescope (LE) (Chen et al., 2020) covers 1-15 keV, the medium-energy X-ray telescope (ME) (Cao et al., 2020) covers 5-30 keV, and the high-energy X-ray telescope (HE) (Liu et al., 2020) covers 20-250 keV. It was successfully launched into the planned orbit on June 15, 2017.

**eXTP**

The enhanced X-ray Timing and Polarimetry (eXTP) mission is a large-scale international collaboration project initiated and led by China, with participation from more than 100 research institutes across over 20 countries, including Italy, Germany, Denmark, Spain, Switzerland, France, the Czech Republic, and the Netherlands. Scheduled for launch in 2027 and currently in phase B, this space observatory is equipped with a variety of high-performance telescopes. These telescope arrays are capable of precisely measuring the X-ray energy spectrum, temporal variations, and polarization of celestial objects, as well as monitoring various transient celestial events, such as gamma-ray bursts and gravitational wave bursts. The eXTP mission is the topic of this thesis and will be discussed in detail in Chapter 2.

**STROBE-X**

The Spectroscopic Time-Resolving Observatory for Broadband Energy X-rays mission (STROBE-X) is a next-generation X-ray observatory proposed as a NASA mission concept, with significant contributions from European countries. The mission is designed to investigate the X-ray universe with unprecedented sensitivity, timing resolution, and energy coverage (Ray et al., 2024). The mission features wide energy coverage, ranging from soft X-rays (0.2 keV) to hard X-rays (30 keV), and offers high temporal resolution down to microseconds. This capability provides a unique advantage for studying rapid processes in compact objects. Additionally, the mission is equipped with a large-area detector and a wide field monitor, similar to those of eXTP. STROBE-X focuses primarily on the time-variable X-ray sky and its role as a multi-wavelength and multi-messenger observatory, serving the next generation of the astronomical community.

Numerous other missions have made pivotal contributions to X-ray astronomy, such

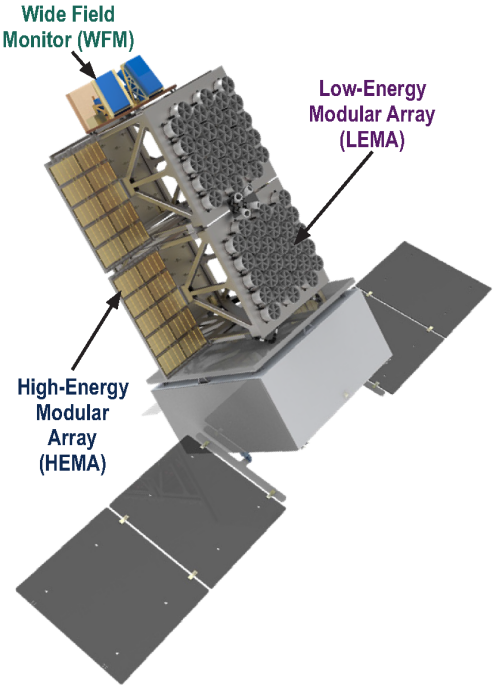


Figure 1.14: The baseline design of the STROBE-X mission is schematically summarized here. Wide Field Monitor (WFM) (Remillard et al., 2024) is mounted on a plate at the top of the Spacecraft. , while the High-Energy Modular Array (HEMA) and the Low-Energy Modular Array (LHMA) (Gendreau et al., 2024) are mounted on the side of the spacecraft.

as Japan's Suzaku, the Russian-German Spectrum-Roentgen-Gamma (SRG) mission, and several NASA observatories, which are not detailed here for brevity. For a more detailed list of historical missions, see the handbook written by Santangelo et al. (2023a).

## 1.3 Summary

X-rays are an important window for studying astrophysical under extreme environments and conditions, mainly because they can detect and reveal processes in the universe related to high-energy, violent, and extreme physical phenomena. These environments are often associated with extremely high temperatures, densities, magnetic fields, gravitational fields, and particle energies. Since humans began to explore the high-energy universe 70 years ago, research methods have evolved from rockets and high-altitude balloons to modern satellite observation platforms. Despite years of research and exploration, our study of the X-ray universe remains one of the frontiers in modern astrophysics and particle physics. Although many breakthrough discoveries have been made in high-energy cosmic phenomena after years of research, there are still many questions to be answered about the physics of black holes and phenomena near their event horizons, the equation of state inside neutron stars, the triggering mechanisms of explosive high-energy phenomena, the distribution of matter in galaxy clusters, and dark matter.

X-ray photons are detected based on three main interactions: the photoelectric effect, Compton scattering, and pair production. In the photoelectric effect, the incident photon is completely absorbed by the detector, knocking out a bound electron in the material and transferring its energy to the ejected electron. In Compton scattering, only a portion of the incident photon's energy is transferred to the recoil electron due to inelastic collisions, and the photon is deflected from its original direction. Finally, pair production refers to the interaction where a photon is annihilated, resulting in the creation of an electron-positron pair. Each of these three processes dominates in a different energy range: the photoelectric effect dominates at sub-kiloelectronvolt energies, Compton scattering dominates in the 100 keV to several MeV range, and pair production becomes the dominant interaction at higher energies, occurring only when the incident photon's energy exceeds 1.022 MeV. These three interactions are also the primary mechanisms for detecting high-energy particles. Therefore, understanding these physical interactions is crucial for the detection of high-energy particles.

For particle detection in different energy ranges, various types of detectors are required, which is determined by the interaction mechanism between particles and matter. Different energy ranges lead to changes in interaction mechanisms, thus affecting detector design and selection. Early gas detectors (such as the proportional counter and Geiger counter mentioned in the thesis) are widely used in X-ray detection because of their simple manufacturing, low cost and high efficiency. With the development of technology, the energy, time and spatial resolution of GSPC and solid-state detectors

(such as X-ray CCDs, SDDs, and microcalorimeters) have been significantly improved, which has greatly improved detection performance. In the high-energy X-ray range, scintillation detectors and MCPs compensate for the limitations of gas detectors and provide higher sensitivity and efficiency. As an emerging technology, microcalorimeters significantly improve energy resolution by accurately measuring temperature changes caused by incident high-energy particles. In addition, X-ray optical systems (such as Walter optics, polycapillary optics and encoded masks) effectively solve the problem of the failure of traditional focusing methods caused by the strong penetration of X-rays through grazing focusing and mask imaging methods, achieving high-energy High-resolution imaging of particles.

# 2 THE eXTP Mission

## 2.1 Science Case

Since its emergence in the 1960s, X-ray astronomy has opened new horizons for exploring high-energy astrophysical phenomena, revolutionizing our understanding of the universe. As a frontier field in modern astrophysics, this discipline probes fundamental physics in extreme relativistic systems: from spacetime curvature and accretion disk dynamics near black hole event horizons to strong-field quantum vacuum effects on neutron star surfaces; from observational tests of spacetime metrics in extreme gravity to laboratory tests of quantum electrodynamics in ultra-strong magnetic fields. The physical conditions involved far exceed the parameter space achievable in terrestrial laboratories. This disparity establishes X-ray astronomical observations as a unique natural laboratory for testing fundamental theories—including general relativity and quantum chromodynamics—under extreme conditions. Through multi-messenger observations of compact objects, this field drives theoretical innovation in fundamental physics under extreme conditions and continually expands the frontiers of knowledge.

Building on these foundations, the eXTP mission emerges as a transformative international endeavor. The eXTP is an international collaborative scientific mission to study the state of matter under extreme density, gravity and magnetic field conditions. The mission is equipped with a unique suite of scientific instruments, enabling the first simultaneous studies of spectral, timing, and polarization properties studies of cosmic sources in the energy range of 0.5-30 keV energy band.

The main scientific goals of eXTP include:

- Determine the Equation of State (EoS) of matter under ultra-nuclear density conditions.
- Measure Quantum electrodynamics (QED) effects in strongly magnetic star bodies.
- Explore the physical mechanism of accretion processes in strong gravitational

fields.

The core scientific goal of eXTP is to study the behavior of matter under such extreme conditions that cannot be achieved in Earth laboratories. Specifically, eXTP will focus on three key scientific goals.

These key scientific goals are:

- Studying the state of ultradense matter
- The physics and astrophysics of strong magnetic fields
- The accretion process in strong gravitational fields

To achieve these goals, the mission requires simultaneous, high-sensitivity observations across multiple observational parameters: high-throughput timing and spectroscopy to study neutron star oscillations (LAD), high-resolution spectroscopy to resolve atomic features in strong gravity (SFA), polarimetry to map magnetic field geometries (PFA), and a wide-field monitor to trigger on transient events (WFM). Consequently, the mission is equipped with a unique suite of scientific instruments.

### 2.1.1 Dense Matter in Neutron Stars

NSs are the densest stars in the observable universe. The density of their cores can reach more than ten times the density of atomic nuclei. It is the remnants after a supernova explosion caused by gravitational collapse. They have both extremely strong gravity and extremely high density, far exceeding any material we have created in the laboratory. "What Are the New States of Matter at Exceedingly High Density and Temperature?" was laid out in the 2002 US National Research Council report *Connecting Quarks with the Cosmos* Council et al. (2003), and its 11 big questions were featured on the cover of Discover Magazine as "the 11 greatest unanswered questions of physics." Haseltine (2002). This is a cutting-edge research in the cross-disciplinary field of nuclear astrophysics, which is of great scientific significance and value in unveiling multiple exotic states of matter, such as nuclear superfluidity, exotic matter (including hyperonuclear unblocked quarks), and color superconducting phases, in understanding and predicting the multi-messenger radiation of neutron stars, and to investigate the Quantum Chromodynamics (QCD) phase diagram in a region that current numerical methods are unable to access (Fukushima and Hatsuda, 2010).

Einstein's theory of general relativity links the dense matter EoS to the mass-radius relationship of NSs. eXTP will enable high-precision pulse profile modeling and spin measurements by observing the pulsations and QPOs of X-rays in accreting NSs, which will allow for precise determination of the mass and radius of the NS, which are the key parameters for unraveling the dense matter model. Since eXTP also carries a polarization measurement instrument, the PFA, this will further reduce the simplicity of these parameters and thus improve the accuracy of the measurements. eXTP can also further constrain the EoS of NSs by measuring their spin frequencies.

### 2.1.2 Physics and Astrophysics of Strong Magnetic Fields

As an important category of compact objects, magnetars are valuable for research due to their unique properties under extreme physical conditions. This special type of neutron star has two hallmark features: surface magnetic field strength reaches the order of ($B \sim 10^{12-13}$ Gauss), and the X-ray radiation behavior exhibits significant changes. Typical observational phenomena include frequent bursts that exceed the Eddington limit in the X-ray and soft gamma-ray bands, some of which produce medium-intensity or even giant flares. At present, observational records show that only four magnetars have been confirmed to have radio radiation characteristics. Pulsars are rotating magnetized NS, one of the most fascinating objects in astrophysics due to their potential as physics laboratories under extreme conditions. Pulsars exhibit a variety of phenomena and form different classes based on key parameters such as rotational period and magnetic field strength. Figure 2.1 reveals the evolutionary paths of different types of celestial bodies through the distribution map of pulsar rotation periods and period derivatives. The contour lines marked in the figure intuitively reflect the dynamic correlation between characteristic age and magnetic field strength.

Observational data show that magnetars mainly present two forms: Anomalous X-ray Pulsars (AXPs) with a stable rotation period in the range of 1 to 10 seconds and Soft Gamma-ray Recurring sources (SGRs). In order to further study its physical mechanism, the eXTP, which is about to be put into operation, will play a key role. The satellite system captures magnetar burst signals in real time through the WFM, and conducts deep observations in coordination with the SFA and the LAD. With its high sensitivity and wide field of view, the system not only significantly improves the detection efficiency of burst events, but also provides decisive evidence for revealing the three-dimensional configuration of the magnetic field and the energy release mechanism through precise time-varying data analysis and multi-band spectral analysis.

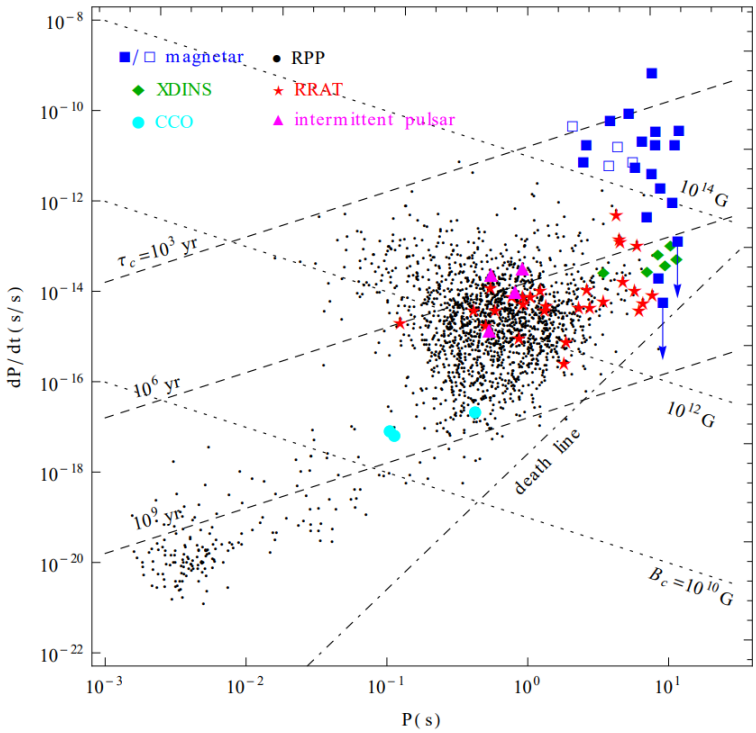


Figure 2.1: Period and period derivative diagram of pulsars (Tong, 2016).

### 2.1.3 Accretion Process in Strong Gravitational Field

Another eXTP research topic is the structure of accretion disks near the event horizon of black holes, revealing the dynamics of accretion disks and the spin of black holes by observing relativistic iron line and high-frequency QPOs. Relativistic iron line are important tools for studying black hole accretion disks. eXTP will use its SFA and LAD to perform high-precision spectral and time-resolved observations of relativistic iron line to study the dynamics of accretion disks and the spin of black holes. These observations will provide a deep understanding of physical processes in strong gravitational fields. eXTP will use its highly sensitive detectors to study the QPOs of accreting black holes and accreting neutron stars. By measuring the frequency and waveform of QPOs, the dynamics of accretion disks and the spin of black holes can be revealed. The high time resolution of eXTP will enable the first coherent detection of low-frequency QPOs and the study of their phase-dependent spectral shapes.

### 2.1.4 Other Frontiers in Astrophysics

Since the groundbreaking gravitational wave event GW170817 in 2017, multi-messenger astronomy has developed rapidly. As of the time of writing this thesis, GW170817 is still the only gravitational wave detection event that is clearly linked to electromagnetic

observations. The WFM and other highly sensitive imaging equipment aboard the eXTP will make it an important electromagnetic follow-up observation platform for gravitational wave events. In the future, when LIGO/Virgo/KAGRA or Einstein Telescope detects a compact binary coalescences, eXTP will rapidly respond to localize associated GRBs via WFM, while its SFA and LAD will perform high-resolution spectroscopy and polarimetry on jet afterglows. These observations will be crucial for revealing the jet morphology, energy release mechanisms, and magnetic field configuration, thereby bridging the information gap between gravitational-wave and electromagnetic observations.

High-energy astrophysical phenomena often show instantaneous sudden outbursts or extreme variability. eXTP's all-day monitoring and rapid response capabilities make it an ideal platform for transient source detection. The WFM is expected to detect a large number of GRBs, tidal disruption events (TDEs), and short-timescale AGN flares. In particular, in TDEs, the high-energy radiation from stars torn apart by supermassive black holes can reveal the entire process of accretion disk formation and jet initiation through eXTP's imaging and polarization observations. In addition, eXTP can track the state transition of "Changing-look AGN" in real time to study the accretion flow dynamics and the interaction between jets.

The mission will monitor the high-energy activities of a large number of flaring stars, which will help to further study stellar magnetic fields and atmospheric dynamics. The X-ray radiation released by flares will be recorded by SFA and LAD to analyze magnetic field reconnection and high-energy particle acceleration processes. This type of data is crucial to understanding the evolution of stellar magnetic fields and activity cycles. Concurrently, by evaluating the impact of stellar radiation on planetary atmospheres, eXTP will provide observational support in the field of planetary habitability and space weather, and make important contributions to exoplanet research.

eXTP high-resolution imaging and polarimetry will unravel the internal structure of SNRs, which is expected to reveal the propagation of shock waves, magnetic field distribution, and high-energy particle acceleration mechanisms. Through spatially resolved polarization measurements, eXTP can determine the non-thermal radiation region and magnetic field direction, providing direct evidence for studying the acceleration source and energy spectrum characteristics of cosmic rays. In addition, eXTP can observe the rapid evolution of young SNRs, providing a time evolution perspective for understanding the end-states of stellar.

The mission will conduct multi-scale and cross-mass level systematic observations of various accretion systems. From accreting white dwarfs (such as cataclysmic variables

and intermediate polarized stars) to quasars (AGN and high-redshift QSOs), eXTP has high-sensitivity observation capabilities. In white dwarf systems, eXTP will reveal the complex relationship between magnetic fields and accretion dynamics; in quasars, X-ray reflection and polarization data will be used to analyze disk wind dynamics, accretion rate changes, and jet initiation mechanisms. These observations will promote the fine modeling of accretion physics and disk wind theory.

Polarimetry serves as a crucial diagnostic tool for probing radiation mechanisms and source geometry. The PFA will measure polarization degrees and angles across diverse targets including GRBs, magnetars, and AGNs. Such measurements will possible to determine whether the radiation is dominated by synchrotron radiation, Compton scattering, alternative radiation mechanisms, and reconstruct the magnetic field topologies. Furthermore, precision polarimetry measurements are expected to find signs of Lorentz invariance breaking or large-scale symmetry breaking in the universe, and explore the limits of basic physical laws.

Through long-term monitoring, eXTP will accumulate vast datasets enabling discovery of rare or novel high-energy phenomena, e.g., intermediate-mass black holes (IMBHs), fast X-ray transients (FXTs), new gamma-ray bursts, etc. may all be discovered in the field of view of eXTP. Combined with data from other bands and detection methods, eXTP will realize multi-band and multi-messenger joint analysis, open up a new model of collaborative observation and data fusion, and promote the comprehensive development of high-energy astrophysics.

## 2.2 The eXTP Mission Design

During the final stages of this thesis work, the eXTP mission configuration underwent modifications due to external constraints. A key outcome of this update was the exclusion of the originally planned European instrument contributions. Consequently, the LAD and WFM, as described in this thesis, are no longer part of the eXTP payload. Nevertheless, the pre-update configuration presented here remains scientifically valid and serves as a valuable reference for other mission concepts in the future of the X-ray and gamma-ray astronomy.

### 2.2.1 Overview

The eXTP (Figure 2.2) is a flagship Sino-European next-generation space X-ray mission, currently in its Phase B study. It is led by the Institute of Institute of High

Energy Physics (IHEP) of the CAS, with significant contributions from European partners. The European consortium comprises over 100 scientific research institutions across more than 20 countries, including Italy, Germany, Denmark, Spain, Switzerland, France, the Czech Republic, and the Netherlands. The eXTP mission scientific payload includes four science instruments: the Spectroscopy Focusing Array (SFA), the LAD, the Polarimetry Focusing Array (PFA), and the WFM. According to the cooperation plan, China will undertake the space segment of the mission, including payload support, the service module, and payload integration. China will also provide the SFA and PFA instruments, while Europe is expected to contribute to the SFA and PFA focal plane cameras. Additionally, China will be responsible for the launch missions, telemetry and control systems, as well as the management of operations and scientific ground systems. The LAD and WFM instruments will be provided by the European segment of the eXTP consortium, which essentially comprises all the countries involved in the LOFT (Feroci et al., 2012) study.

China is take primary responsibility for the overall design, development of the mission.

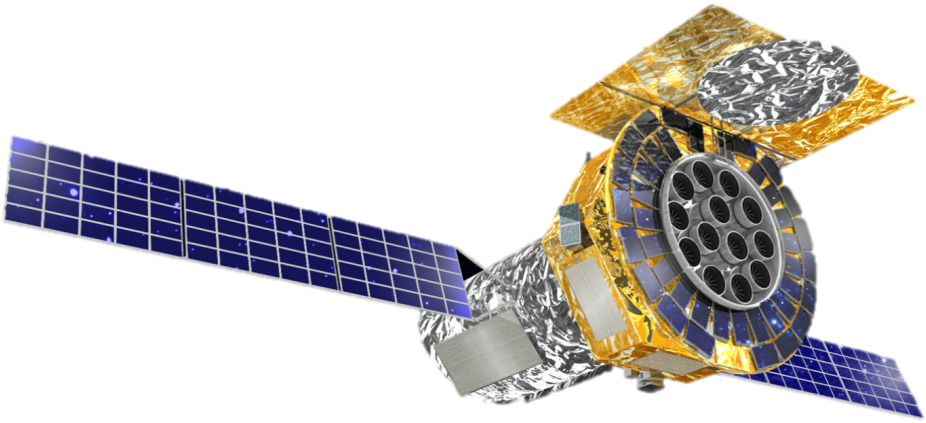

Figure 2.2: Artistic view of the eXTP spacecraft. The four instruments included: the focused SFA and PFA telescopes arrays, the LAD, and the WFM (Zhang et al., 2022).

The mission is structured into six key systems according to the Space Science Programs of China:

- **Satellite System** China will be responsible for the platform and the satellite's Assembly, Integration, and Testing (AIT). The eXTP mission satellite will feature a Chinese platform supporting the eXTP payloads, provided by the Innovation Academy for Microsatellites of the Chinese Academy of Sciences (IAMC).

- **Launcher System & Launch Site System** The eXTP mission is planned to be launched by the Long March 5 (CZ-5) rocket from the Wenchang Space Launch

Site in Hainan, China. The target orbit is proposed to be a low-Earth orbit at an altitude of approximately 550 km. With an orbital inclination of 2.5 deg, the mission enables instruments to operate in a low particle density environment, ensuring the energy resolution of LAD and reducing background noise caused by radiation degradation and particle-induced. The satellite carries propellant for orbit maneuvers and maintenance during the mission, with additional reserves to ensure successful de-orbiting.

- **Telemetry, Tracking, and Command (TT&C) System** The telecommunications architecture includes four types of communication links between the satellite and the ground station: the S-band data link, X-band data link, Beidou short message link, and Very High Frequency (VHF) stations (inherited from the China-France Space Variable Objects Monitor (SVOM), launched in June 2024). The S-band section supports satellite TT&C, while the X-band section supports the downlink of scientific data. The Beidou short message link enables the rapid uplink of Target of Opportunity (ToO) observation tasks. Both the Beidou and VHF networks will be utilized for the real-time downlink of WFM burst information.

- **Ground Support System & Science Application System** The spacecraft serves as the space-based segment of the eXTP mission and requires significant support from ground-based systems for its operation. The ground segment of the eXTP mission is divided into three main components: (1) TT&C; (2) the Operational Ground Segment (OGS); and (3) the Science Ground Segment (SGS).

  The TT&C segment collects and transmits data regarding the satellite's housekeeping, status, and operational parameters to ground stations for monitoring and verification of the spacecraft's health.

  The aim of OGS is to provide mission control and it is composed by the Mission Operation Center (MOC) and by two primary ground stations for telemetry reception: the Sanya ground station in China and the Malindi ground station in Europe, both of which will be equipped with X-band receivers and transmitters. The MOC, managed by the National Space Science Center (NSSC) of CAS which will be in charge of receiving the instrument telemetry and instrument housekeeping data. It will decode and process the data into a manageable format for further analysis, quick-look activities, archiving, and distribution by the SGS. The MOC will also be responsible for converting mission observation programs

provided by the SGS into specific telecontrol commands and transmitting them to the TT&C segment for uplink transmission in transparent mode.

The SGS comprises the Science Support Center (SSC), the Science Operation Center (SOC), and two Science Data Centers (SDCs). The SSC will receive ToO observation requests and assist in coordinating multi-wavelength and multi-messenger joint observation programs. Additionally, the SSC is responsible for developing auxiliary documentation and software tools, as well as performing validation of final mission data and auxiliary files. Subsequently, the SSC will provide all these products to the scientific community through the NSSC's central mission archive.

The SOC is primarily responsible for developing the annual mission observation plan and monitoring the status and performance of the payloads. The SDCs in China and Europe will provide analysis software to process data from the scientific payloads and generate predefined scientific products. These products will be used for quick-look activities.

Data from the onboard burst alert system of the WFM will be downloaded through 15 VHF ground stations deployed around the equator. Bright burst event alerts will be transmitted to the ground and the scientific community within 0.30 seconds. These ground stations are inherited from the SVOM. Alternatively, alerts can be transmitted via China's Beidou Navigation Satellite System or through the short messaging service of the relay satellite communication system.

The system-level product tree of the eXTP is illustrated in Figure 2.3, outlining its major subsystems, components, and their relationships. As previously mentioned, key components and responsibilities are identified, along with the division of contributions between China and Europe, where yellow boxes represent China's contributions and blue boxes represent Europe's.

### 2.2.2 The Spacecraft

The satellite consists of three modules: the Optical Module (OM), the Platform Module (PM), and the Detector Module (DM). The mission is divided into independent functional modules to optimize the AIT process. The satellite design adopts a "centralized around payload" concept, where the payload is positioned at the centre, and the satellite platform is installed around it. This approach primarily considers the length of the satellite's OM. The satellite' s dimensions are constrained by the rocket fairing, with a maximum diameter of 4600 mm and a height of 8835 mm. The PFA &

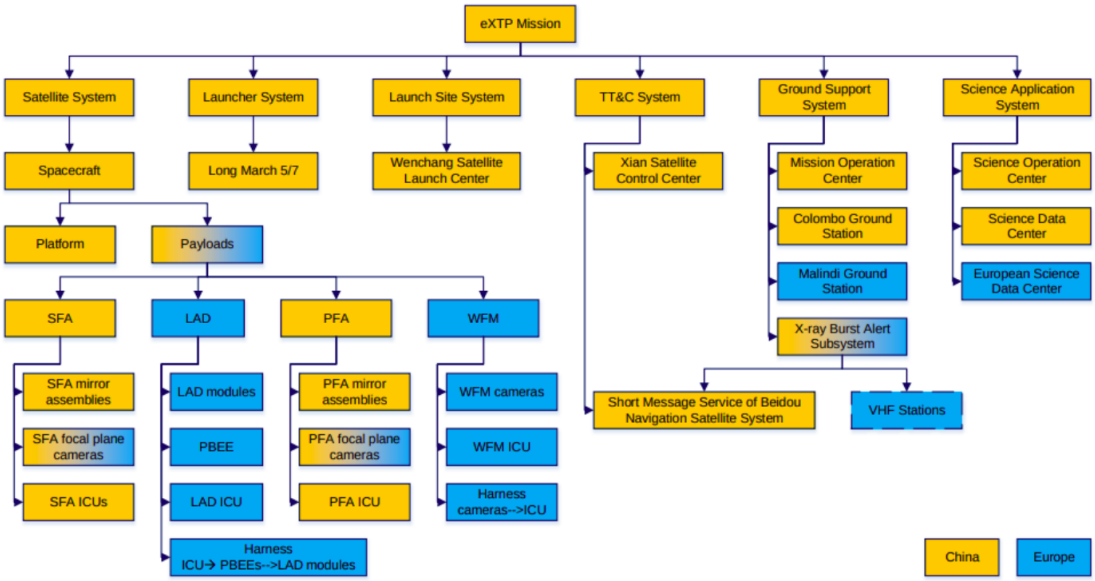


Figure 2.3: Schema of the eXTP mission system-level product tree (Zhang et al., 2022).

SFA focal length and the detection area of the LAD are limited. Both the SFA and PFA utilize grazing-incidence Wolter-I optics X-ray telescopes with a focal length of 5250 mm for focusing.

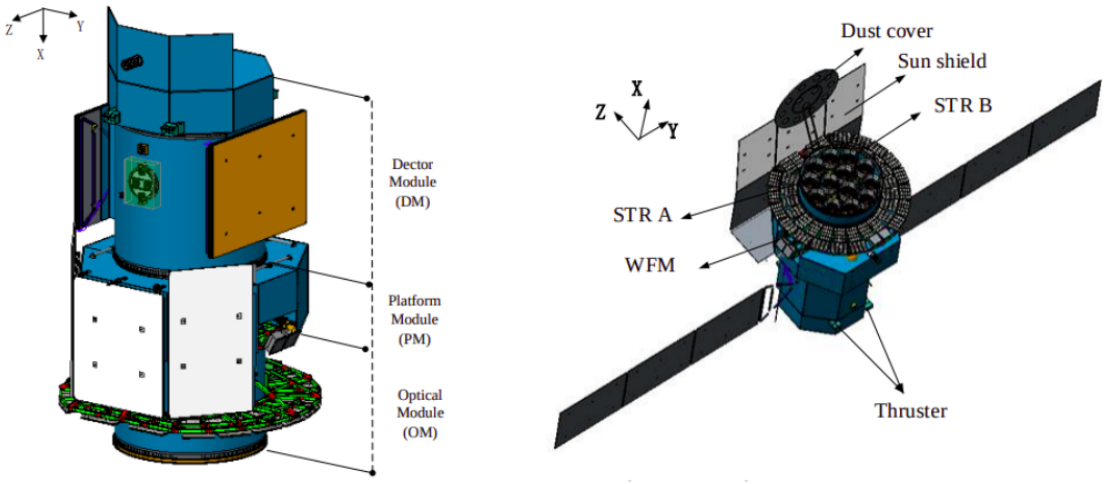


Figure 2.4: The in-flight configuration of the eXTP mission satellite (Zhang et al., 2022).

The mirror assemblies of the SFA and PFA, the LAD modules, and the star trackers are mounted on a framework integrated with the OM. Their alignment is maintained coaxially to enhance the overall sensitivity of the mission. The LAD is installed on an annular frame surrounding the mirror assemblies of the SFA and PFA. At the DM, 13 focal plane cameras for the SFA and PFA are mounted, equipped with sunshades to

protect the detectors from solar radiation, as shown in Figure 2.4.

The satellite employs a three-axis stabilized zero-momentum attitude control system, offering multiple pointing modes, including inertial pointing, solar pointing, and attitude maneuvers. It is equipped with eight reaction wheels as the primary actuators for attitude control, capable of achieving a 30° reorientation within 600 seconds. For high-precision inertial pointing, the system integrates high-precision star trackers, gyroscopes, and reaction wheels. Additionally, the satellite features four 10N thrusters to facilitate orbital maneuvers during initial deployment, orbit maintenance, and debris avoidance. With a designed operational lifespan of 8 years, the satellite ensures consistent and reliable mission performance.

The power supply system of the eXTP satellite primarily consists of two solar panel arrays and a battery pack. Two solar panel arrays, with a total area of approximately 27 square meters, will be installed as shown in the Figure 2.2 and Figure 2.4. The battery pack, comprising lithium-ion batteries with a total capacity of 300 Ah, is designed to meet the power requirements during the launch phase and in safe mode.

### 2.2.3 Observing Strategy

As a powerful international collaborative astronomical project, eXTP boasts excellent spectral resolution, wide-field sky coverage, polarization measurement capabilities, and high data throughput. A comprehensive observation strategy has been developed to fulfill the mission's dual objectives: serving as a specialized scientific instrument and a versatile astrophysical observatory. This strategy integrates targeted observations, large-scale surveys, and rapid response capabilities to maximize the scientific output and ensure the mission achieves optimal results. The mission also aims to provide open access to the scientific community while ensuring that funding institutions and participating countries receive the corresponding scientific data.

As an open space-based observatory, eXTP observation time will be allocated annually through calls for proposals and scientific peer review. The mission is designed to respond swiftly to transient events (e.g., bursts) and execute flexible ToOs. Scientists can propose ToOs beyond the source state changes defined in guest observer programs and key projects. The eXTP PI will decide on scheduling proposed observations after consulting relevant members of the Observing Time Allocation Committee (OTAC). Depending on the nature of the ToO, a one-year proprietary data rule may be applied, or the data may be made available to the entire scientific community.

For pointed instruments, a standard one-year proprietary data period is assumed, after

which all data will be made publicly accessible. For the WFM, no proprietary data rights are applied, and its data will be made available to the community within a much shorter timeframe.

The eXTP satellite is designed to observe celestial objects in inertial space, based on the requirements for scientific observations and on-orbit calibration. The satellite's observation modes primarily include routine observations, follow up observations, ToO, and small-sky scanning modes.

- **Routine observation mode** Conduct observations according to pre-planned observation objectives.

- **Follow-up observation mode** Dedicated to rapid response to unexpected astrophysical events, eXTP is designed to conduct initial observations of afterglows from explosive sources, such as X-ray bursts and flares. The system includes automatic repointing to the burst immediately after triggering and an automatic return to the previous pointing. These features provide eXTP with rapid turnaround capabilities and flexible scheduling, ensuring efficient and timely observations.

- **ToO** This includes ToO observations scheduled by ground systems based on astronomical events and additional calibration requests, all subject to time delay constraints. Observation plans must be uploaded within a few minutes.

- **Small-sky scanning modes** This mode is typically used for the calibration of the Point Spread Function (PSF) or vignetting function of instruments such as SFA, LAD, and PFA. It involves scanning an X-ray source over a range of $\pm 2$ degrees.

The eXTP mission is planned for a minimum mission lifetime of 5 years, with the possibility of extending the mission by an additional 3 years to a total of 8 years, based on mission requirements.

The mission operations will be divided into 5 phases, with the objectives for each phase described as follows:

- **Launch and Early Orbit Phase (LEOP):** This phase begins with the satellite launch and involves maneuvering it into its operational orbit. During this stage, satellite and instrument systems are powered on and checked.

- **Commissioning Phase:** Starting immediately after the LEOP phase, this

phase typically lasts up to 3 months. It involves detailed testing and calibration of the systems to prepare for routine operations.

- **Nominal Operations Phase:** Spanning 5 years, this is the primary mission phase during which scientific observation plans are executed, aiming to achieve core and key scientific objectives.

- **Extended Operations Phase:** If the satellite continues to collect valuable data, this phase extends the mission for an additional 3 years or any other agreed-upon duration as determined by the stakeholders.

- **Decommissioning Phase:** This is the final phase, during which controlled satellite reentry procedures are executed to comply with casualty risk regulations, ensuring a safe conclusion to the mission.

## 2.3 The eXTP Scientific Payload

The eXTP originates from the merger of two major mission concepts: China's X-ray Timing and Polarization (XTP) mission and Europe's LOFT. The eXTP project's SFA and PFA instruments evolved from those developed for XTP, while the LAD and WFM instruments were inherited from the LOFT mission and adjusted to align with the objectives of the eXTP project. A detailed introduction to each instrument is provided below. While the LAD is the main topic of this thesis, it will be discussed in detail in the following chapter.

### 2.3.1 Spectroscopic Focusing Array - SFA

The SFA comprises of an array of 9 identical Wolter-I X-ray telescopes (see Figure 2.6) designed for spectroscopic and timing observations in the energy range of 0.5-10 keV featuring a total effective area larger than 6000 $cm^2$ at 1-2 keV, the comparison of SFA with others telescope is showen in Figure 2.5. The telescopes consist of the mirror module, the electron deflector, the filter wheel, and the focal plane camera. The Wolter-I mirror assembly has a focal length of 5.25 meters. They achieve an energy resolution of 180 eV at 6 keV and a time resolution better than 10 $\mu$s, with a dead time expected to be below 5% at 1 Crab. Each telescope is equipped with a thermal shield to maintain the mirror assembly at the required operating temperature of 20 $\pm$2 ℃. An electronic deflector is installed at the bottom of the mirror module to mitigate the impact of particle background on the detector.

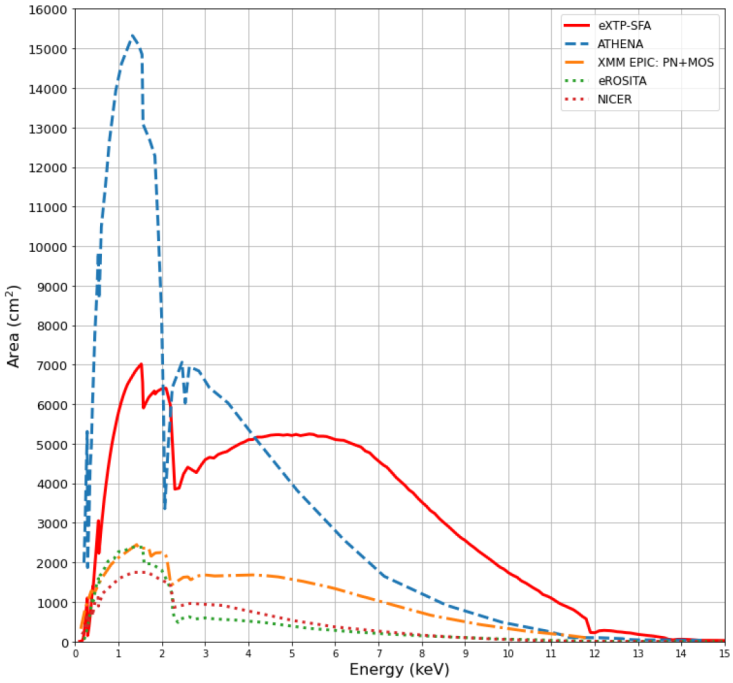


Figure 2.5: Comparison of the total effective area between the SFA and other X-ray focusing telescopes (Zhang et al., 2022).

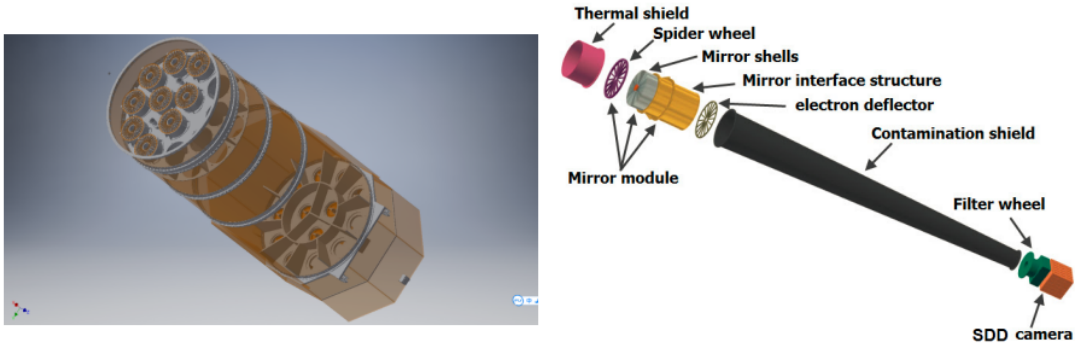


Figure 2.6: Left: Layout of the nine SFA telescopes (with four empty slots reserved for PFA telescopes); Right : Schematic structure of a single SFA telescope (Zhang et al., 2022).

The optical design and interface of the SFA and PFA are nearly identical to simplify the design process, facilitate engineering implementation, and reduce mission risks. The weight budget for the optical modules is 50 kg for SFA and 100 kg for PFA. The electroforming replication process is employed to manufacture the mirror shell, considering factors such as performance, weight, space environment, and cost. This technology, developed by National Institute for Astrophysics (INAF) in collaboration with Media Lario[1], has been implemented in several advanced X-ray telescopes (Citterio

[1]Media Lario is private italian company which produces optical components and systems, custom-

et al., 1986; Burrows et al., 2005; Predehl et al., 2014; Pavlinsky et al., 2014; Ramsey, 2017; Yuan et al., 2018). The process begins with creating an aluminum mandrel with a negative mirror profile (parabola + hyperbola) for each mirror shell. A 0.100 mm layer of Kanigen coating is electrochemically applied. Kanigen is particularly suitable for super polishing by grinding, producing an extremely smooth surface, which is essential for high-quality mirrors. A thin layer of gold is then deposited on the polished mandrel surface to prepare for the subsequent deposition of nickel. Nickel is applied using an electroforming process to form a metal layer that precisely replicates the mandrel profile. Finally, the mirror shell is cooled and separated, based on the differences in thermal expansion coefficients between the various metals. To enhance reflectivity for X-rays with energies below 5 keV, a carbon coating is deposited on the gold surface (Jin et al., 2020). The main difference between SFA and PFA is the reflective coating. The baseline design of SFA uses a gold-plated electroformed nickel shell, while PFA uses a direct electroformed nickel shell. The primary technical specifications are provided in Table 2.1.

Table 2.1: Key specifications of the SFA/PFA mirror module

| **Parameters** | **Specification for one mirror module** |
|---|---|
| Focal length | 5250 mm |
| Energy range | 0.5 - 10 keV (SFA)<br>2-8 keV (PFA) |
| On-axis collecting area | $\geq$600 cm$^2$ at 1.5 keV (SFA)<br>$\geq$800 cm$^2$ at 3 keV(PFA)<br>$\geq$550 cm$^2$ at 6 keV |
| Angular resolution (HPD) | $\leq$1' (SFA)<br>$\leq$30" (PFA, goal 15" ) |
| Energy range | 0.3-10.0 keV |
| Reflection surface | Surface material: gold (SFA), nickel (PFA)<br>Micro roughness $\leq$0.5 nm (rms) |
| Envelope dimension | Diameter $\leq$600 nm |
| Total Weight | 125 kg |
| Working temperature | 20 $\pm$ 2 ℃ |

The Wolter-I mirror assembly consists of 45 nested mirror shells, each comprising a coaxial and confocal paraboloid and hyperboloid, with an angular resolution requirement of less than 1 arcmin of half-power diameter (HPD) [2]. The assembly is installed

made or in high volumes for Space Telescopes, Satellite Earth Observation Systems, Laser Optical Communications Systems.

[2]Often used to describe the resolution of a telescope or optical system. It represents the area in which the optical system can effectively focus light, and is often related to the "spread" of the beam, especially in optical imaging systems. Specifically, the half-power diameter is the angular diameter at which the intensity of the point spread function (PSF) of the system is reduced to half of its maximum value.

on the satellite's optical bench, as illustrated in the left of Figure 2.6. Each SDD array consists of 19 hexagonal cells with a side length of 3.2 mm and an effective thickness of 450 µm. The inner 7 cells of the array is used for detecting X-rays from celestial sources, while the surrounding cells are utilized to capture background signals. The side length of the hexagonal cells is designed to match the expected angular resolution of the optics. The thickness is optimized to ensure excellent quantum efficiency within the energy range of the SFA. A thin aluminum layer with a thickness of about 80 nm is applied to the silicon sensor entrance window to block incoming photons. The prototype detector module for the SFA was fabricated by the Max-Planck-Institut für Extraterrestrische Physik in Garching, Germany, in collaboration with the Max-Planck-Gesellschaft Semiconductor Laboratory (HLL). The mechanical design of the detector module is shown in Figure 2.7.

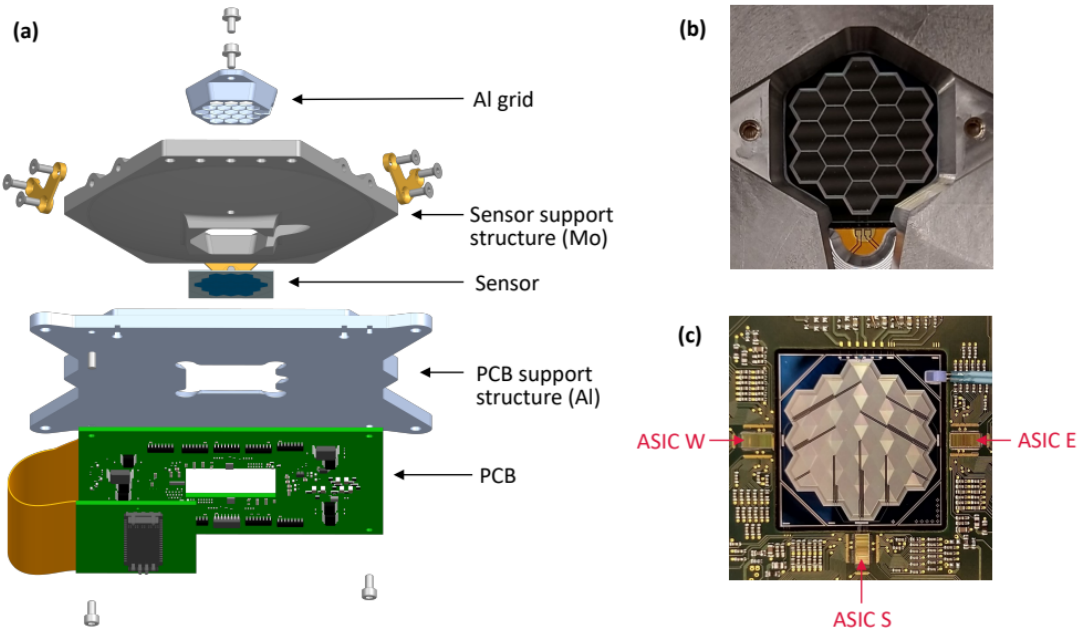


Figure 2.7: **(a)**The detector module consists of two metal support structures connected by gold-coated PEEK (Polyether ether ketone) standoffs for thermal isolation. The silicon sensor is fixed to the upper support structure, which is made of molybdenum, while the lower support structure is made of aluminum and houses a PCB containing the front-end electronics (FEE). **(b)** shows the entrance window side of the 19-pixel silicon drift detector, located at the center of the detector module. **(c)** displays the front view of the sensor, with the three High Time Resolution Spectroscopy (HTRS) Application-Specific Integrated Circuits (ASICs) used for detector signal readout clearly marked. Each sensor pixel is connected to the corresponding channel of the HTRS ASIC via aluminum bond wires. (Figure: (Altmann et al., 2024))

The Printed Circuit Board (PCB) houses the Front-End Electronics (FEE) (see Figure

2.7), with the three HTRS ASICs being the most critical components, responsible for reading out all 19 pixels. The design of the FEE for each SDD pixel signal processing chain includes a charge-sensitive preamplifier, a fast shaper, and a slow shaper with a sample-and-hold circuit. Since the central SDD pixel focuses most of the incident photons, a dedicated readout ADC circuit is implemented to minimize readout dead time. Meanwhile, the remaining pixels are multiplexed to simplify the readout process. An Field Programmable Gate Array (FPGA)-based Back-End Electronics (BEE) module is implemented to control the FEE, and readout the digitized data from the Analog-to-Digital Converters (ADCs). It also plays an important role in recording the signal amplitude and arrival time of each incident X-ray photon and sending it to the spacecraft data processing subsystem for temporary storage and telemetry. The FPGAs also generates the instrument's internal data packet, which includes key parameters such as the count rate of each cell, the survival time of the readout circuit, and the operating temperature of the cell.

The Filter Wheel is located above the detector. In order to adapt to various observing conditions, the filter wheel is equipped with four operating positions:

- **Open filter** Utilized for ground testing and observations of faint sources;
- **Calibration** An $^{55}$Fe radioactive source is employed for in-orbit calibration;
- **Optical blocking filter** This filter, composed of a 400 nm polyimide layer and a 200 nm aluminum film, serves to block visible and UV light while also protecting the detector from contamination;
- **Closed filter** A metal shutter is employed to measure the internal background and to protect the detector from potential damage during launch and extreme solar events.

### 2.3.2 Polarimetry Focusing Array - PFA

The PFA is composed of 4 identical telescopes designed for X-ray imaging polarimetry, with sensitivity in the 2-8 keV energy range. The PFA is the only instrument on eXTP that provides high imaging resolution, achieving better than 30 arcseconds, while offering excellent temporal and spatial resolution. This capability helps discriminate and remove source confusions occurring in other instruments. For a 1 ks observation of the Crab Nebula, the PFA can achieve a polarization measurement sensitivity as low as 3%. At 3 keV, the total effective area of the PFA exceeds 300 cm$^2$. The expected

effective area, compared to IXPE, is shown in Figure 2.8. The main features of the PFA optics have already been discussed in section 2.3.1. The PFA parameters and specifications are listed in Table 2.1.

The 4 PFA telescopes share the same optical design as the SFA (Section 2.3.1), though the PFA requires significantly better angular resolution. The mirror module configuration is identical to that of the SFA, except that the reflective surface is made of nickel instead of gold.

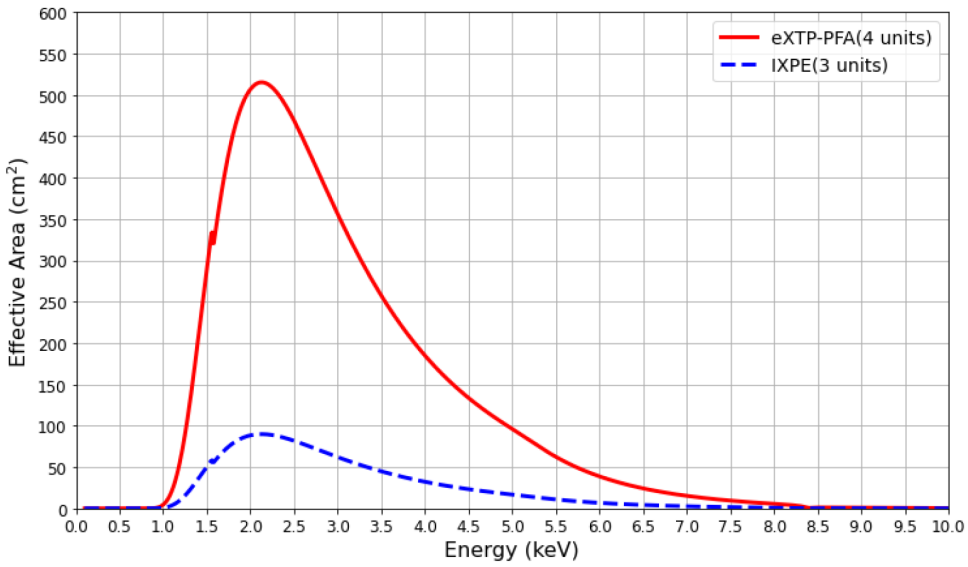


Figure 2.8: Comparison of the total effective area between PFA and IXPE (Zhang et al., 2022).

The focal plane camera comprises detector and electronics boxes, the Gas Pixel Detector (GPD) is adopted as the focal plane polarimeter for the PFA. The GPD was invented and developed by the Italian National Institute of Nuclear Physics (INFN)-Pisa group, with its principles extensively detailed in references (Bellazzini et al., 2003; Muleri et al., 2008; Bellazzini et al., 2013; Costa et al., 2001).

The event detection process of the GPD proceeds as follows: An incident X-ray goes though one of the holes of the collimator (Section 1.1.3), penetrate 50 $\mu$m thick beryllium sealed window. Once it enters the detector chamber, it interacts with the working gas (Dimethyl Ether (CH3-O-CH3) at 0.8 atm) of the GPD. Based on the photoelectric effect, a photoelectron is emitted when an X-ray photon is absorbed by an atom.

As the photoelectrons propagate through the gas, they further ionize surrounding gas molecules, generating primary electrons and positive ions. The shape and orientation of the ionization trajectories preserve the polarization information of the X-rays.

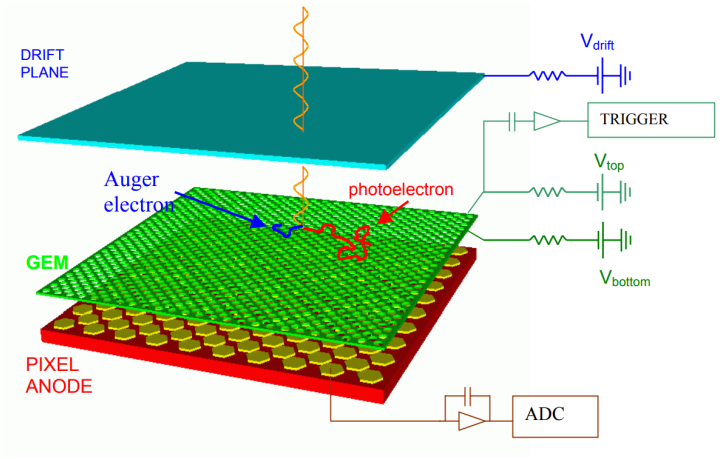


Figure 2.9: Working principle of a Gas Pixel Detector. (Figure: (Costa et al., 2001)) The full track is used to determine the polarization information of the incoming X-ray photons by specifically the polarization degree and polarization angle.

Under the influence of a parallel electric field, the primary electrons drift toward the anode. When these electrons pass through the tiny apertures of a Gas Electron Multiplier (GEM), an avalanche multiplication effect occurs, producing a large number of secondary electrons that significantly amplify the electrical signal. The GEM gain factor can be adjusted by controlling the high voltage between its top and bottom layers. The amplified secondary electrons continue to drift along the electric field and eventually reach the anode plane, which consists of a pixelated ASIC (Bellazzini et al., 2004, 2006) chip with a pitch of 50 $\mu$m. The ASIC chip is responsible for collecting and measuring the multiplied charge signals. Its effective area of 1.5 cm $\times$ 1.5 cm defines the detector's sensitive area, and it achieves a readout charge noise of approximately 50 $e^-$. At an X-ray energy of 6 keV, the energy resolution of the detector is 15% – 20%, consistent with the typical performance of gas detectors.

The electronics boxe is primarily designed for the accommodation of the BEE, with its key functions including:

- **ASIC Control and Operation**: Drives ADC conversion for high-precision data acquisition
- **Satellite Communication**: Handles the packaging and transmission of scientific data, as well as receiving and executing commands.
- **System Management**: Performs housekeeping tasks and manages the secondary power supply.
- **Active Thermal Control for GPD**: Manages the thermal control of the GPD,

maintaining required optimal operational temperature.

### 2.3.3 Wide Field Monitor - WFM

The WFM is another instrument contributed by the European consortium, with the capability to simultaneously observe approximately one-third of the sky in the same energy band as the LAD instrument. The primary role of the WFM is to identify sources for further observations with the LAD, SFA, and PFA (Hernanz et al., 2018). To achieve this goal, the WFM is designed to have maximum overlap with the sky accessible to LAD, SFA, and PFA. The object source of the WFM including new transients and known sources undergoing spectral state changes.

The scientific topic of the WFM is provide triggers for the "narrow field of view" instruments of eXTP: SFA, LAD, PFA for the depth observation. It also provides alerts about the outbursts of relevant sources, indicating whether they are new or recurrent and already known. The WFM also has its own scientific objectives, such as monitoring the long-term behavior of interesting X-ray sources, detecting short bursts (0.1 – 100 seconds), and recording data at full resolution. As well as providing alerts for GRB, gravitational wave events electromagnetic, Fast Radio Bursts.

The WFM is an imaging instrument with a point source location accuracy of 1 arcminute, designed to match the required on-target pointing accuracy for LAD observations. It is based on the coded mask (see section 1.1.3) technique design, which has been successfully utilized by several instruments in past and ongoing X-ray missions, such as BeppoSAX, INTEGRAL, AGILE, and SWIFT, as mentioned in the previous chapter. The main scientific requirements of the WFM are listed in Table 2.2, (see also the eXTP/WFM papers Hernanz et al. (2018, 2022, 2024).

The WFM is a coded aperture imaging instrument designed with a modular approach, consisting of six identical cameras and each camera includes four large area SDDs. Each set of two cameras forms a camera pair and covers the same FoV, enabling a fine 2D angular resolution. The response of a single camera is highly directional, offering high angular resolution along the X-axis while exhibiting lower resolution along the Y-axis. By merging the outputs of two co-aligned cameras oriented 90° relative to one another around their shared viewing axis, the system achieves high-resolution two-dimensional imaging. The WFM is equipped with the same working principle as the SDDs used in the LAD. However, the detectors of the WFM are specifically designed with a smaller anode pitch (169 $\mu$m in the WFM versus 970 $\mu$m in the LAD) to optimize their imaging properties in conjunction with the coded mask. The structure design of an individual WFM camera is based on the classical design of the

Table 2.2: Scientific requirements of the WFM instrument

| **Parameters** | **Requirement** |
|---|---|
| Point source localization (confidence level 90%) | 1 arcmin |
| Angular resolution | 5 arcmin |
| Peak sensitivity (5 s source detection) | 1 Crab (1 s) 5 mCrab (50 ks) |
| Absolute flux calibration accuracy | 20 % |
| Relative flux calibration precision | 5 % |
| Sensitivity variation knowledge | 10 % |
| Duration for rate triggers | 0.01 - 100 s |
| Field of view | 3.1 sr (around all pointing instruments) |
| Energy range | 2 - 50 keV primary |
| Energy resolution | 500 eV |
| Energy scale calibration accuracy | 4 % |
| Number of energy bands for compressed images | 8 |
| Time resolution | 300 sec for images 10 µsec for event data |
| Absolute time calibration accuracy | 2 µsec |
| Rate meter data | 16 ms |
| Event/image data downlink maximum delay | 3 hours |
| Onboard storage of triggered data | 3 hours |
| Broadcast of trigger time and position to end user | 30 sec for 65% of the events after onboard detection |
| Number of triggers for WFM | 5 alerts per day |
| Modularity | No full loss of FoV due to single point failure |
| Onboard memory | 5 min @ 100 Crab |

coded mask instruments as shown in Figure 2.10.

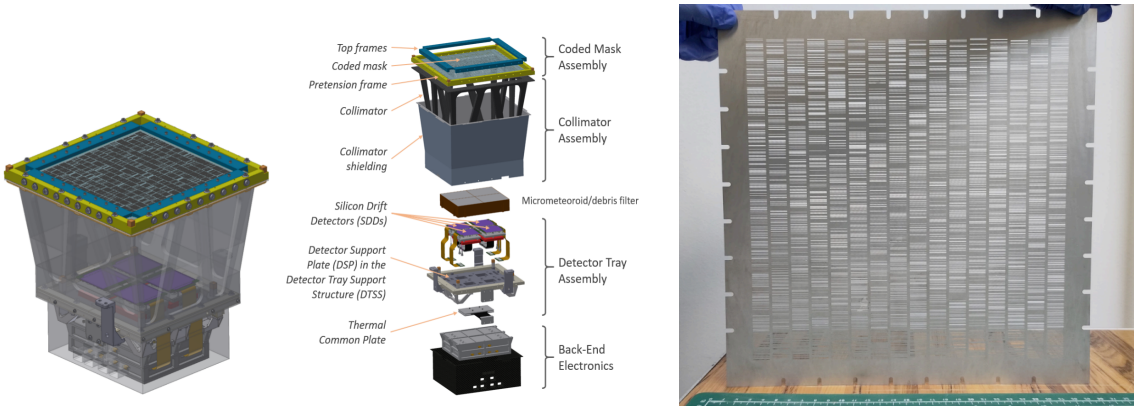


Figure 2.10: The WFM Camera, exploded view of the WFM camera and Coded Mask Design. Left: The WFM camera features a detector plane comprising four detector assemblies (shown in blue), with the coded mask mounted on top. The design supports both fine and coarse resolution directions. The collimator structure and the back-end electronics box located beneath the detector plane are also shown. Right: The Full size coded mask with final pattern is made of tungsten (W) with a slit pitch of 0.25 mm × 16.4 mm. The coding area measures 260 mm × 260 mm with a thickness of 0.15 mm. It contains 16 rows of evenly distributed slits, spaced 2.4 mm apart. Grooves along the edges are included for assembly. (Source: Hernanz et al. (2024))

The WFM consists of three Camera Pairs (six cameras in total, including their Back-End Electronics) and two Instrument Control Units configured in cold redundancy. Each camera comprises the following components: a Detector Tray housing four Silicon Drift Detectors, four Front-End Electronics units, four Be windows, a Back-End Electronics assembly, a Collimator, a Coded Mask, and a Thermal Foil. The Camera Pairs and individual cameras within the WFM are strategically organized to ensure a high level of redundancy. The functional block diagram for the WFM is shown in Figure 2.11. The mask nominal open fraction is chosen to be 25% in the sense that 25% of the 1040 x 16 mask elements are open. The mask pattern is currently derived from the biquadratic residues of the prime number 16901. This pattern exhibits ideal coding properties when used with a perfect detector.

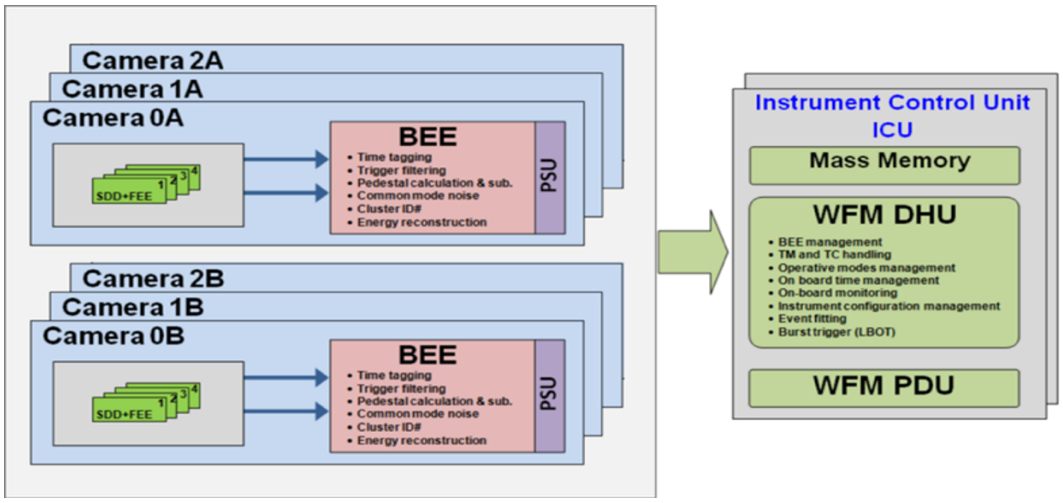


Figure 2.11: Functional Block Diagram of the WFM.

# 3 LAD Hardware Design

As mentioned in the preceding Section 2.2 , the LAD instrument has been excluded from the updated configuration of the eXTP following its most recent design. Nevertheless, the foundational research on the LAD's capabilities, especially its pioneering contributions to high-throughput X-ray spectral-timing instrumentation, continues to hold significant scientific relevance. The instrument's design and performance continue to inform development efforts for next-generation X-ray mission such as STROBE-X (as mentioned in Section 1.2) and ARCO. ARCO (Astrophysics of Relativistic Compact Objects) is a new proposal for ESA' s F3 mission call, and it is expected to be formally proposed soon.

## 3.1 Instrument Overview

The LAD is designed to measure X-ray spectra and photon arrival times from bright Galactic and extragalactic sources. As the name implies, the LAD uses innovative technology and design to achieve an effective detection area of 3.4 square meters. As the largest X-ray detector currently under development, the LAD has an effective area six times that of the PCA (Proportional Counter Array) on the RXTE satellite and the LAXPC (Large Area X-ray Proportional Counter) on ASTROSAT. The LAD combines large-area detection with the high spectral resolution of solid-state detectors, achieving a FWHM energy resolution of 200 eV at 6 keV. This design opens a new observational window for high-throughput spectral-timing studies of bright sources.

The LAD instrument adopts a hierarchical and modular design. The entire LAD is divided into four groups, arranged around the SFA and PFA in a specific geometric configuration. Each LAD module consists of a 4×4 SDD array paired with a 4×4 capillary plate collimator, mounted in a grid-like frame. Each module contains two MBEE PCBs and two Module Power Supply Units (MPSUs). The MBEE collects data from the 16 FEE boards within the module and preprocesses the acquired digital data. To meet the effective area requirements of the eXTP LAD, at least 40 modules are required. For efficient data management, each PBEE controls a group of 10

modules, which together contain 20 Module Back-End Electronics (MBEEs) (two per module). In the hierarchical architecture, the PBEE resides at a higher control level. It aggregates scientific telemetry and housekeeping data from the MBEEs and transmits them to the ICU via redundant SpaceWire links. In addition, the PBEE is responsible for distributing power, telecontrol commands and synchronization clock signals from the ICU to each MBEE unit. Figure 3.1 illustrates the architecture of the LAD instrument.

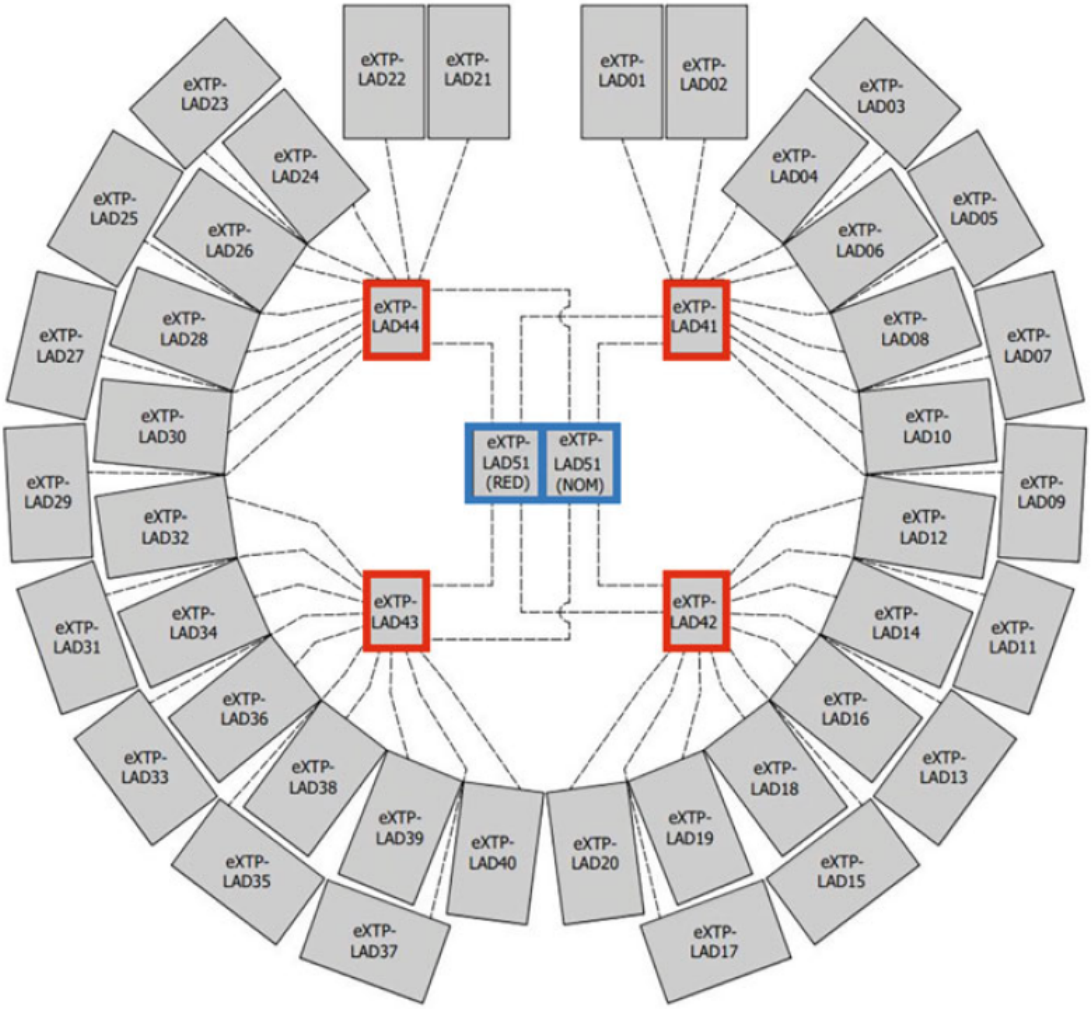


Figure 3.1: The LAD instrument architecture consists of three primary subsystems, as visually represented in the block diagram: 40 gray boxes correspond to the LAD Modules, 4 red boxes denote the PBEEs, and 2 blue boxes signify the Instrument Control Units (ICUs).
(Source: Feroci et al. (2022))

The instrument reduces dead time and pile-up effects through its modular design and collimated field of view. This design enables high-precision spectral-timing measurements when observing bright galactic sources such as X-ray binaries and active galactic nuclei, making the LAD a powerful X-ray instrument. Table 3.1 summarizes

the LAD's key technical parameters. The LAD's capabilities are complemented by the lower-energy sensitivity of the co-aligned PFA and the imaging capabilities of the WFM. This synergistic design integrates the LAD with the other instruments into a versatile observatory, providing advanced capabilities for future astrophysics research, particularly in high-throughput timing and spectroscopy.

This chapter presents the design concept of the LAD instrument and explores the key technologies underpinning its architecture. As a core payload of the next-generation X-ray observatory, the LAD represents a performance leap enabled by several technological breakthroughs: the modular configuration of large-area detectors enhances detection efficiency; precision-optimized collimators provide a 1° FWHM field of view; and solid-state detectors deliver optimized energy resolution. These advances enable the LAD to conduct spectral-timing observations with unprecedented sensitivity, making it a highly capable instrument. The following sections begin at the detector level and analyze the design and integration of each LAD component step by step.

Table 3.1: The main specifications of the LAD instrument (Feroci et al., 2022)

| **Parameter** | **Specification** |
|---|---|
| Energy range | 2-30 keV (extended: 30-80 keV for out-FoV) |
| Effective area | 3.4 $m^2$ @ 8 keV, 0.9 $m^2$ @ 2 keV, 0.3 $m^2$ @ 30 keV |
| Energy resolution | $<$ 240 eV FWHM @ 6 keV (all events) |
| Field of View | 1° (FWHM) |
| Field of Regard | $>$ 50% |
| Absolute Time Accuracy | $<$ 10 $\mu$s |
| Dead time | $<$ 1% @ 1 Crab |
| Background | $<$ 10 mCrab |
| Background knowledge | $<$ 0.5% at 5-10 keV |
| Response stability | $<$ 0.01 Hz: $<$ 2% per decade |
| | 0.01-1 Hz: $<$ 0.2% per decade |
| | 1-1200 Hz: $<$ 0.02% per octave |
| | $>$ 2000 Hz: lower is better |
| | 10-2000 Hz: $<$ 0.0002% nearly periodic |
| Maximum flux | $>$ 500 mCrab (sustained) |
| | $>$ 15 Crab (continuous, 300 minutes) |

## 3.2 Instrument Design

The LAD system integrates a total of 640 detectors. Its modular and hierarchical design ensures that even if a single detector or module fails, the scientific objectives of the mission can still be effectively achieved - each functional unit has the ability to operate

independently. The module contains MBEE PCBs and two MPSUs. The MBEEs is responsible for collecting data from the 16 FEEs in the module and pre-processing the digitized signals.

Although SDD, FEE, MBEE and PBEE are not designed with hardware redundancy, the system limits the impact of single-point failure to the local level through a fault isolation mechanism. Furthermore, the ICU adopts a cold redundancy design, which can seamlessly switch to the backup unit when the main ICU fails, thereby improving the overall system reliability.

### 3.2.1 LAD Modules

#### The Silicon Drift Detectors

The LAD X-ray detectors are large-area SDDs developed by the INFN, the FBK, the INAF, and the Italian Space Agency (ASI). These monolithic SDDs were originally designed for the ALICE internal track system at the Large Hadron Collider (LHC) at CERN (Rashevsky et al., 2001, 2002) and were later optimized for the eXTP mission. They have a sensitive area of 10.86 cm × 7.00 cm, geometric dimensions of 120.8 mm × 72.5 mm, and a silicon wafer thickness of 450 $\mu$m (Rachevski et al., 2014). A single silicon wafer is divided into two symmetrical halves, each half integrates 292 drift cathodes with a cathode spacing of 120 $\mu$m (Rachevski et al., 2023). Two columns of 224 readout anodes are set in the edge area of each half, with an anode spacing of 970 $\mu$m.

The detector works in conjunction with a lead glass collimator (capillary plate) manufactured based on MCP technology, which can accurately limit the FoV of the LAD to 1° (FWHM) (Zhao et al., 2024). Its nominal energy coverage range is 2-30 keV, and can be extended to 80 keV (FoV out-of-detection mode) for bright source observations.

These detectors show highly competitive performance indicators: a FWHM energy resolution of 300-500 eV at 6 keV energy and a time resolution of 10 $\mu$s, providing excellent detection capabilities for X-ray astrophysics research. These performance indicators make it an ideal observation platform for studying the spectral timing physical processes in compact objects (such as NSs and BHs) and high-energy transient sources (such as gamma-ray bursts).

Figure 3.2 shows the full-scale prototype of the SDD developed by FBK. The prototype has been radiation hardened and calibrated by the joint team of INFN and INAF.

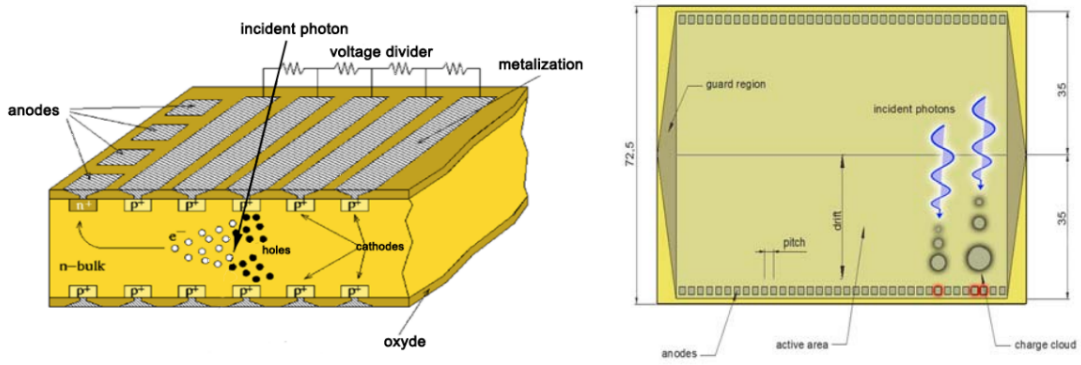


Figure 3.2: Working principle of large area Silicon drift detectors: The left figure illustrates the physical process by which photons are absorbed in the silicon material substrate, while the right figure presents the structural features of the detector module. The module is configured with an array of annular signal reading anodes in the top and bottom regions. With the directional migration of carriers under the action of electric field, the spatial distribution of the charge cloud exhibits a diffusion characteristic with respect to the length of the drift path, and by resolving the spatial distribution parameter of this diffusion characteristic, the spatial coordinates of the particle incidence event in the drift direction can be accurately reconstructed.
(Source: Brandt et al. (2012))

The working principle of the SDD is shown in the right of Figure 3.2. When an X-ray photon is incident on the SDD, an electron cloud is generated by the photoelectric effect. The electron cloud then drifts toward the readout anode located at the edge of the detector under the action of a graded electric field, which is established by a graded negative bias (up to -1.3 kV) applied through the cathode array arranged on both sides of the detector. The maximum drift length is 35 mm, with the constant drift field strength being 360 V/cm, resulting in an electron drift velocity of approximately 5 mm/$\mu$s and a maximum drift time of 7 $\mu$s.

During the drift process, the inherent diffusion effect of the silicon material causes the electron cloud to expand, and its diffusion radius is positively correlated with the square root of the drift time, making the spatial distribution of the charge cloud linearly dependent on the drift distance. Consequently, If the total charge is completely collected by a single anode, it is defined as a single anode event; when the charge is shared by two adjacent anodes, it is classified as a double anode event.

Several pre-series production batches of detectors were delivered, and the overall qualification procedure was successfully carried out on some of these detectors (Campana et al., 2014; Rachevski et al., 2023).

### The Front-end Electronics

Figure 3.3 shows the LAD FEE electronic architecture. The LAD Detector Assembly (DA) is composed of the SDD detector and its FEE board. The LAD FEE, developed by the University of Geneva, is responsible for readout and analog-to-digital conversion of the charge signals from the SDD anodes and communicates with the MBEE. The FEE is divided into 2 symmetrical rows of 14 ASICs. To match the pitch of the SDD anodes and maintain a compact layout, only 8 out of the 32 available channels per ASIC are used. Each ASIC of the row has differential trigger lines connected in parallel to the MBEE, allowing triggers to propagate in parallel. Each ASIC also has an individual hardwired address, allowing individual access via common CMD and clock (CLK) differential signals, where the individual ASIC address (0 to 13) or broadcast (14, i.e. all ASICs) can be set within the command frame.

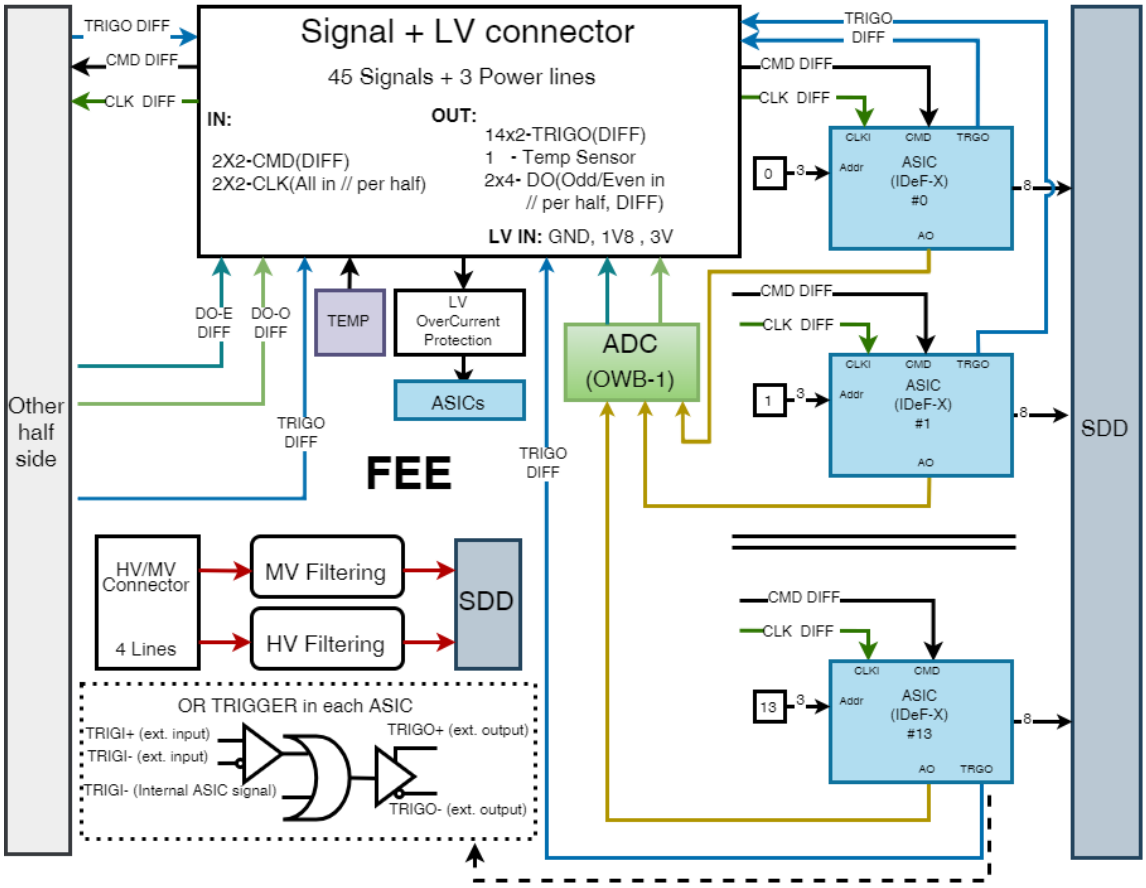


Figure 3.3: LAD FEE Electronic architecture.

The FEE is based on the the IDeF-X ASIC(Baudin et al., 2022) , a 32-channel front-end ASIC optimized for low capacitance and leakage current. It was developed by the French Alternative Energies and Atomic Energy Commission (CAE). Each anode channel is converted by a charge-sensitive amplifier with a charge-to-voltage conversion

sensitivity of 20 mV/fC, followed by a programmable gain-adjustment module covering a range of 50 to 200 mV/fC. The ASIC integrates a peak-widening unit and signal-holding circuitry to ensure a stable output over the controller read cycle by capturing the pulse peaks in real time and maintaining their voltage amplitude. The output of this analogue signal exhibits a linear proportionality to the anode charge, and the analogue-to-digital conversion is completed by the OWB-1 dedicated integrated circuit (Bouyjou et al., 2017). The chip adopts a 13-bit high-precision conversion architecture with a fast conversion capability of 2.8 $\mu$s to quantify the analogue voltage signal output from the sensor in real time.

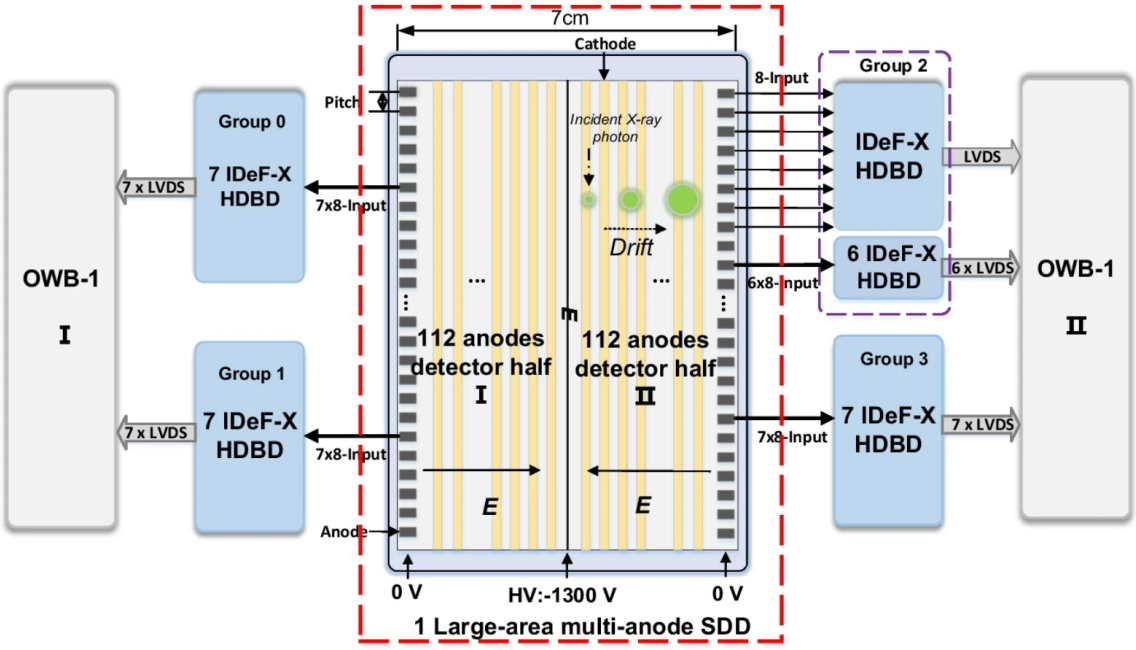


Figure 3.4: The detector employs a segmented large-area SDD with multiple anodes, partitioned into two symmetrical halves. Each half utilizes two clusters of 14 IDeF-X HDBD readout circuits to handle signals from 112 anode channels, with both clusters interfacing through a common OWB-1 ADC. A HV supply of -1.3 kV is centrally biased along the detector's symmetry plane, establishing an inward radial electric field gradient from the detector periphery toward the central axis. (Source: Xiong et al. (2025))

As a result, the FEE consists of two symmetrical rows, each containing 14 ASICs as shown in Figure 3.4. The demo board is shown in the Figure 3.5, and it is worth noting that the demo board is only designed for functional verification with only 7 ASICs in each row. The SDD tile is glued to the backside of the FEE board, which is based on rigid-flex technology, with short wire bonding connections to minimize capacitance. The anodes of the SDD are directly connected to the input channels of the ASICs.

Each LAD SDD has an associated FEE board onto which it is mounted; the FEE board is glued directly to the SDD, additionally providing mechanical support to the

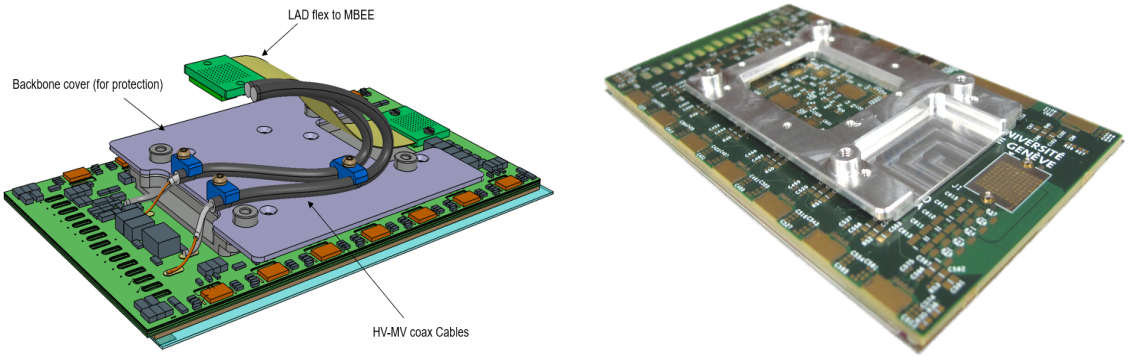


Figure 3.5: The design of the FEE DM. *Left*) Three-dimensional design of the FEE. *Right*) The FEE DM board, designed by the University of Geneva, features only 7 ASICs, serving as a demonstrator. (Source: Yannick Favre)

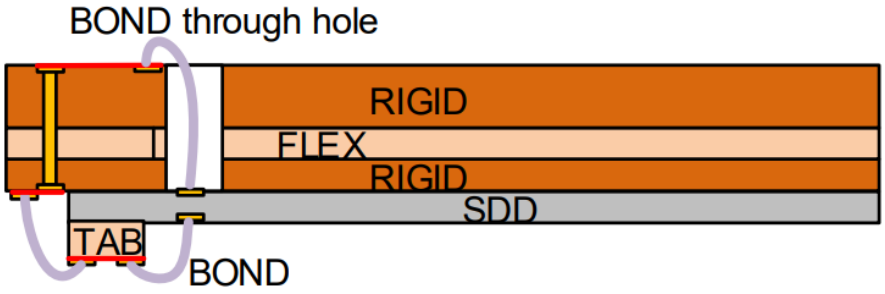


Figure 3.6: LAD FEE SDD bonding principle

SDD. The bottom cathodes of the SDDs are first bonded to an intermediate flexible tab, which is then glued to the bottom of the PCB. Subsequently, the end of the tab is bonded to the PCB, implementing a double-bond mechanism to minimize wire length. The top cathodes, located under the PCB, require drilled holes in the board to allow for bonding, as shown in Figure 3.6.

### The Collimators

Each LAD detector is paired with a collimator of equal area to limits background contamination from off-axis discrete sources and the diffuse Cosmic X-ray Background (CXB). The LAD's FoV is limited by the lead-glass collimators fabricated through MCP technology. These collimators comprise densely packed cylindrical micropores with a diameter of 83 $\mu$m and length of 5 mm, achieving an open area ratio exceeding 70%. The LAD collimator design inherits and extends the technological legacy of pioneering X-ray detectors, including the Medium Energy Detector Array (MEDA) and Gas Scintillation Proportional Counter (GSPC) aboard the EXOSAT observatory, while incorporating advancements from the Mercury Imaging X-ray Spectrometer (MIXS) developed for the BepiColombo mission. Significantly, the collimator architecture of the MIXS-C (Collimated detector) subsystem, characterized by its high-aspect-ratio microchannel geometry and efficient background rejection capabilities, has provided a critical design paradigm for optimizing the LAD's collimation efficiency. Figure 3.7 displays an optical micrograph of a representative micropore plate.

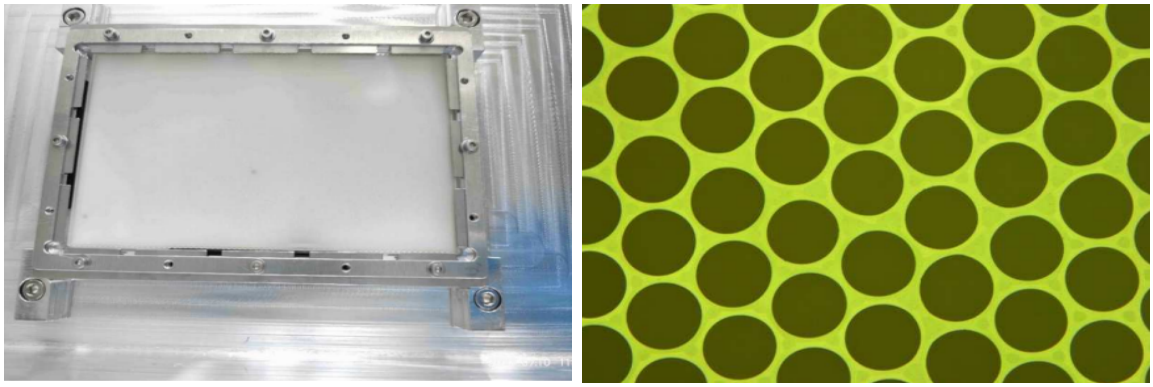

Figure 3.7: Diagrammatic representation of the MCP structure. (a) The device solid on the assembly jig, showing that the assembly is made of a rectangular thin lead glass substrate with a form factor of (111.0 ± 0.1) × (72.5 ± 0.1) mm$^2$, and the substrate thickness accuracy is controlled in the range of 5.0 ± 0.1 mm Lombardi et al. (2022). (b) Microscopic image of micro-region morphology and structural features revealing the geometrical properties of microscopic channel arrays on the device surface. (Source: Zhao et al. (2024))

The core scientific requirements driving the design of LAD collimators include the

following three key dimensions:

- **Field-of-View**: accurate spatial positioning of the target source is achieved through 1° FWHM angular resolution, while suppressing background noise caused by all source X-rays incident at larger angles;
- **High-energy transparency optimization**: maintaining excellent photon transport efficiency in the 30-50 keV energy region, which requires the coordinated design of the micropore aspect ratio and X-ray attenuation characteristics of the collimator material (lead glass);
- **Response function engineering**: a flat-top structure needs to be introduced into the basic triangular response function to accurately characterize the dependence of X-ray transmittance on the off-axis angle. This non-ideal response correction is of great value in studying the energy spectrum decomposition of extended sources (such as supernova remnants) and diffuse backgrounds.

The details of the baseline design are given in Table 3.2.

Table 3.2: MCP specification

| **Parameters** | **Value** |
|---|---|
| Pore diameter [$\mu$m] | $83 \pm 5$ |
| Chanel aspect ratio | $60:1$ |
| Pb fraction [%] | 37 |
| Thickness [mm] | $5 \pm 0.1$ |
| Open area ratio [%] | $\geq 70$ |
| Surface parallelism [arcmin] | $\leq 1$ |
| Dimensions [mm$^2$] | $(111 \pm 0.1) \times (72.5 \pm 0.1)$ |
| Channel roughness [nm] | $\geq 13$ |
| K-fraction [%] | $\leq 0.1$ |

### The Optical Filters

The optical filter of LAD is a key component of the module's optical and thermal design. Since the SDD is sensitive to photons in the optical/ultraviolet band, these photons induce dark current, resulting in a significant increase in readout noise. At the same time, the LAD module adopts a passive cooling design, so the thermal radiation characteristics of the optical filter need to match the overall thermal design of the module to ensure on-orbit thermal stability. In order to ensure the signal-to-noise ratio of the detector, the supporting filters need to meet a dual technical specification: superb attenuation of $>10^8$ orders of magnitude in the optical wavelength band

(200-1100 nm), and high transmittance of >0.85 at the characteristic X-ray energy point of 2.5 keV (approaching the theoretical limit). The filter module also needs to meet space-grade environmental adaptability requirements: it needs to be equipped with a proton-resistant oxygen erosion protection layer during low-orbit operation to cope with the bombardment of reactive oxygen atoms in the low-Earth orbit (LEO) environment of up to 2.3 x $10^{22}$ $atoms/cm^2$ (5-year cumulative flux).

In order to achieve the low-noise environment required for X-ray detection, physical isolation must be used to prevent optical/ultraviolet band photons from reaching the SDD. Specifically, the optical filter achieves this goal by mechanically mounting the filter between the collimator plate and the detector. The optical blocking filter is mainly composed of aluminum film and polyimide film, wherein the thickness of the aluminum layer and the polyimide is determined by the low energy cutoff requirement of the X-ray. In the optical filtering design of LAD, the thickness of polyimide (as a structural support layer) is optimized to 1-2 $\mu$m, and the thickness of the aluminum layer is 200 nm. This configuration achieves transparency to X-rays and a transmission suppression ratio of $10^{-8}$ in the O/UV band, effectively meeting the detector's requirements for low noise and high sensitivity detection. The Figure 3.8 shows a prototype of an optical filter design by INAF.

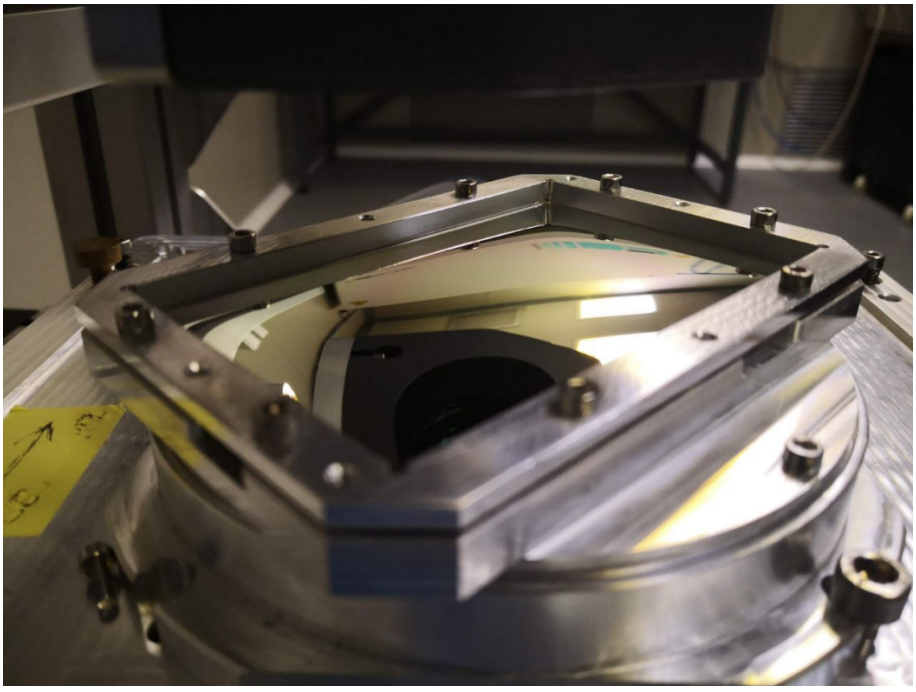

Figure 3.8: The LAD filter mounted in the bulge test holder during a measurement. (Source: Cicero et al. (2022))

### Module Back-end Electronics

Each module contains two MBEEs, each of which manages half of the detector units in the module (16 SDDs and their FEE). The MBEE reconstruction pipeline is designed to process event data streams from 16 SDDs in parallel. The MBEE circuit board integrates the following key components: radiation-hardened field programmable gate array (Radiation-Hardened FPGA), LVDS transceivers, interfaces to other relevant LAD components (FEEs, PBEE, and MPSU), and voltage and current monitor circuits. The core functions of the MBEE include real-time collection of digital event data from 16 FEE units and sending remote control commands to the FEE. Its pipeline design can process data from all 16 detectors simultaneously and keeps the pipeline always ready to process the next event. The digitized events are transmitted to the PBEE after preprocessing, 16-bit timestamp marking and format packaging. In addition, MBEE is also responsible for collecting internal module housekeeping data and forwarding it to PBEE, while managing the power distribution of the FEE unit.

Task of MBEE

The primary role of the MBEE is to handle data received from the FEEs, derive timing information, reconstruct energy, and produce science data packets. Each MBEE board is responsible for collecting data from eight FEEs, covering half of a module. Furthermore, the MBEE oversees the operation and control of the ASICs through the FEE interface, configures the HV and MV for the SDD using the PSU interface, and creates housekeeping data to track the condition of the module's electronics. These tasks are executed by the MBEE in response to telecommands sent from the ICU to the MBEE through the PBEE.

Event Processing

The MBEE pipeline was implemented in VHSIC Hardware Description Language (VHDL) and has been preliminarily verified and operated in an MBEE prototype design at the IAAT. To extract an accurate photon energy from the raw digitized signals, which are contaminated by electronic offsets and noise, the MBEE pipeline performs several real-time processing steps. This section briefly describes the MBEE pipeline that constructs the event packet for a valid event. For a more detailed description, refer to the paper *Preliminary design and development of the module back-end electronics for the large area detector onboard the eXTP mission* (Xiong et al., 2025).

- **Pedestal subtraction**: The process of subtracting a set of pedestal values (one per anode) stored in the MBEE from th measured signal values. These pedestal

values result from manufacturing variations.

- **Common noise (CN) subtraction**:Basically, it is an undesired baseline shift, mainly caused by intrinsic noise and statistical fluctuations. It consists of two effects: the CN generated by the detector and the CN introduced by the ASIC; therefore, only channels not hit by the charge cloud will be considered in the calculation of the CN for each ASIC. The calculation will be performed using the median algorithm.

- **Energy reconstruction**:The procedure will be composed of the following steps:

  - **Gain Correction**: The reconstructed energy of an event is calculated as the sum of signals from n event channels, where each channel is multiplied by an individual gain factor. These factor are stored in a lookup table (shared with the pedestal table) and can be recalculated or uploaded from the ground.

  - **Temperature Correction**: The Gain calibration will be performed at fixed temperature and assumes a gain variation coefficient of 0.1%/°C

  - **Upper Threshold Rejection**: If the reconstructed energy exceeds the upper limit, the event is rejected.

  - **Energy Scaling**: The final step of the energy reconstruction of 9-bit energy word is generated through a nonlinear function defined as:
    2-30 keV: 60 eV per bit;
    30-80 keV: 2 keV per bit.

- **Generate event packet**: Event packets are generated based on distinct observation modes (standard and high-rate observation modes).

The upper section of Figure 3.9 depicts the architecture of the data processing pipeline, while the lower section provides detailed visualization of data packets generated under different observation modes.

### Module Structure

Figure 3.10 shows the breakdown of the LAD module, which consists of the aforementioned components and is the core functional unit of the LAD. The structure of the module consists of two parts: the collimator tray and the detector tray. The main function of the collimator tray is to provide mechanical support for the 16 collimators and optical filters in the module and ensure their coaxial arrangement; the coaxial

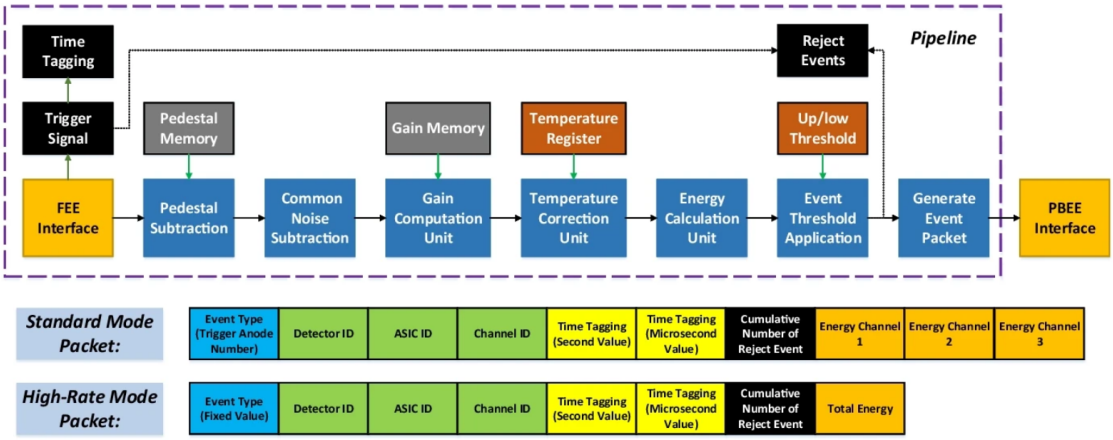


Figure 3.9: Detailed Pipeline Processing Flow and Event Packets in Two Observation Modes. (Source: Xiong et al. (2025))

accuracy can be controlled within 1 arc minute through a clamping mechanism that is specially designed to compensate for the difference in thermal expansion coefficients between the glass micro-aperture collimators and the aluminum alloy tray frame. The detector tray provides mechanical support for 16 sets of SDD/FEE components and related MBEE and MPSU.

The rear of the module is equipped with an aluminum alloy heat sink panel for thermal management, and a 300 micron thick lead shielding layer is installed to reduce the background noise of the detector. The thermal pad is used to transfer the heat generated by the MPSU to the rear heat sink panel. Each LAD module is thermally isolated from the panel support frame. The LAD module itself does not have an active cooling system, but is equipped with heaters to ensure that the temperature does not fall below the minimum operating limit (-55°C); in addition, these heaters can be used to periodically anneal the SDD.

### 3.2.2 The Panel Back-End Electronics

Each LAD group hosts a PBEE that processes all events for the ten modules in the group and provides power and data interface directly to the LAD ICU. Each PBEE has redundant LVDS signal port for communicating commands and telemetry with the ICU as well as transmitting high rate scientific data directly to the ICU.

The primary tasks of the PBEE are to connect to the MBEEs, collect and buffer event packets, reformat time stamps and packet data according to the observation mode, transmit data to the ICU, execute commands from the ICU and distributing them to the MBEEs, and collect and format telemetry internal packets sent to the

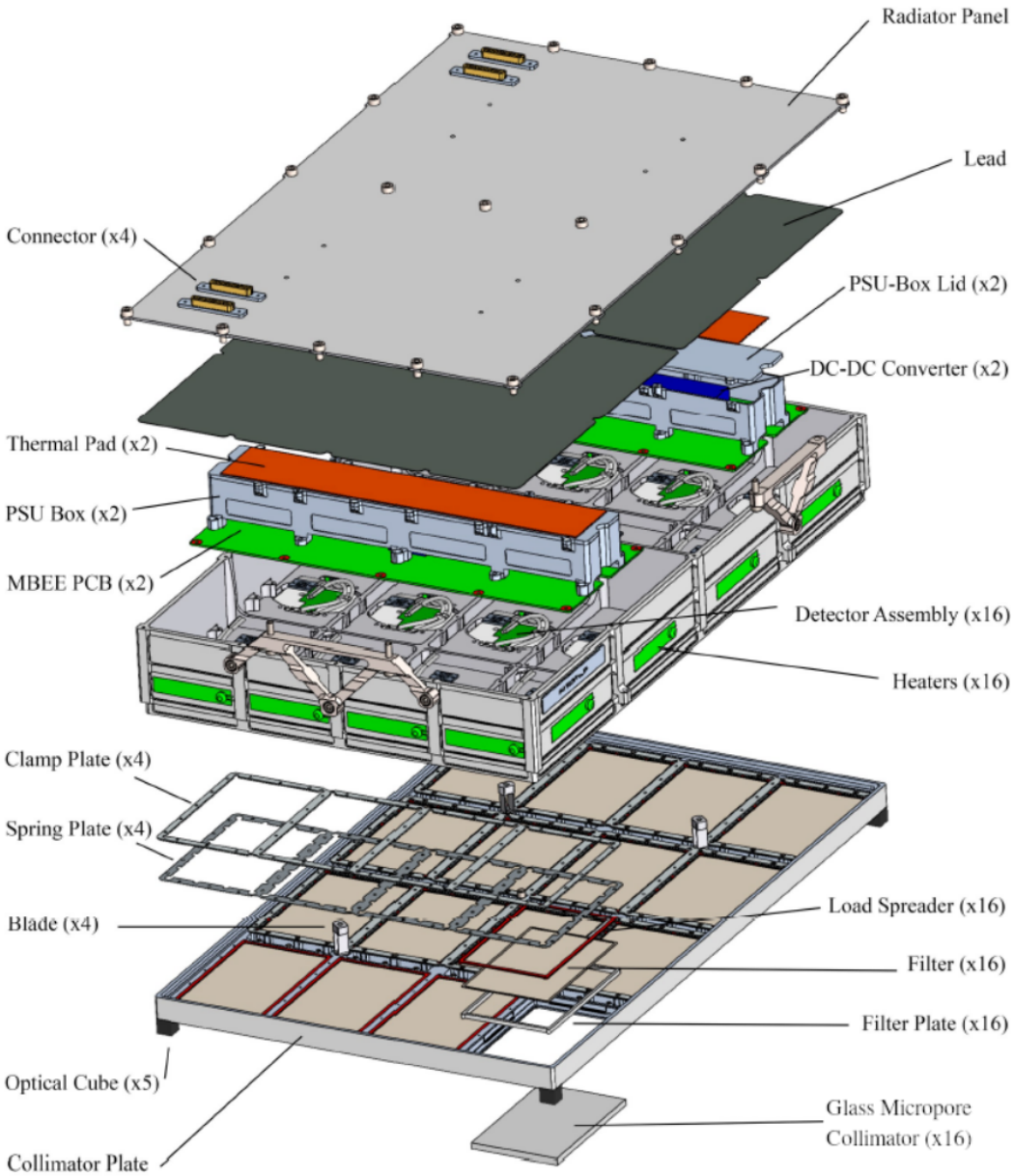


Figure 3.10: Exploded view of the LAD module design. (Source: Santangelo et al. (2023a))

ICU. Additional tasks of the PBEE include distributing a stable 10 MHz High-accuracy Clock (HAC) and PPS to MBEEs. The standard operating mode of the ICU telemetry contains complete information about each event. This includes the event type, differential time tag, and event energy. After an event has been successfully detected and its energy has been reconstructed the event package is sent to the PBEE.

The development and testing of a PBEE prototype board was done as part of this thesis. Therefore the PBEE is presented in much more detail in Chapter 4 - PBEE Prototype design.

### 3.2.3 The Instrument Control Unit

The ICU serves as the central control component for the LAD instrument. It provides the interface to the spacecraft Onboard Data Handling (OBDH) and also control the instrument sub-systems via SpaceWire. The ICU box comprises two integrated modules: the Data Handling Unit (DHU) and the Power Distribution Unit (PDU). The prototype of the ICU is shown in the Figure 3.11 .


Figure 3.11: Prototype of the LAD' s Instrument Control Unit (ICU), developed by the University of Tübingen, based on a LEON4 – GR740 Evaluation Board.

The ICU system is duplicated in a redundant configuration (cold standby) to ensure operational continuity. Its core functionality resides in the Data Handling Unit, which is responsible for compiling, processing, and compressing scientific data, as well as HK collection, instrument health monitoring, and calibration tasks. The LEON4 microprocessor was selected to execute embedded software operations, offering superior

configurable capabilities over rigid hardware-based architectures such as state-machine implementations.

The DHU collects the data from the PBEEs via a SpaceWire interface PCB, as shown in Figure 3.12, performs the selection and formatting tasks depending on the selected observation mode. Besides the routing and execution of telecommands, the ICU can run macro commands for several tasks, including on-board calibration and the individual sequenced switching of the MBEEs in the engineering modes.

### 3.2.4 Power Distribution

Power will be distributed in the form of 43 Volts from the S/C PDU via the DHU and the PBEEs to the individual MBEE, as shown in Figure 3.12. All necessary lower voltages are generated at the respective level (DHU, PBEE, MBEE) by local power converter boards. This configuration reduces cabling between the ICU, the PBEEs, and the MBEEs. Additionally, the high-voltage requirements for detector operation are locally supplied through specialized high-voltage circuit boards integrated directly into each module.

In particular, the PBEE Power Supply Unit (PPSU) is in charge of main power supply elaboration, providing the internal LV supplies for the PBEE prototype (3.3 V, 1.8 V, plus 1.25 V generated on board by shunt resistor), as well as to generate the secondary voltage supply for each of the 10 LAD Modules. PPSU shall switch the secondary power supply towards the MBEE on/off by a PBEE TC and give back the related status telemetry.

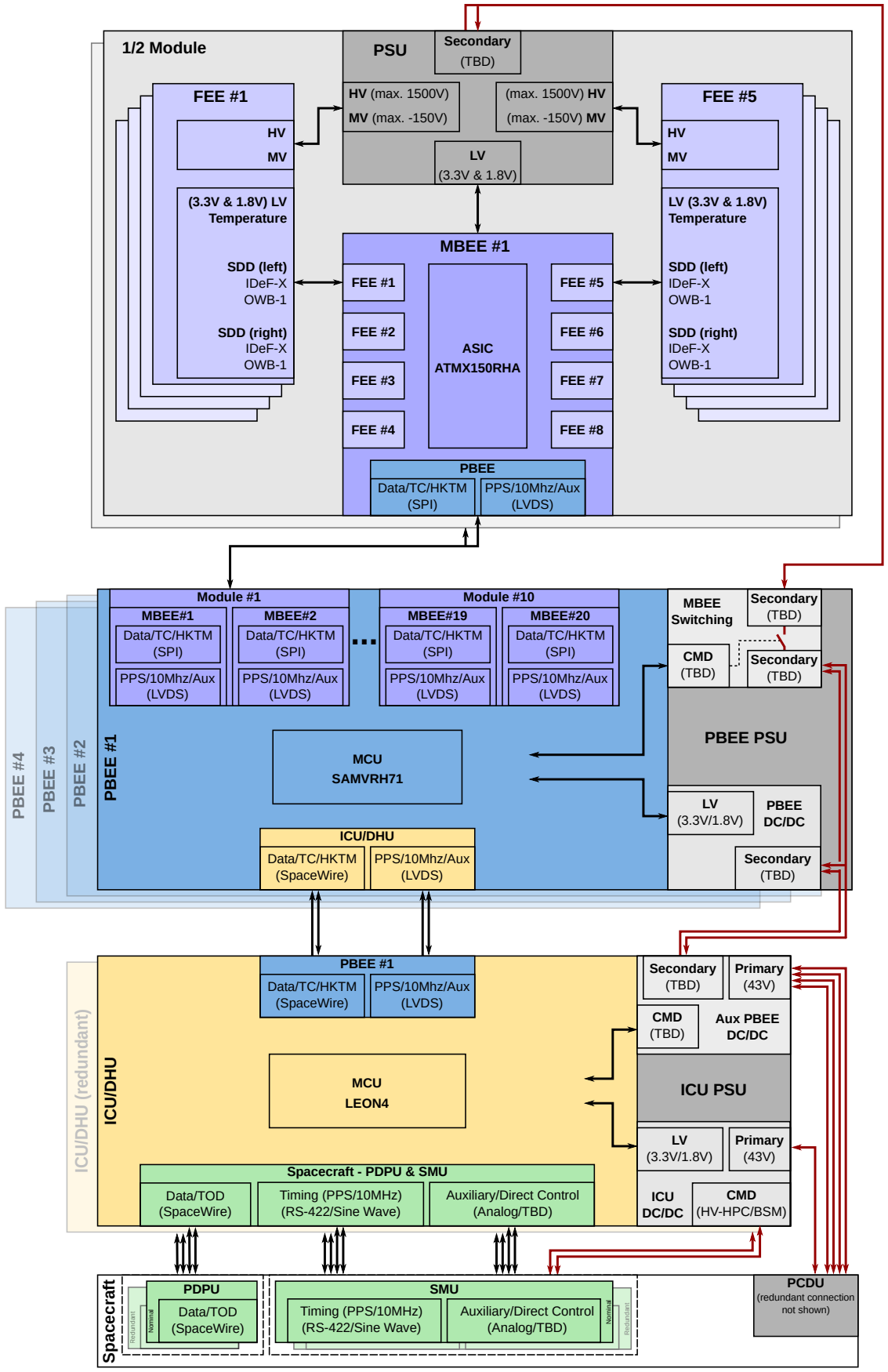


Figure 3.12: Electrical configuration of the LAD. The block diagram illustrates the interfaces between hierarchical electronic circuits and the allocation of electrical power of the LAD. (Source: Jörg Bayer)

# 4 PBEE Hardware Prototype

As described in Chapter 3, the back-end electronics of the LAD are designed with two hierarchical levels: MBEE and PBEE. These units read out the scientific data after the charge cloud generated in the SDD is converted and digitized by the FEE. Simultaneously, the FEE requires real-time configuration and control. Additionally, the MBEE processing pipeline performs event reconstruction, time-stamping, and format packaging on the raw scientific data to generate standard telemetry packets. Since the LAD system contains 40 detector modules (corresponding to 80 MBEEs), the MBEE cannot directly establish a point-to-point connection with the ICU due to the limitations of interface resources and transmission bandwidth. To manage the large number of LAD modules, the PBEE is therefore designed to serve as a router between the ICU and the MBEEs.

This chapter presents the development of the PBEE. The electronics development encompassed the digital circuitry design for the PBEE and the development of firmware in C for its Microcontroller Unit (MCU). This firmware controls the functional blocks that manage communication with both the ICU and the MBEEs. The functional blocks of this electronic system are developed based on the FreeRTOS (Richard, 2025)* real-time operating system running on the MCU in order to realise the real-time response of the PBEE to ICU commands and the efficient processing of MBEE scientific data packets. Additional work presented in this thesis includes electronic prototyping, manufacturing, iterative improvements, development of control and analysis software, component-level testing, and validation of the complete readout chain functionality.

This chapter first describes the functional definition and task requirements of PBEE, followed by a detailed analysis of the implemented PBEE circuit architecture and its core components. It then presents the hierarchical architecture and key functional modules of the MCU firmware design. Finally, it describes the mechanical design of the PBEE accommodation box. A verification of the PBEE electronics' function is described in Chapter 5.

*FreeRTOS is a real-time operating system (RTOS) kernel designed for embedded systems. Originally developed by Richard Barry in 2003, it has been successfully ported to a wide range of microcontroller architectures.

## 4.1 Functional Description

The PBEE handles all event data from a group of 10 LAD modules as shown in Figure 4.1. It primarily functions as a data and command router between the ICU (specifically the Data Handling Unit, DHU) and the MBEEs. The PBEE is responsible for implementing command distribution, data acquisition, and data processing functionalities. Specifically, it acquires scientific data from the MBEEs, transfers processed data to the ICU via SpaceWire, manages the Telemetry/Telecommand (TM/TC) interface, and distributes the HAC and PPS signals to the MBEEs.

The primary tasks of the PBEE include:

- Interfacing with up to 20 MBEEs
- Collecting and buffering event packets
- Distributing the clock signal
- Reformatting data based on the observation mode
- Transferring data to the DHU
- Collecting housekeeping (HK) data and generating HK packets

The interface between PBEE and DHU is a fully compliant SpaceWire interface, running at 100 MHz

## 4.2 Hardware

The development of a data processing device begins with the selection of the core processing hardware. This selection requires a systematic evaluation of competing factors, including cost, computational performance, architectural complexity, physical size, and power efficiency. Candidate technologies, such as FPGAs, ASICs, and MCUs, exhibit significant differences in processing throughput, design complexity, and cost. A critical secondary consideration involves determining the optimal programming paradigm commensurate with operational requirements. For example, microcontroller-based designs are typically programmed in C, whereas FPGA architectures are configured using Hardware Description Languages (HDLs). This section will discuss the different hardware options, while software implementation specifics will be analyzed in subsequent discussions.

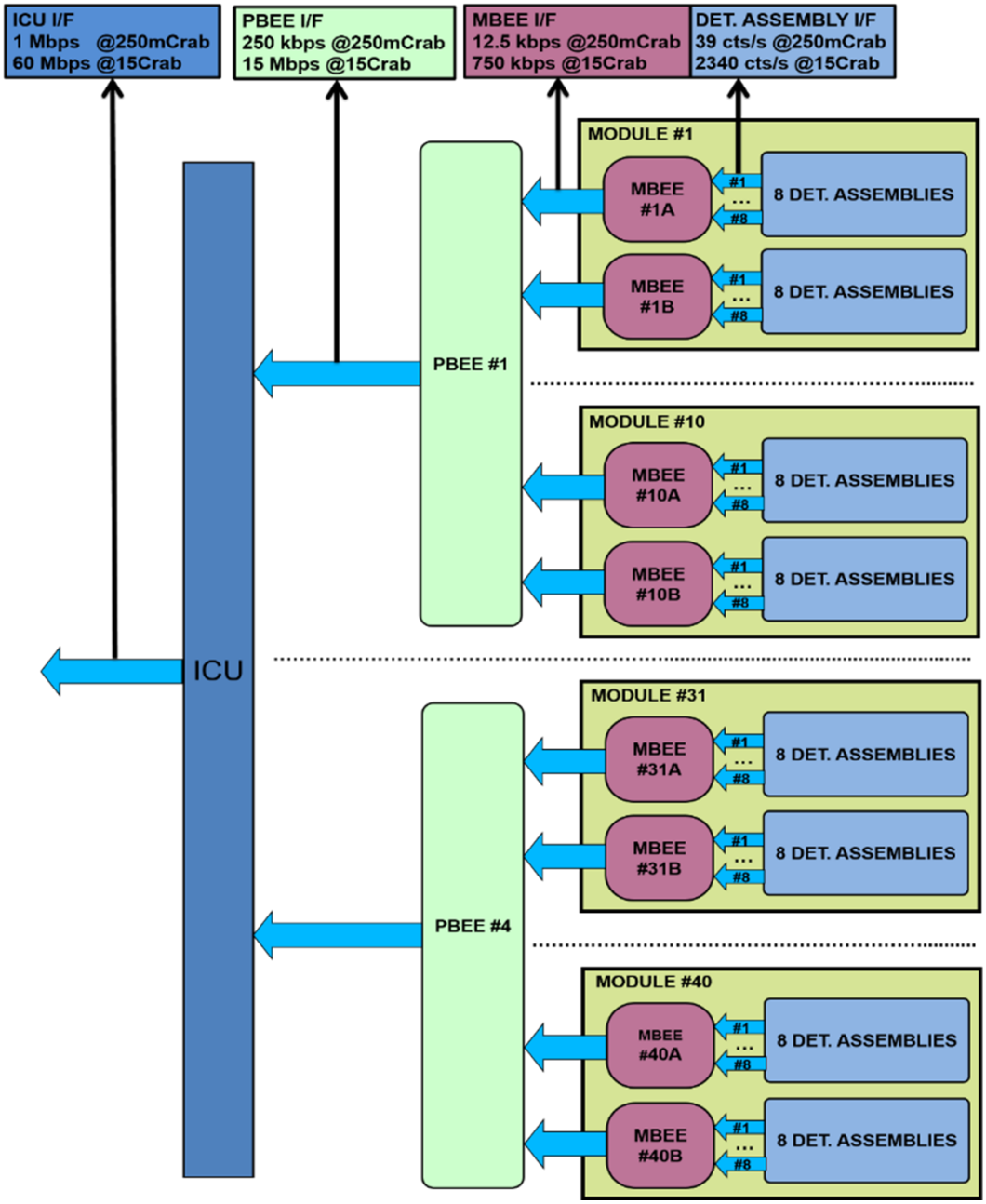


Figure 4.1: Each LAD module contains 16 SDD assemblies, which are read out by two MBEE boards. Consequently, each MBEE board processes data from 8 SDDs or 16 SDD halves. Since the MBEE reads each detector half in parallel, 16 parallel data pre-processing pipelines are implemented in each MBEE. The four PBEEs are responsible for collecting the scientific data and forwarding it to the ICU. The expected data rates at each hierarchical level are provided at the top. (Source: eXTP-EKUT-LAD-RP-0002 LAD PBEE Design Report.)

### 4.2.1 Field-Programmable-Gate-Array

An Field-Programmable Gate Array (FPGA), classified as a re-programmed integrated circuit (IC), is built on a silicon chip. This architecture consists of an array of field-programmable logic blocks connected via programmable routing matrices, allowing in-system hardware reconfiguration through post-fabrication programming. FPGAs offer very dynamic circuit reconfigurability, enabling architectural modifications via bitstream programming to support a wide range of functionalities. Since it can process a large amount of data in parallel, it is mainly used in application scenarios with large data throughput. As a result, parallel execution of statements has become one of its defining features. It is mainly configured using hardware description language (HDL) to achieve arbitrary functions. The MBEE described in previous chapters was developed using FPGA technology. Notably, during the LOFT era, FPGAs were also widely employed in the development of similar instruments, such as the LOFT LAD (Xiong et al., 2025; Zane et al., 2012).

### 4.2.2 Application-Specific Integrated Circuits

ASICs are integrated circuits (ICs) designed for specific functions or applications. Unlike FPGAs, which can be reprogrammed after fabrication, ASICs are custom-built for specific tasks and remain fixed once manufactured. Although both share similar manufacturing processes, ASICs are tailored for dedicated applications, whereas FPGAs offer post-fabrication flexibility. Customization is an expensive process but allows them to meet requirements that would not normally be feasible with generic hardware solutions.

### 4.2.3 Microcontroller

Microcontroller units (MCUs) have been used aboard space missions due to their low-power operation, high integration density, and deterministic real-time control capabilities. These monolithic integrated circuits incorporate essential computing components including central processing units (CPUs), memory architectures (RAM/ROM), programmable I/O interfaces, and mission-critical peripherals (e.g., timers, analog-to-digital converters (ADCs), universal asynchronous receiver-transmitters (UARTs)), consolidating computational and control functionalities within a single die to execute autonomous operations. Specifically for extraterrestrial deployments, space-grade MCUs implement radiation-hardened design methodologies employing techniques such as triple modular redundancy (TMR) and silicon-on-insulator (SOI) fabrication to

mitigate single-event effects (SEEs) caused by galactic cosmic rays (GCRs) and solar particle events (SPEs). Since electronic components or circuits are often affected by ionizing radiation in the space environment, radiation hardening becomes an important condition for the selection of space instrument components. This kind of MCU with radiation-resistant process is called radiation-hardened MCU, which are designed to mitigate the effects of SEEs, such as single-event latch-up (SEL), single-event transient (SET), single-event upset (SEU) or single-event burnout (SEB).

### 4.2.4 SAMRH71

The PBEE is responsible for communicating with the 20 MBEEs during the mission. Since its primary tasks—command routing, data packet handling, and interface management—are control and communication-intensive, a microcontroller (MCU) is more suitable than an FPGA-based architecture. This is because MCUs excel at running complex protocol stacks and real-time operating systems, which matches the PBEE's needs. Moreover, compared to FPGAs, MCUs do not require developing complex finite state machines (FSMs) and offer extensive protocol libraries, greatly reducing development cycle and complexity. Additionally, due to U.S. export control restrictions, the design must utilize non-U.S. technology. Therefore, for these technical and regulatory reasons, the SAMRH71 MCU (Figure 4.2) was selected.

Radiation Hardened SAMRH71 [1] is a 32-bit Arm® Cortex®-M7 (with FPU) microcontroller manufactured in the ATMX150RHA process, which provides high radiation tolerance and latch-up immunity. This high-performance MCU operates at up to 100 MHz and integrates 128 KB of flash, 16 KB of double-buffered memory, over 1 MB of embedded SRAM, and external memory interfaces. Figure 4.3 represents the block diagram of the SAMRH71 microcontroller.

[1] https://www.microchip.com/en-us/product/samrh71

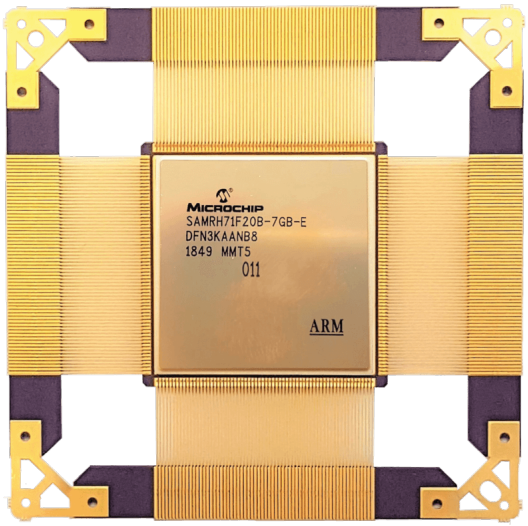


Figure 4.2: The microcontroller SAMRH71. The pin requires the use of a specialized pin bending device to achieve the precise curvature needed for compatibility with the PCB package.
(Source: Microchip Technology)

**Key Features** [2]

- Manufactured with ATMX150RHA technology
- Arm Cortex-M7 Core running up to 100 MHz delivering 2.14 DMIPS/MHz
  - Simple- and double-precision HW Floating Point Unit (FPU)
  - Embedded Trace Module (ETM) with instruction trace stream, including Trace Port Interface Unit (TPIU)
  - One dual-port 32-channel central DMA Controller (XDMAC)
  - One PLL for system clock, one PLL for peripherals
  - SEU full characterization LET >20Mev
  - Total Ionizing Dose of 100 krad(Si)
  - Temperature range – 55°C to +125°C
- Memory
  - 128 Kbytes embedded Flash with build-in ECC (up to 2 errors correction)

[2] https://www.microchip.com/en-us/product/samrh71#Overview.

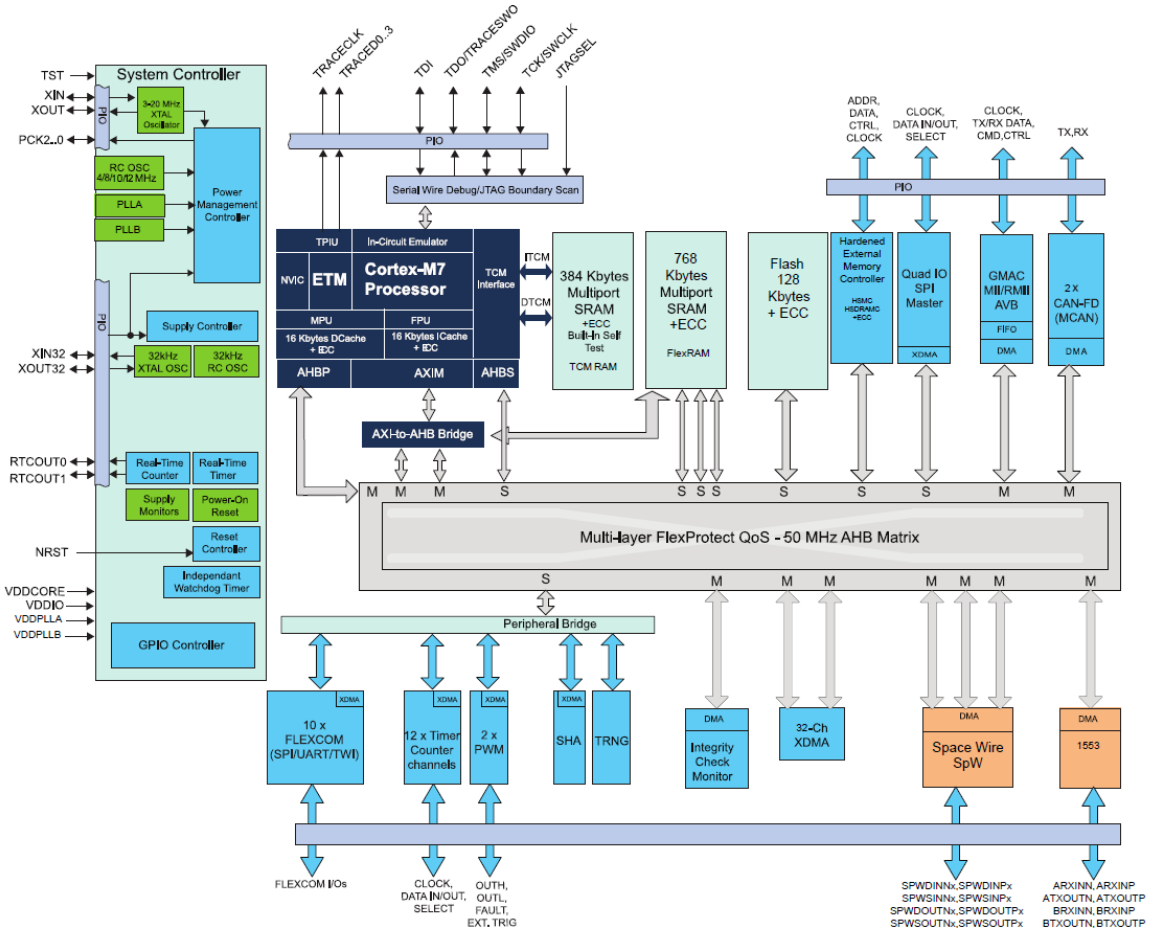


Figure 4.3: The SAMRH71 Block Diagram. The SAMRH71 is ideally suited for aerospace applications, as it integrates various aerospace reception/transmission links with vehicle data, such as SpaceWire and 1553. The device's peripheral set includes Ethernet 10/100, two CAN-FDs, up to 10 FLEXCOMs (USART/UART/SPI/I2C), SpaceWire and Mil Std 1553 links, as well as high-performance processors SHA and TRNG.
(Source: Microchip (2022))

  - 384 Kbytes embedded SRAM for Tightly Coupled Memory (TCM) interface or System SRAM with ECC
  - 768 Kbytes of multiport SRAM with ECC
  - One PLL for system clock, one PLL for peripherals
- Communication Peripherals
  - Ten FLEXCOMs, each supporting USART/UART, SPI and TWI/I²C.
  - Single data rate transfer Quad I/O Serial Peripheral Interface (QSPI)
  - SpaceWire interface with two SpaceWire ports with integrated RMAP support and embedded SpaceWire router

The SAMRH71 has a built-in advanced DSP hardware accelerator that supports single instruction multiple data (SIMD) processing, saturation arithmetic instructions, and single-cycle multiply-add instructions. Its interrupt system is managed by a Nested Vector Interrupt Controller (NVIC), which supports efficient interrupt handling and priority management. It can also be Debugged via JTAG or Serial Wire Debug (SWD).

### 4.2.5 Design of the PBEE Prototype

The PBEE board design incorporates the following key components: the MCU, LVDS transceivers, the MBEE-PBEE interface, the PBEE-ICU interface, and the PBEE-PSU interface. An additional programming and debug interface is available on the board to upload and debug firmware of the MCU. The core processing unit of the PBEE is a SAMRH71 radiation-hardened microprocessor from Microchip Technologies, positioned at the center of the PBEE board. The controller is the interlink between the DHU of the LAD at one end, the various MBEEs on the other. It receives commands from the DHU (via SpaceWire), processes them, forwards them to the MBEEs (via twisted-pair cables), gathers housekeeping, receives and temporarily stores science data frames, and transmits both science and housekeeping frames to the DHU (via SpaceWire). The processor interfaces with external LVDS transceivers to handle communication with the MBEEs. Various analog housekeeping parameters, including currents, voltages, temperatures, and position switches, are measured within the PBEE, amplified, converted to digital signals, and fed into the processor at a rate of once per second. Figure 4.6 shows a 3D rendering of the PBEE.

External LVDS transceivers are employed to convert single-ended signals into differential signals for communication with the MBEEs. Specifically, radiation-hardened dual LVDS transceivers (RHFLVDSR2D2) are utilized for the MBEE interface, while

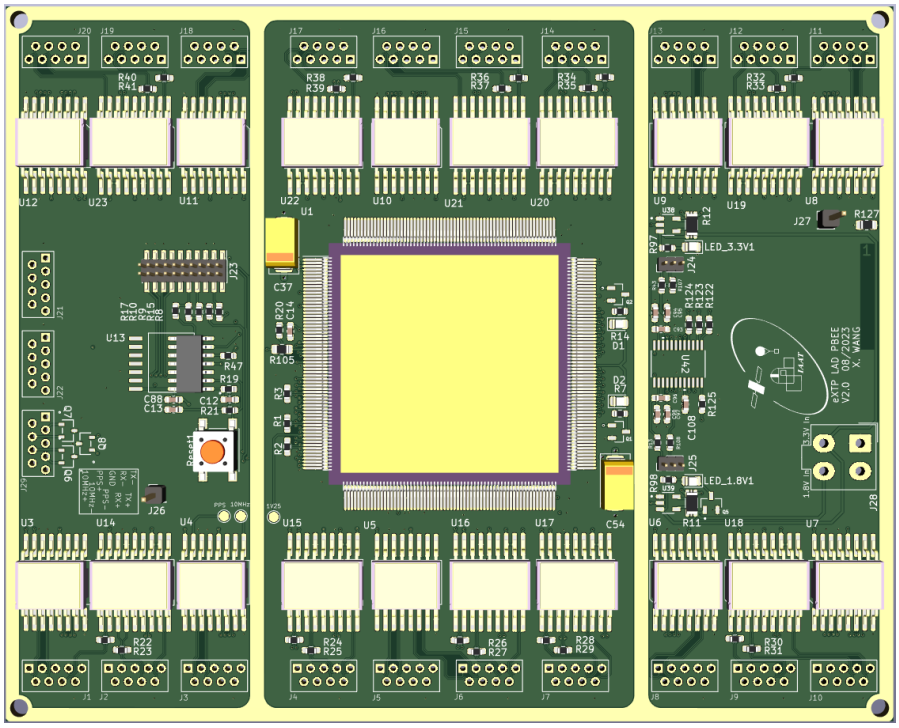

Figure 4.4: 3D views of the final PBEE PCB.

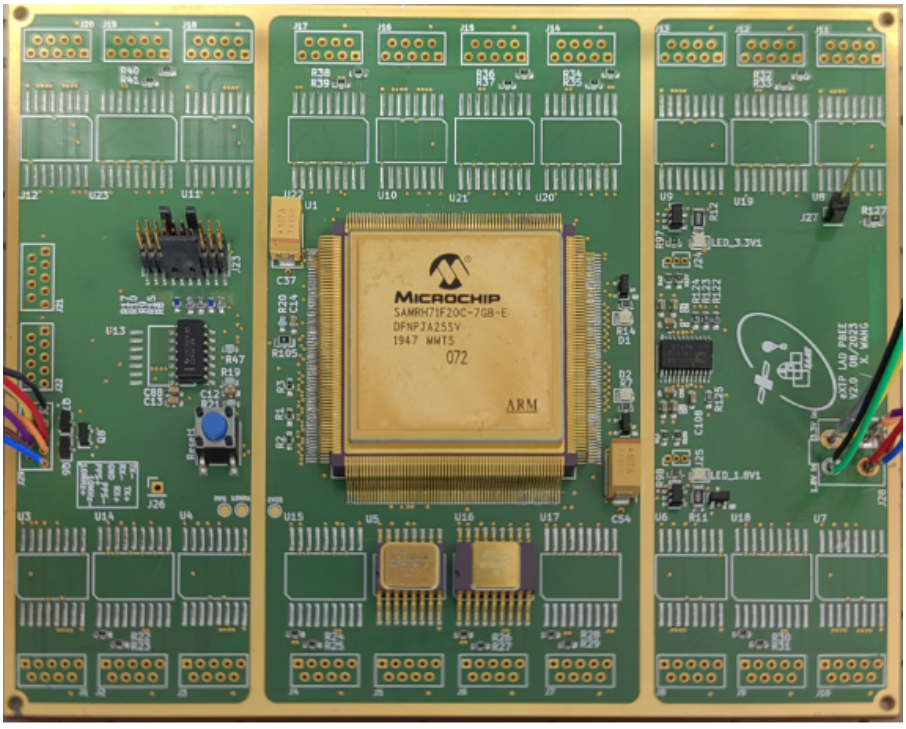


Figure 4.5: The PBEE prototype board features a connector on the left side for interfacing with the ICU, while the upper and lower rows of connectors are designated for communication with the MBEE. The power input interface is located on the right side of the board. It should be noted that some of the LVDS transceivers in the diagram are not soldered.

4-channel transceivers (RHFLVDS31A and RHFLVDS32A) are implemented for the timing interface (PPS and HAC 10 MHz). The SpaceWire interface to the ICU leverages the integrated LVDS transceivers within the MCU. Each PBEE accommodates 20 MBEE connectors.

In the current design, two LVDS receivers (RHFLVDS32A) are deployed to receive timing signals from the ICU, enabling warm redundancy for the timing interface. A single LVDS driver (RHFLVDS31A) distributes timing signals to two MBEEs, requiring a total of ten LVDS drivers to implement the timing interface across the PBEE. Additionally, one LVDS transceiver (RHFLVDSR2D2) manages the data and command interface for two MBEEs, necessitating ten RHFLVDSR2D2 units for all 20MBEEs. To optimize power efficiency, the LVDS transceivers for the main data interface are activated exclusively during data transfer operations.

The PBEE board is powered by two primary power rails supplied by the PBEE PSU. The PBEE board integrates a radiation-resistant precision shunt regulator (RHF100) to provide a high-precision reference voltage for the SpaceWire interface. The reference voltage is stabilized at a 1.25V common-mode level to ensure reliable transmission of bus signals in space radiation environments.

The PBEE incorporates two LVDS clock inputs from the ICU: the Pulse Per Second (PPS) and the High Accuracy Clock (HAC). The PPS provides absolute timing synchronization, aligning with the Global Navigation Satellite System (GNSS) time reference. Its timing accuracy is maintained within 1 µs when GNSS signals are available, and it exhibits a drift rate of less than 0.5 seconds per day during GNSS outages. The HAC, operating at 10 MHz, delivers differential timing with a resolution of 100 ns. Additionally, the HAC serves as an external clock source for the MCU. These two clock signals provide MBEE with a time stamp function for triggering events, enabling precise time information acquisition through dual clock time value recording.

The PBEE schematics and printed circuit board (PCB) were designed using KiCad, a cross-platform, open-source electronic design automation suite. The design files were managed and collaboratively developed using IAAT's internal GitLab repository. The dimensions of the board were determined by the requirements of its Mechanical Interfaces, which resulted in a 134mm x 108mm rounded rectangle with four fixed-position mounting holes.

A manual reset button and Serial Wire Debug (SWD) connector are provided for ease of debugging and programming during development. Of the three voltages used by the board, 3.3 and 1.8 volts are provided by two power supply terminals, and the third

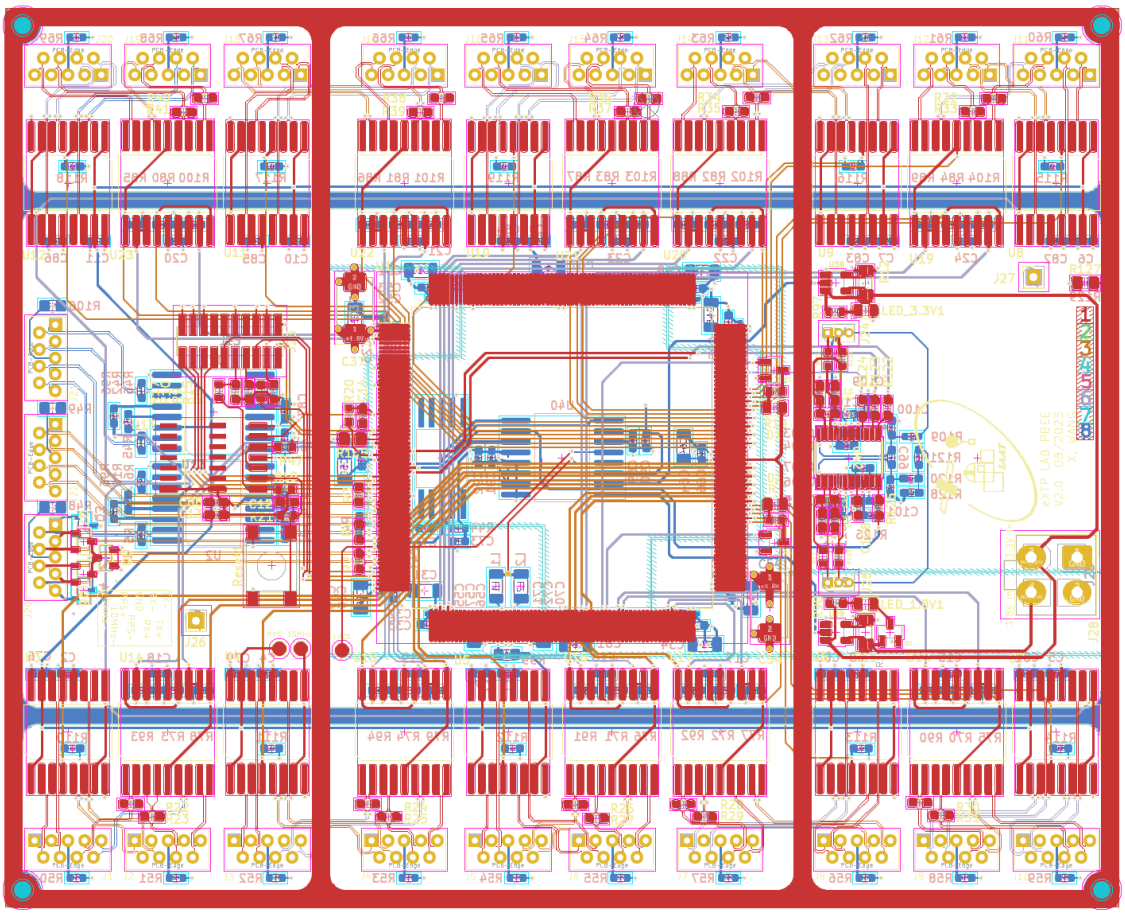

Figure 4.6: The PBEE prototype PCB layout. The SAMRH71 MCU, a central component of the PBEE design, is positioned at the board's center. Flanking the MCU are LVDS transceiver and connectors, which facilitate communication with external modules.

voltage, 1.25V (for the spaceWire), is generated by a shunt regulator.

### ICU-PBEE Electrical Interfaces

There are two types of connectors linking the ICU and PBEE. The first type is a standard SpaceWire connector, which is a 9-pin micro-miniature D-type connector specifically selected for its suitability in space applications. This connector consists of eight signal contacts and one screen termination contact, with additional details provided in the ECSS-E-ST-50-12C documentation. In the PBEE design, there are two connectors to accommodate both random and nominal connections between the ICU and PBEE. The second type of interface is dedicated to timing, enabling the transmission of a 10MHz High Accuracy Clock and Pulse-Per-Second signals from the ICU to the PBEE. The pin configuration for this timing interface is detailed in Figure 4.7.

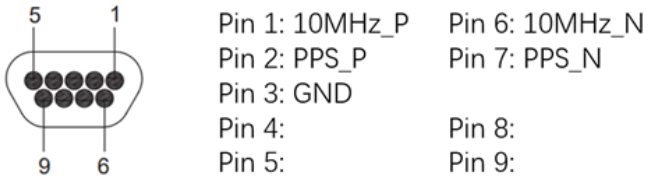


Figure 4.7: The connector layout used for the ICU - PBEE prototype timing interface (PBEE Side), where *_P denotes the positive signal and *_N denotes the complementary signal of the differential pair.

### PBEE-MBEE Electrical Interfaces

A straightforward full-duplex asynchronous interface has been implemented between the PBEE and MBEE to streamline the harness and connector design. Data originating from the MBEE is transmitted through the receive channel (RX_P/N), while data sent from the PBEE to the MBEE is transmitted via the transmit channel (TX_P/N). Additionally, the timing signals are transmitted to the MBEE through the same harness. This approach significantly reduces the number of harnesses required and adheres to weight budget constraints. To enhance data transmission reliability and extend the communication range in the harsh environment of outer space, LVDS differential pairs are utilized.

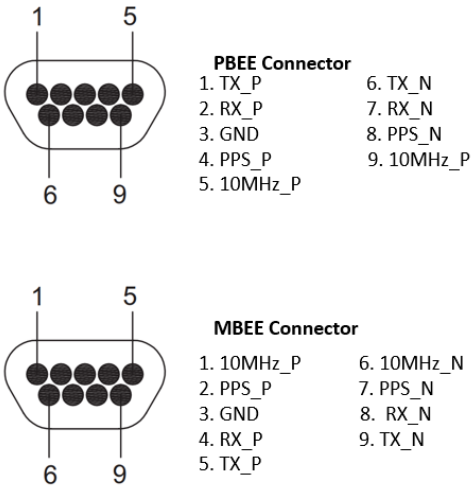


Figure 4.8: The connector layout used for the MBEE-PBEE prototype interface employs a Micro-D 9-pin space-qualified connector.

## 4.3 Firmware

This section describes the software design of the PBEE, which is essential for achieving its intended functionality after all hardware components have been selected. This was one of the primary focuses of this thesis. First, the functional blocks of the PBEE software are explained, followed by an introduction to the communication protocol of the LAD. The external interfaces of the PBEE firmware design, i.e., the MBEE interfaces and the ICU interface, are also described in detail.

### 4.3.1 Firmware Functional Blocks

The PBEE firmware is based on a real-time operating system (RTOS) and is designed to process data and events within tightly defined time constraints to ensure a timely and deterministic response, which is critical for applications such as embedded systems. PBEE is primarily used for managing multi-task scheduling, interacting with the ICU, communicating with multiple MBEEs, processing commands and telemetry, and generating and collecting HK data. As a router in the LAD system, PBEE has very high real-time requirements and must respond to the commands from ICU and process scientific data from MBEEs efficiently to ensure the stable operation of the system. The main function of PBEE is to continuously listen to and receive commands from ICU and respond to them in a timely manner. It is also responsible for polling scientific data from all 10 modules. MBEE time stamps the scientific data and packages it into communication packets, which are then transmitted to PBEE, where they are buffered,

reformatted, and ultimately routed to the DHU. The PBEE software is responsible for the following functions:

- Managing PBEE operational mode transitions
- Handling TM/TC (Telemetry/Telecommand) interfacing with the ICU over nominal/redundant SpaceWire links
- Executing TCs (Telecommands) and distributing them to the MBEE
- Acquiring scientific data from the MBEE
- Buffering event data packets
- Reformatting scientific data and forwarding it to the DHU (Data Handling Unit)
- Collecting HK (Housekeeping) data and generating HK packets
- Controlling the power on/off of the MBEE
- Distributing differential time to the MBEE
- Implementing PBEE Failure Detection, Isolation, and Recovery (FDIR) algorithms and procedures

Figure 4.9 illustrates the block diagram of the PBEE software architecture at the conclusion of Phase B of the eXTP mission. The software components are organized and layered according to their functionalities. After defining the software requirements and architectural design based on the previously established PBEE specifications, the software development will be completed in the subsequent phase. The next phase of the mission will implement additional functionalities, such as PUS (Packet Utilization Standard) services, diagnostic data, memory management, and more.

Several software layers can be identified within the PBEE software:

- **Hardware Driver Layer**: Corresponds to the drivers interfacing with the lower-level system hardware.
- **Functional Layer**: Necessary for interacting with PBEE's internal and external devices.
- **Management Layer**: Responsible for managing these functionalities when invoked.

The main software components of the PBEE include:

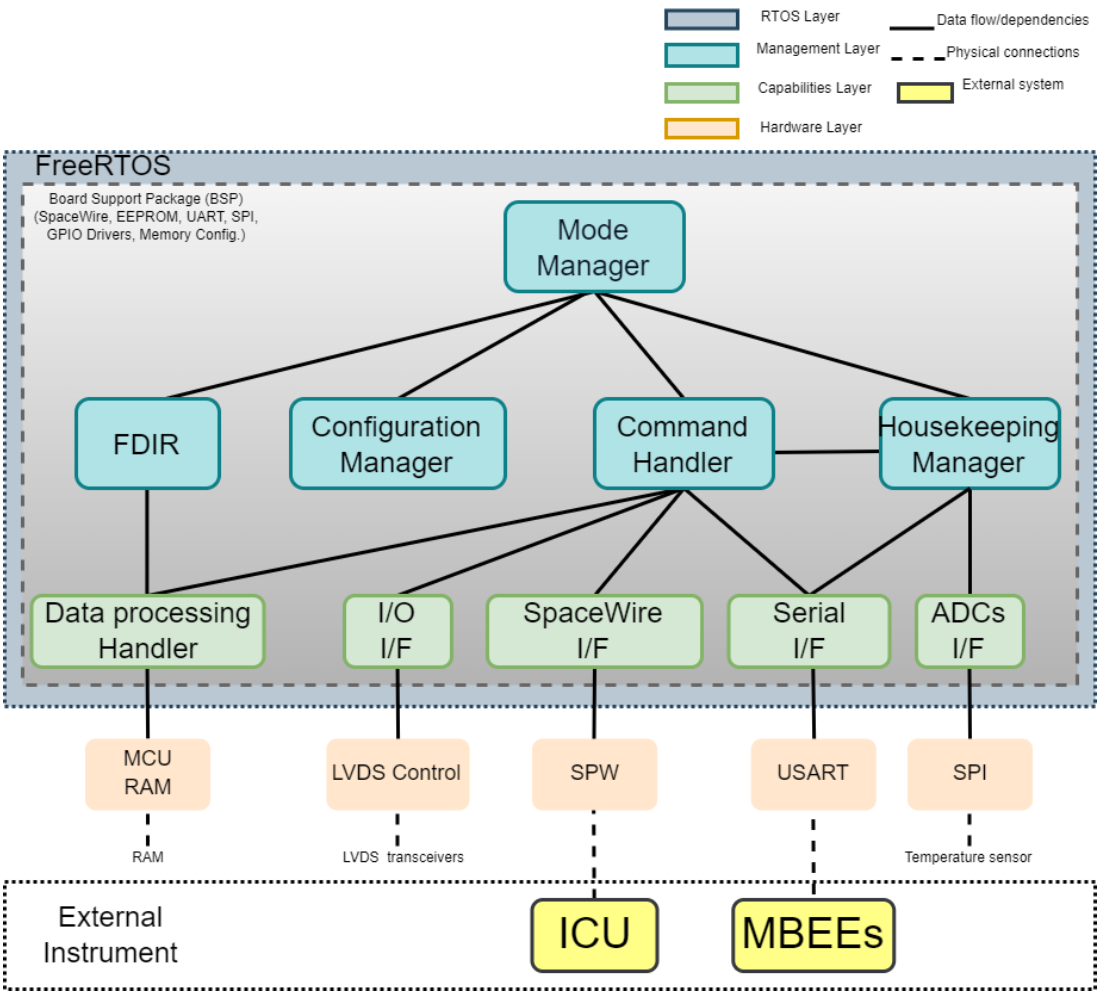


Figure 4.9: The PBEE data processing software architecture diagram. This diagram presents the architecture of the PBEE data processing software, highlighting the integration of functional and structural elements within the system. Solid lines illustrate the flow of data and logical dependencies between software components, defining the operational pathways for information exchange. Embedded within the architecture are FDIR modules, which ensure system resilience by continuously monitoring for anomalies, isolating faults, and triggering recovery protocols to mitigate mission risks. The I/F (Interface) components establish connections to external instruments such as the ICU, MBEEs, and other PBEE hardware devices, with these physical linkages explicitly represented by dashed lines in the diagram.

- Mode Manager: A component responsible for implementing PBEE operational modes and managing permitted transitions.
- FDIR: This functionality, aimed at reducing mission failure risks, will be implemented in the next phase of the study.
- Configuration Manager: Handles the storage of parameter data required to configure PBEE and MBEE in various modes. These parameters can be updated via the DHU.
- Command Handler: Receives Telecommands (TCs) from the ICU, checks their validity using Cyclic Redundancy Check (CRC), and verifies their acceptance based on the operational mode. It then executes the commands on the PBEE or sends the decoded commands to a message queue for transmission to the MBEE.
- HK (Housekeeping) Manager: This component polls for HK data from the device using SPI, generates and formats HK Telemetry packets, and sends them to the ICU. Certain critical parameter values will also be monitored for FDIR purposes in the next phase of the mission.

### 4.3.2 LAD Communication Protocol

The communication protocol serves as the data transport layer for the LAD onboard eXTP. Reflecting the hierarchical hardware architecture of the LAD instrument, the protocol defines distinct communication segments for the ICU-PBEE and PBEE-MBEE interfaces, ensuring scalability and modularity. It encompasses two distinct communication segments:

- **ICU-PBEE Interface**: Utilizes SpaceWire for high-reliability command and telemetry exchange.
- **PBEE-MBEE Interface**: Implements UART-based communication for subsystem-level data transfer.

To support instrument operation and scientific data transmission, the protocol employs standardized packets featuring a fixed-header structure with variable-length payloads. This design accommodates both electronics control commands (fixed-size operational directives) and variable-volume scientific data streams. As illustrated in Figure 4.10, each protocol packet consists of immutable header fields that define the packet type, destination, and integrity checks, alongside payload sections that are dynamically

sized based on the complexity of the command or the volume of scientific data being transmitted. This dual-segment, fixed/variable hybrid architecture optimizes bandwidth utilization while maintaining deterministic behavior for command execution.

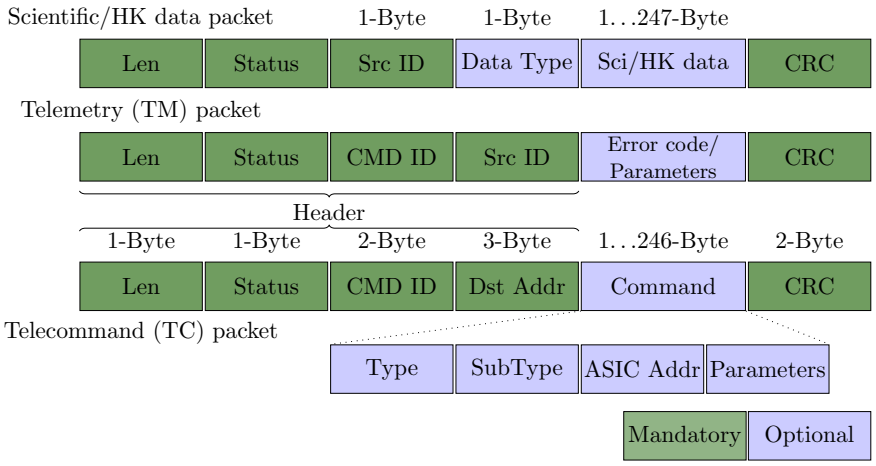


Figure 4.10: The LAD communication protocol format. Top a): Scientific/HK data packet scheme. Middle b): Telemetry packet scheme. Bottom c): Telecommand packet scheme

The protocol packets of LAD are categorized into three types of commands: Scientific Event/HK packets, Telemetry (TM) data, and TC packets. As shown in Figure 4.10.a), this packet encapsulates either observation science data or HK data. The packet type is distinguished by specific bits in the status field (Stus) of the packet frame. The HK information is included in the data structure, which contains the device's electrical parameters, temperature, and operational information. Each command consists of a command type, a command subtype, and optional command parameters, which are often used to configure the instrument, and together form a unique executable TC. The telemetry packet scheme follows a similar structure to the Scientific Event/HK packet as shown in Figure 4.10.b, they all have the same 1-byte source ID to identify the source of the data. When the packet is sent from the PBEE to the ICU, this byte is appended to indicate the PBEE and MBEE IDs, where the high 3 bits indicate the PBEE ID and the low 5 bits indicate the MBEE ID. The command portion of the TC packet shown in Figure 10.c) is customisable.

The communication packets are structured to sequentially include the following three major fields:

- **Packet Header** (7 bytes for command packet, 3 bytes for scientific data packet, mandatory): Contains essential metadata such as packet type, destination, and sequence information.

- **Data or CMD (Command) Field** (0 to 246 bytes, optional): Carries the payload, which may consist of operational commands or scientific data, with a variable length depending on the specific requirements of the transmission.
- **CRC Field** (2 bytes, mandatory): Provides a Cyclic Redundancy Check value to ensure data integrity and error detection across the packet.

The structure depicted in Figure 4.10 represents the current baseline design for the LAD communication protocol. The following describes the principal fields and their intended functionalities, which are defined to meet the key requirements of data integrity (e.g., CRC), routing (e.g., Destination Address), and command execution (e.g., CMD ID). While the specific implementation may be optimized in future development cycles, the core functions of these fields are expected to remain stable.

- **Length**: the first byte contains the information of the length of the package which can be easy to use to read a complete package during the communications. And this field indicates the complete length of the package.
- **Status Flag**: the second byte contains the Status of the package. The explanation of each bit are list in Table 4.1.

Table 4.1: The bit definitions and functional descriptions of the packet status frame

| Bit | Name | Explanation |
|---|---|---|
| 0 | ICU cmd flag | Indicates packet is a PC to ICU communication. |
| 1 | ALERT bit | Indicates an event originating from MBEE, PBEE, or ICU. Might be a scheduled event or unexpected. |
| 2 | “Get” answer bit | Indicates the package is an answer to a “Get” command. |
| 3 | MBEE HK bit | Indicates the package contains MBEE housekeeping data. |
| 4 | PBEE HK bit | Indicates the package contains PBEE housekeeping data. |
| 5 | ACK bit | Indicates the telecommand executed by the electronics end when it raises. |
| 6 | ERROR bit | Indicates a command or automated process returned errors. May be sent in response to TC or as an unsolicited ALERT packet. Refer to section 3.4.2.5 for error codes. |
| 7 | Data type bit | Indicates what type of package, command, or scientific data transfer. (0b: Command / 1b: Scientific Data) |

- **CMD ID**: The unique identifier for the TC package.

- **Destination Address**: This field contains two pieces of information: the PBEE ID and the MBEE ID. Bits 0 to 19 are defined as the MBEE ID, while bits 20 to 23 are defined as the PBEE ID. Each bit position indicates an ID number.
- **Source ID**: This address will be converted into a 1-byte source ID when the packet is sent from PBEE. This byte includes both the PBEE ID and the MBEE ID. The value in bits 0 – 4 represents the MBEE ID, while the value in bits 5 – 7 represents the PBEE ID.
- **Command**: Includes all executable commands for the electronic end.
- **CRC**: This information is used to verify the correct transmission and reception of the frame. The CRC algorithm parameters are list in Table 4.2

Table 4.2: CRC algorithm parameters

| Algorithm | Check | Poly | Init | RefIn | RefOut | XorOut |
|---|---|---|---|---|---|---|
| CRC-16/AUG-CCITT | 0xE5CC | 0x1021 | 0x1D0F | false | false | 0x0000 |

### 4.3.3 Data Rates

The science telemetry budget estimate for LAD is based on assumption of default event-by-event data, where each event is described by 58 bits of data. A source intensity of ∼15 Crab (Feroci et al., 2022) was used as an assumption of the maximum radiant intensity in the field of view, a parameter that represents the maximum data output that could be generated during the observation, which is the worst-case scenario for instrument operation.

Based on these assumptions, the maximum expected count rate of the LAD can be ∼2,011,259 counts/s. The estimated data transfer rate for each half-module MBEE is calculated to be ∼1.75 Mbps. Notably, the design incorporates a 20% margin to ensure that the system can efficiently handle additional data loads beyond the estimated maximum rate, thereby improving the reliability and robustness of the instrument.

### 4.3.4 Operation Modes and Mode Transitions

This section presents the operational modes and their transition mechanisms of the PBEE as specified in the LAD Requirement Specification. The PBEE is designed to perform multiple functions, including scientific data acquisition, system configuration, engineering verification tests, and initialization procedures during system startup.

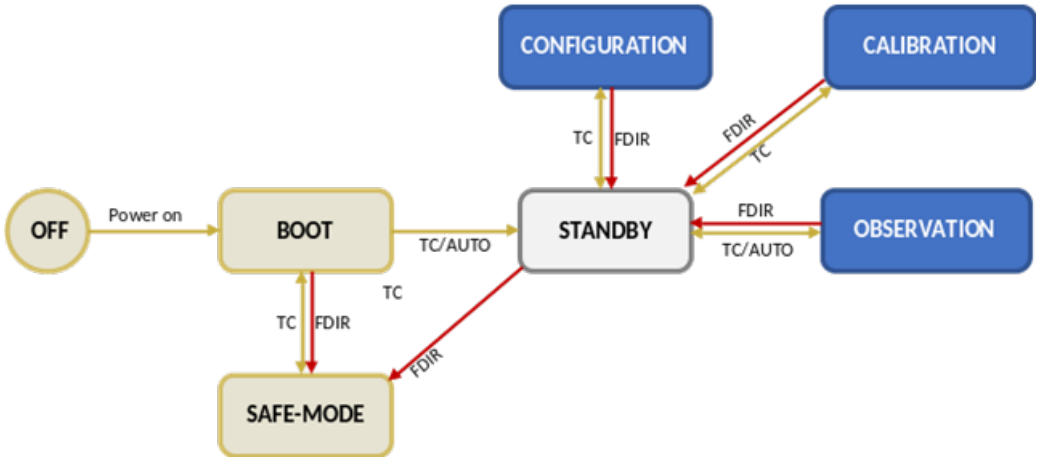


Figure 4.11: The PBEE operating modes and transitions.

Figure 4.11 provides a schematic representation of the currently defined PBEE operational modes and their permissible transitions. The diagram illustrates the state transition logic between various operational modes, which can be initiated through two distinct pathways: (1) via telecommand (TC) from ground control, or (2) through autonomous system responses. Notably, the latter includes automatic transitions to safe mode when the system detects anomalies or critical failures, ensuring system protection and data integrity.

The list of the defined PBEE operation modes with a description is the follow:

- **Off mode**

  In this initial state, as the name suggests, the PBEE remains powered off.

- **Boot mode**

  This is a transitional operation mode in which the PBEE switches from a power-off state to power-on. During the power-on procedure, the PBEE should be configured to ensure that all critical signals are in a known or safe state, preventing erratic or metastable conditions that could lead to electronic failures.

- **Safe mode**

  This mode can be accessed from any other operational mode. Its primary function is to provide the instrument with essential capabilities to detect functional anomalies while ensuring the safe operation of fundamental power supply systems. The PSU functions are strictly regulated and can only be activated or deactivated via TC. When transitioning from Operational Mode to Safe Mode, all MBEEs must be immediately powered off. In this mode, only a restricted set of commands

is permitted, including transitions to other allowed modes. Observation data transmission is not allowed in this mode.

- **Standby mode**

  Following a successful power-on procedure, if the safe flag register is clear, the PBEE should transition into Standby Mode. In this mode, data acquisition remains disabled, and MBEEs remain unpowered (i.e., Off), while HK data and the PSU continue routine operations. This mode serves as the default state before initiating observations.

- **Configuration mode**

  In this mode, it should be possible to modify the PBEE and MBEE configuration parameters stored in RAM. The MBEEs remain in Configuration Mode, where they store essential operational registers and parameters—such as pedestal values, gain settings, and ASIC configurations—in non-volatile memory. However, these registers should be adjustable via TC to meet specific mission or engineering requirements. To prevent undefined behavior and ensure safety, most registers should only be modified while in Configuration Mode, except for those explicitly designated as safe for modification or when functionality necessitates it (e.g., the operation mode register).

- **Engineering mode**

  This mode offers a transparent mode allowing the detectors to be readout passing as much information as possible. Transparent information bypass offers debugging capabilities to identify and ensure correct behaviour of the MBEEs and data processing pipelines.

- **Observation mode** The main operation mode allows for the activation of all MBEEs individually, provided no failures are detected. Commands from the ICU can be used to transition MBEEs into different modes as needed. In this mode, the power supply operates stably, HK TM processing is enabled, and HK routines run automatically. The PBEE utilizes this mode to conduct LAD science observations. If the MBEEs are powered on in Observation Mode, the module configuration parameters stored in RAM shall be transferred to the respective module.

# 5 LAD Integration and Test

This chapter presents the experimental validation of the PBEE prototype described in Chapter 4, a critical component for the eXTP/LAD instrument. The test campaign was conducted at Thales Alenia Space Italia laboratory beginning January 2024. All testing procedures adhered to the European Cooperation for Space Standardization (ECSS) standards, specifically the test requirements defined in ECSS-E-ST-10-03C and the verification framework outlined in ECSS-E-ST-10-02C.

The validation began with preliminary functional tests of the PBEE circuit board, followed by its integration into the full LAD data processing chain for system-level testing. Subsequently, the team conducted end-to-end data acquisition experiments using $^{55}$Fe and $^{109}$Cd radioactive sources to validate and characterize the system performance.

## 5.1 Electrical Tests

The electrical characterization of the eXTP/LAD PBEE prototype included signal integrity assessment, impedance matching verification, power quality analysis, and inrush current monitoring. Prior to system-level power-on, comprehensive insulation resistance tests were performed on the digital interfaces and cable harness. All results met the requirements of ECSS-E-ST-20-07C and the design specifications, ensuring electrical safety and signal transmission integrity.

Power consumption is a critical parameter for the LAD instrument, as the eXTP satellite employs a solar-battery power system. The test setup incorporated independent power distribution units for the PBEE and MBEE. High-precision digital multimeters and current probes provided real-time monitoring of all power rails. Test data indicate that under typical operating conditions, the peak power consumption values were 7.1 W for the ICU, 2.1 W for the PBEE, and 3.3 W for the MBEE (including its MPSU). These measurements were obtained from an Engineering Model (EM) that implements only partial functionality compared to the final flight design. Consequently, power consumption for the flight models is projected to be higher. The measured power

consumption of the ICU (7.1 W) and PBEE (2.1 W) demonstrators remained well below their respective design thresholds of 15 W and 4.4 W. This provides adequate margin for future scaling to flight-ready systems.

During power-on, the PBEE exhibits an inrush current. This inrush current can impact battery performance and other electronics on the shared power bus. The inrush current shape are measured with a current probe and an oscilloscope connected on each positive primary bus line at a time, in single shot mode. During testing, the 1.8 V supply (core voltage for the PBEE's microcontroller) was enabled first. The 3.3 V supply was then activated, following the prescribed PBEE startup sequence.

The 3.3 V power supply is essential for the microcontroller peripherals of the PBEE. The inrush current for the 3.3 V supply reached approximately 0.09 A with a duration of 0.1 ms, as shown in Figure 5.1 (left).

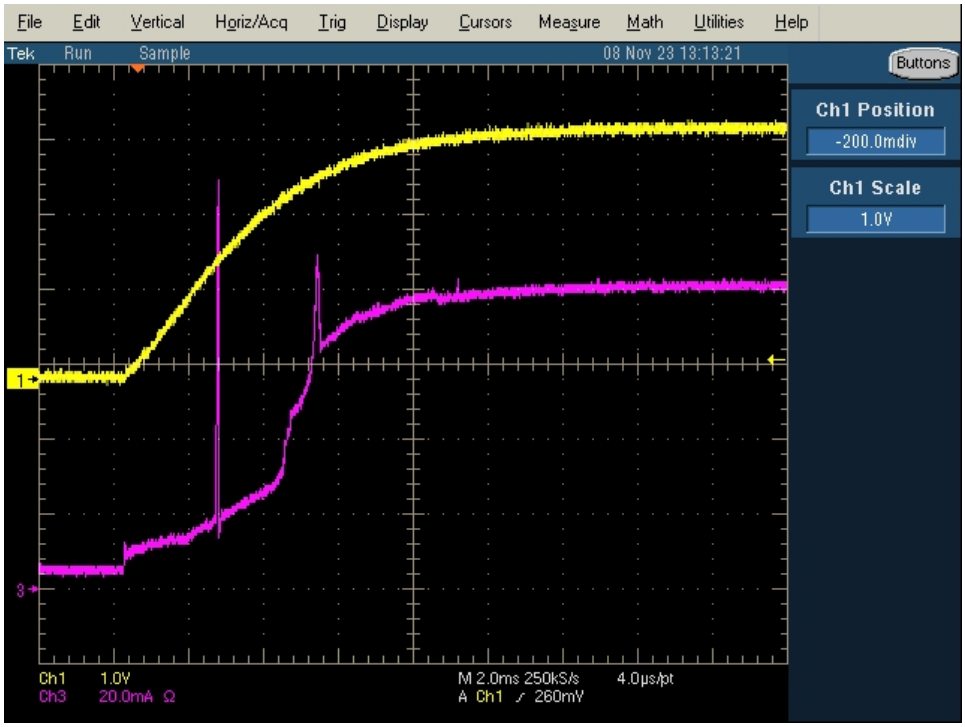


Figure 5.1: The inrush behavior of LAD PBEE is shown, with the yellow trace indicating the 3.3 V voltage and the purple trace representing the 3.3 V current. A peak inrush current of 90 mA is observed approximately 0.1 ms after the voltage ramp-up initiates.

## 5.2 Functional Tests

Functional validation of the PBEE employed a system-level integration approach, wherein the PBEE was evaluated within the complete LAD data processing chain.

The test platform configuration is illustrated in Figure 5.2.

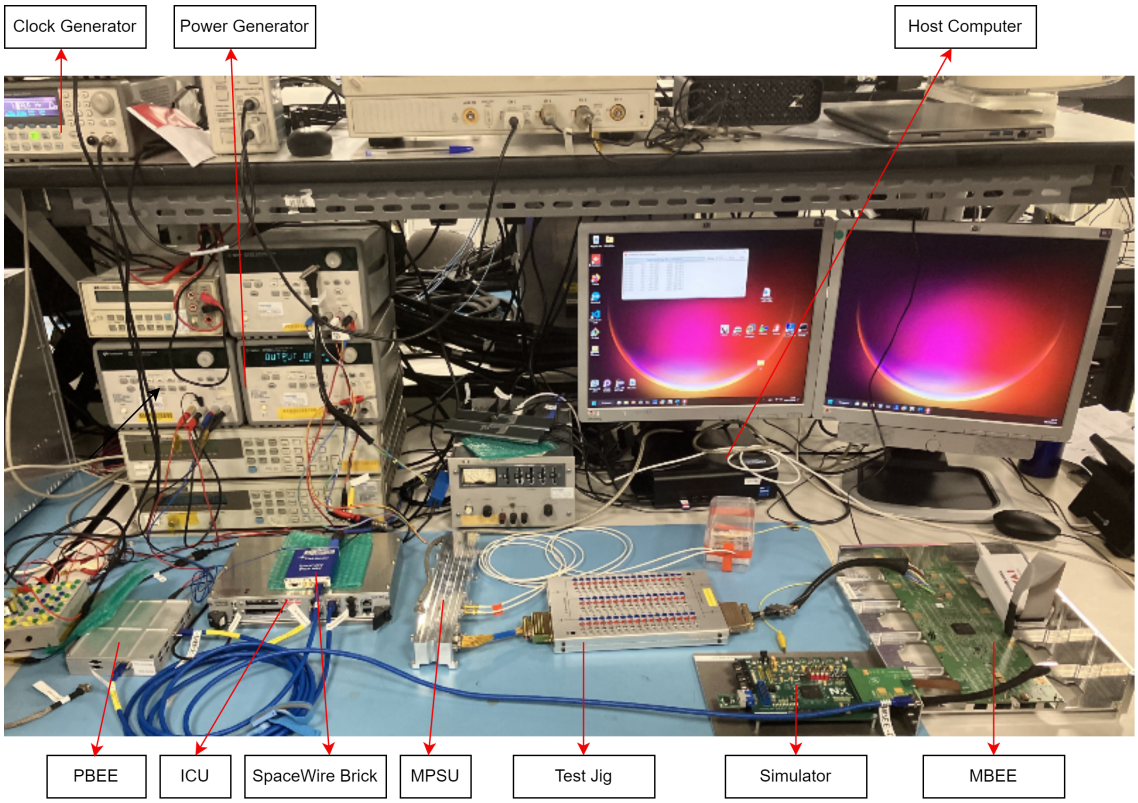


Figure 5.2: The setup of the LAD joint test bench demonstrates the integration of the back-end electronics developed by IAAT Tübingen and the MPSU developed by the Space Research Center of the Polish Academy of Sciences (CBK PAN).

### 5.2.1 Tests Setup

The Functional test category encompasses all procedures designed to validate the functional and performance characteristics of the equipment. These tests verify the integrated functionality of the hardware (HW), firmware (FW), and software (SW). Functional testing was conducted after verifying the electrical signal characteristics, as detailed in Section 5.1. All functional tests described herein were performed using dedicated Test Equipment (TE). The standard test configuration required the Equipment Under Test (EUT) to be fully integrated and connected to the TE.

The functional test sequence proceeded as follows:

- Interface Integration and Configuration
  - Establish connections between test system components:

    - Connect the ICU with the Electrical Ground Support Equipment (EGSE).
    - Connect the PBEE module to the ICU.
    - Connect the MBEE module with the PBEE.
    - Connect a FEE to the MBEE.
  - Power-on all units and verify that each board attains its nominal operational state. Configuration and re-programming of main components are facilitated via EGSE-controlled computers.

- Operational Mode Verification
  - Command transitions between different operational modes for all test units.
  - Read and verify the corresponding control and status registers to confirm mode transitions and system behavior.

- Housekeeping (HK) Data Acquisition
  - Retrieve and analyze HK register data from each unit under test to assess system health and monitor operational parameters.

- Scientific Data Acquisition
  - Transition the MBEE to observation mode and acquire data packets.
  - Inspect and validate the integrity and content of the generated scientific data.

- Timing Performance Evaluation
  - Analyze the temporal behavior of received scientific data.
  - Evaluate timing accuracy and consistency by inspecting related registers and identifying any timing-related errors.

- Calibration and Transparent Readout Mode
  - FEE generates events that can be feed back to MBEE. Verify data transmission.
  - Change some register patterns in the MBEE pipeline and see if they are correctly implemented.
  - Inject test signals within the ASIC to check Gain calibration etc.
  - Engage calibration mode and perform data readout operations to assess calibration integrity and data path functionality.

The test bench incorporated a signal generator to provide the PPS and 10 MHz HAC signals, which were distributed from the PBEE to the MBEE. The EGSE transmitted telecommands to the ICU, which was connected to the EGSE via a SpaceWireBrick Mk4 at a data rate of 200 Mbit/s. Command interface tests were conducted on the ICU to assess its responsiveness and functional correctness. The ICU's various operational modes were also tested to verify compliance with the LAD instrument's specifications and design requirements. Following PBEE integration, remote commands were sent via the EGSE to evaluate the ICU-PBEE interface. This phase aimed to validate the reliability of ICU-PBEE communications, ensuring robust data exchange and command execution.

Testing focused on confirming the PBEE' s ability to execute diverse tasks under ICU control. The outcomes were assessed against functional, timing, and performance design criteria. Throughout validation, particular attention was paid to verifying the PBEE' s execution of tasks in response to ICU remote commands.

The MBEE was then integrated into the test sequence, with all verification procedures conducted per its design specifications. Within the system architecture, the PBEE functions as a command router by receiving telecommands from the ICU, processing them, and distributing them to the appropriate MBEE. Upon receiving a command, each MBEE performed interpretation and execution, then generated and transmitted a response. The PBEE-MBEE communication interface was implemented using UART protocol transmitted via LVDS signaling.

### 5.2.2 Command & Control

The LAD is commanded and controlled by the Payload Data Processing Unit (S/C level) (PDPU) via a cold-redundant SpaceWire communication channel, which adheres to the avionic bus standard at both the Physical and Data Link Layers. At the Application Layer, a customized implementation of the ESA Packet Utilisation Service - C (PUS-C) is employed as described in Section 4.3.2, featuring structured TeleCommands (TCs) and TeleMetries (TMs) in a predefined format.

The SpaceWire functionality is physically integrated into the LAD ICU-DHU board, where it operates through the Leon4 GR740 Peripheral interface. Timing signals at the ICU level are received from the S/C Spacecraft Management Unit (SMU) and subsequently relayed to the PBEE board using the SpaceWire protocol. Concurrently, science telemetry data is transmitted back to the ICU over the same SpaceWire link, while timing signals are distributed via a dedicated LVDS line that leverages the SpaceWire Physical Layer.

Table 5.1: Telecommand Service Classification of PBEE

| **Service Name** | **Type** | **TC (type,subtype)** | **TC Short Description** |
|---|---|---|---|
| TELECOMMAND HK oriented | 3 | TC (3,5) | Enable Housekeeping Parameter Report Generation |
| | 3 | TC (3,6) | Disable Housekeeping Parameter Report Generation |
| | 3 | TC (3,31) | Define Housekeeping Parameter Report Collection Interval |
| | 3 | TC (3,33) | Get Housekeeping Interval Time |
| | 3 | TC (3,128) | Get a Housekeeping Data Packet |
| TELECOMMAND Management oriented | 17 | TC (17,1) | Perform Connection Test |
| | 17 | TC (17,128) | Test Telecommand of Maximum Length |
| TELECOMMAND Science Data Transfer oriented | 24 | TC (24,1) | Enable/Start Science Transfer from User |
| | 24 | TC (24,2) | Disable/Stop Science Transfer from User |
| | 24 | TC (24,128) | Reset Output Buffer |
| TELECOMMAND Instrument oriented | 25 | – | Set MBEE/PBEE Mode |
| | 25 | TC (25,0) | PBEE Boot |
| | 25 | TC (25,1) | PBEE Stand-by Mode |
| | 25 | TC (25,2) | PBEE Safe Mode |
| | 25 | TC (25,3) | PBEE Configuration Calibration Mode |
| | 25 | TC (25,4) | PBEE Calibration Mode |
| | 25 | TC (25,5) | PBEE Observation Mode |
| | 25 | TC (25,6) | PBEE Firmware Reset |

To ensure redundancy, the timing interface between the ICU and PBEE employs two LVDS receivers (RHFLVDS32A), establishing a warm-redundant configuration. The PBEE further propagates timing and command/control signals to the LAD Module MBEE board via UART, incorporating science telemetry within an LVDS architecture that retains the SpaceWire Physical Layer structure.

Data packets and timing signals are embedded within the SpaceWire framework, with single-ended timing and TM/TC signals converted to differential signals using LVDS transceivers. Radiation-hardened dual LVDS transceivers (RHFLVDSR2D2) facilitate the MBEE interface, while 4-channel transceivers (RHFLVDS31A and RHFLVDS32A) manage the timing interface for PPS and 10MHz signals.

The LAD incorporates three distinct state machines, each corresponding to a key logical unit in the LAD System chain:

- **ICU-DHU**: Managed by the LEON4 GR740 MCU
- **PBEE**: Controlled by the SAMHR71 MCU
- **MBEE**: Operated via the NanoXplore NX1H35AS FPGA

A detailed modes transition diagram of PBEE illustrating these modes is provided in the Section 4.3.4. The MBEE were simulated, validated, and presented by Xiong et al. (2025).

The PBEE's implementation of the PUS service for operational mode transition management is detailed in Table 5.1.

## 5.3 Test with Radiation Sources

To fully evaluate the readout electronics performance, an end-to-end test was conducted with the integrated detector system. This included verifying the SDD' s ability to acquire spectra from radioactive sources under ambient conditions. In SDDs, the incident X-ray photon energy is linearly proportional to the amplitude of the output signal from the anode.

For each characteristic spectral line, the linear relationship between the channels and energy can be expressed as:

$$ADU = Gain * E + Offset \tag{5.1}$$

Where ADU and offset are expressed in instrument units, energy E is in keV, and gain units are ADU/keV (ADU is an Analog Digital Unit, also known as channels). The regression incorporates two free parameters: the gain (slope) and offset, which define the X-ray detector's response. This calibration procedure transforms the amplitude of X-ray events into standardized energy units, thereby finalizing the energy calibration.

The experiment uses a radioactive source with known characteristic energy for calibration, specifically Fe-55 (characteristic emission lines 5.9 keV and 6.4 keV) and Cd-109 (characteristic emission lines 22.10 keV and 25.02 keV). The LAD module was placed in a room-temperature laboratory environment and irradiated by these sources. The resulting spectra were calibrated using the prominent Mn K$\alpha$ (5.9 keV) and Ag K$\alpha$ (22.1 keV) emission lines. The total single-exposure durations were 15,360 seconds for $^{55}$Fe and 6,600 seconds for $^{109}$Cd.

It is important to note several experimental limitations during these tests. For instance, only a single IDeF-X ASIC was active, with the majority of its input channels disconnected. Figure 5.3 shows the histogram distributions of the ADC outputs (in ADU) recorded during irradiation with $^{55}$Fe and $^{109}$Cd.

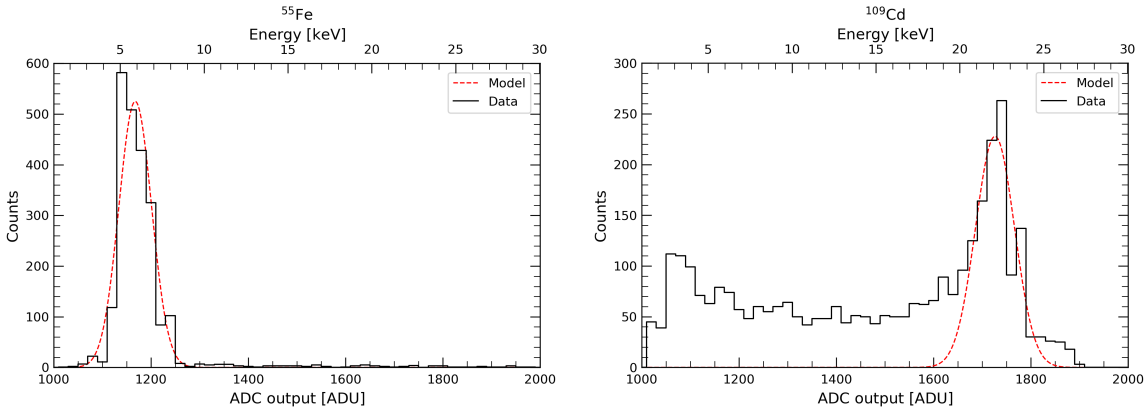


Figure 5.3: Characteristic X-ray spectra obtained from $^{55}$Fe and $^{109}$Cd radioactive sources. (a) Emission peak at 5.9 keV corresponding to $^{55}$Fe decay; (b) 22.1 keV emission line from $^{109}$Cd decay.

Because only a single anode channel was active, charge-sharing events that produce a low-energy tail in the spectrum could not be discriminated. A linear fit to the histogram peaks yielded the following ADU-to-energy relation:

$$ADU = 34.48 * E + 964.21 \tag{5.2}$$

The uncertainties in the fit parameters were: $\delta_{\text{GAIN}} = 1.41\,\text{ADU/keV}$, $\delta_{\text{OFFSET}} = 11.38\,\text{ADU}$.

However, minor discrepancies were observed between the energy values derived from the internal test pulse (VTEST) and the expected values.

$$E = \frac{C \cdot U \cdot w}{e} \tag{5.3}$$

Where:

- $E$ is the equivalent photon energy (eV),
- $C = 50\,\text{fF}$ is the input capacitance of the IDeF-X ASIC,
- $U$ is the amplitude of the injected test pulse (V)
- $w = 3.6\,\text{eV}$ is the average energy required to create an electron-hole pair in silicon,
- $e = 1.602 \times 10^{-19}\,\text{C}$ is the elementary charge.

Based on Equation 5.3, an equivalent expression to Equation 5.2 can be found:

$$ADU = 33.35 * E + 867.53 \tag{5.4}$$

A comparison between Equations 5.2 and 5.4 reveals discrepancies in the derived offset and gain parameters. While the system gain derived from the radioactive sources is consistent with expectations, a measurable baseline offset is evident. This offset is attributed to several factors: (1) the lack of precise calibration for the VTEST circuit, (2) uncertainty in the exact input capacitance, and (3) a disconnected voltage divider resistor in the VTEST configuration used during the test. Despite these discrepancies, which preclude a precise energy calibration at this stage, the experiment successfully demonstrated the fundamental functionality of the readout chain. The system reliably detected X-ray photons and produced a clear, quantifiable signal proportional to their energy. A full characterization of the scientific performance, however, is reserved for future work.

# 6 Discussion and Conclusion

X-ray astronomy provides a unique window into high-energy astrophysical phenomena throughout the universe. The penetrating nature of X-ray radiation allows the study of celestial objects and processes that are inaccessible at other wavelengths. These high-energy processes serve as irreplaceable natural laboratories for testing fundamental physics, such as general relativity and the EoS of matter under extreme densities. Building on decades of observational experience from rockets and satellites, X-ray detection technology continually advances in performance. In this context, sophisticated data processing systems have become increasingly critical for expanding the frontiers of astronomical discovery. Modern space-based observatories achieve high observational efficiency through advanced detector arrays, grazing-incidence optics, and specialized coating technologies.

As a core payload of the eXTP mission, the LAD was designed to play a key role in future X-ray astronomy. Its large effective area and high time resolution are achieved through an array of 640 SDDs. The hierarchical architecture of the back-end electronics —comprising FEE, MBEE, and PBEE levels—is designed to efficiently manage the high data rates generated by the detector array. The modular design organizes the 640 detectors into four independent groups, each managed by a dedicated PBEE to funnel data streams to the ICU. This thesis has focused on the development of the PBEE for eXTP/LAD, culminating in a fully functional prototype system based on the SAMRH71 microcontroller. The PCB design integrates 20 MBEE interfaces and implements a firmware architecture supporting scientific data preprocessing. Furthermore, a communication protocol system compliant with European Cooperation for Space Standardization (ECSS) space engineering standards has been specifically developed for the LAD instrument.

Verification tests confirmed that the PBEE's temporal performance and functional specifications meet design requirements. System-level integration testing successfully validated end-to-end data reliability from photon detection to the Electrical Ground Support Equipment (EGSE). Laboratory experiments involving the irradiation of detectors with radioactive sources successfully yielded first-light signals, demonstrating the effectiveness of the data processing chain. While single-chain verification has

been completed, subsequent multi-MBEE parallel processing capability tests remain necessary. PBEE' s multiple MBEE interfaces will connect to complete detection units to verify parallel communication performance under flight conditions. This research not only provides crucial technical reserves for the eXTP mission but also offers valuable methodological references for electronic system design in future X-ray astronomy projects (e.g., STROBE-X).

# Reference


Riccardo Giacconi. The dawn of x-ray astronomy. *Nobel lecture., ed. Giacconi, R*, 2002.

Cosimo Bambi and Andrea Santangelo. *Handbook of X-ray and Gamma-ray Astrophysics*. Springer Nature, 2024.

Riccardo Giacconi, Herbert Gursky, Frank R Paolini, and Bruno B Rossi. Evidence for x rays from sources outside the solar system. *Physical Review Letters*, 9(11):439, 1962.

Karl G Karl Jansky. Electrical disturbances apparently of extraterrestrial origin. *Proceedings of the Institute of Radio Engineers*, 21(10):1387–1398, 1933.

R Giacconi, H Gursky, and LP Van Speybroeck. Observational techniques in x-ray astronomy. *Annual review of Astronomy and Astrophysics*, 6(1):373–416, 1968a.

Andrea Santangelo, Rosalia Madonia, and Santina Piraino. A chronological history of x-ray astronomy missions. In *Handbook of X-ray and Gamma-ray Astrophysics*, page 5. Springer, 2023a.

Malcolm S Longair. *High energy astrophysics*. Cambridge university press, 2011.

Frank C Jones. Calculated spectrum of inverse-compton-scattered photons. *Physical Review*, 167(5):1159, 1968.

Claus Grupen. *Physics of Particle and Radiation Detection*, page 84. Springer International Publishing, Cham, 2020. ISBN 978-3-030-27339-2. doi: 10.1007/978-3-030-27339-2_4. URL https://doi.org/10.1007/978-3-030-27339-2_4.

George R Blumenthal and Robert J Gould. Bremsstrahlung, synchrotron radiation, and compton scattering of high-energy electrons traversing dilute gases. *Reviews of modern Physics*, 42(2):237, 1970.

Lev Titarchuk. Generalized comptonization models and application to the recent high energy observations. In *AIP Conference Proceedings*, volume 304, pages 380–384. American Institute of Physics, 1994.

AF Illarionov and RA Siuniaev. Comptonization, characteristic radiation spectra, and thermal balance of low-density plasma. *Soviet Astronomy, vol. 18, Jan.-Feb. 1975, p. 413-419. Translation. Astronomicheskii Zhurnal, vol. 51, July-Aug. 1974, p. 698-711.*, 18:413–419, 1975.

RA Sunyaev and LG Titarchuk. Comptonization of x-rays in plasma clouds-typical radiation spectra. *Astronomy and Astrophysics, vol. 86, no. 1-2, June 1980, p. 121-138.*, 86:121–138, 1980.

Andrea Santangelo, Rosalia Madonia, and Santina Piraino. A chronological history of x-ray astronomy missions. In *Handbook of X-ray and Gamma-ray Astrophysics*, page 577. Springer, 2023b.

F Makino and ASTRO-C Team. The x-ray astronomy satellite astro-c. *Astrophysical Letters (ISSN 0004-6388), vol. 25, no. 4, 1987, p. 223-233.*, 25:223–233, 1987.

NE White and A Peacock. The exosat observatory. *Società Astronomica Italiana, Memorie (ISSN 0037-8720), vol. 59, no. 1-2, 1988, p. 7-31.*, 59:7–31, 1988.

Takaya Ohashi, Ken Ebisawa, Yasushi Fukazawa, Kenji Hiyoshi, Michihiro Horii, Yasushi Ikebe, Hitoshi Ikeda, Hajime Inoue, Manabu Ishida, Yoshitaka Ishisaki, et al. The gas imaging spectrometer on board asca. *Publications of the Astronomical Society of Japan*, 48(2):157–170, 1996.

G Manzo, S Giarrusso, A Santangelo, F Ciralli, G Fazio, Santina Piraino, and A Segreto. The high pressure gas scintillation proportional counter on-board the bepposax x-ray astronomy satellite. *Astronomy and Astrophysics Supplement Series*, 122(2): 341–356, 1997.

RE Rothschild, PR Blanco, DE Gruber, WA Heindl, DR MacDonald, DC Marsden, MR Pelling, LR Wayne, and PL Hink. In-flight performance of the high energy x-ray timing experiment on the rossi x-ray timing explorer. *The Astrophysical Journal*, 496(1):538, 1998.

Filippo Frontera, Enrico Costa, Daniele Dal Fiume, Marco Feroci, Luciano Nicastro, M Orlandini, Eliana Palazzi, and Guido Zavattini. Pds experiment on board the bepposax satellite: design and in-flight performance results. In *EUV, X-ray, and Gamma-Ray Instrumentation for Astronomy VIII*, volume 3114, pages 206–215. SPIE, 1997.

Joseph Ladislas Wiza et al. Microchannel plate detectors. *Nucl. Instrum. Methods*, 162(1-3):587–601, 1979.

Richard J. Edgar. *Detectors*, page 23 – 38. Cambridge Observing Handbooks for Research Astronomers. Cambridge University Press, 2011.

Richard L. Kelley, Kazuhisa Mitsuda, Christine A. Allen, Petar Arsenovic, Michael D. Audley, Thomas G. Bialas, Kevin R. Boyce, Robert F. Boyle, Susan R. Breon, Gregory V. Brown, Jean Cottam, Michael J. DiPirro, Ryuichi Fujimoto, Tae Furusho, Keith C. Gendreau, Gene G. Gochar, Oscar Gonzalez, Masayuki Hirabayashi, Stephen S. Holt, Hajime Inoue, Manabu Ishida, Yoshitaka Ishisaki, Carol S. Jones, Ritva Keski-Kuha, Caroline A. Kilbourne, Dan McCammon, Umeyo Morita, S. Harvey Moseley, Brent Mott, Katsuhiro Narasaki, Yoshiaki Ogawara, Takaya Ohashi, Naomi Ota, John S. Panek, F. Scott Porter, Aristides Serlemitsos, Peter J. Shirron, Gary A. Sneiderman, Andrew E. Szymkowiak, Yoh Takei, June L. Tveekrem, Stephen M. Volz, Mikio Yamamoto, and Noriko Y. Yamasaki. The Suzaku High Resolution X-Ray Spectrometer. *Publications of the Astronomical Society of Japan*, 59(sp1):S77–S112, 01 2007. ISSN 0004-6264. doi: 10.1093/pasj/59.sp1.S77. URL https://doi.org/10.1093/pasj/59.sp1.S77.

Emilio Gatti and Pavel Rehak. Semiconductor drift chamber—an application of a novel charge transport scheme. *Nuclear Instruments and Methods in Physics Research*, 225(3):608–614, 1984.

Pavel Rehak, Emilio Gatti, Antonio Longoni, J Kemmer, Peter Holl, Robert Klanner, Gerhard Lutz, and Andrew Wylie. Semiconductor drift chambers for position and energy measurements. *Nuclear Instruments and Methods in Physics Research Section A: Accelerators, Spectrometers, Detectors and Associated Equipment*, 235(2):224–234, 1985.

Gianluigi Zampa, Alexander Rashevsky, and Andrea Vacchi. The x-ray spectroscopic performance of a very large area silicon drift detector. *IEEE Transactions on Nuclear Science*, 56(3):832–835, 2009.

A Rashevsky, V Bonvicini, P Burger, P Cerello, E Crescio, P Giubellino, R Hernández-Montoya, A Kolojvari, LM Montano, D Nouais, et al. Characteristics of the alice silicon drift detector. *Nuclear Instruments and Methods in Physics Research Section A: Accelerators, Spectrometers, Detectors and Associated Equipment*, 461(1-3): 133–138, 2001.

A. Rashevsky, V. Bonvicini, P. Burger, S. Piano, C. Piemonte, and A. Vacchi. Large area silicon drift detector for the alice experiment. *Nuclear Instruments and Methods in Physics Research Section A: Accelerators, Spectrometers, Detectors and Associated Equipment*, 485(1):54–60, 2002. ISSN 0168-9002. doi: https:

//doi.org/10.1016/S0168-9002(02)00531-4. URL https://www.sciencedirect.com/science/article/pii/S0168900202005314. Proceedings of the 5th International Conference on Large Scale Ap plications and Radiation Hardness of Semiconductor Detectors.

A Rachevski, G Zampa, N Zampa, R Campana, Y Evangelista, Gabriele Giacomini, Antonino Picciotto, Pierluigi Bellutti, M Feroci, C Labanti, et al. Large-area linear silicon drift detector design for x-ray experiments. *Journal of Instrumentation*, 9 (07):P07014, 2014.

SA Hoffman, DJ Thiel, and DH Bilderback. Developments in tapered monocapillary and polycapillary glass x-ray concentrators. *Nuclear Instruments and Methods in Physics Research Section A: Accelerators, Spectrometers, Detectors and Associated Equipment*, 347(1-3):384–389, 1994.

MA Kumakhov and FF Komarov. Multiple reflection from surface x-ray optics. *Physics reports*, 191(5):289–350, 1990.

Valentin Viktorovich Lider. X-ray fluorescence imaging. *Physics-Uspekhi*, 61(10):980, 2018.

J.G. Ables. Fourier transform photography: a new method for x-ray astronomy. *Publications of the Astronomical Society of Australia*, 1(4):172–173, 1968.

R.H. Dicke. Scatter-hole cameras for x-rays and gamma rays. *Astrophysical Journal, vol. 153, p. L101*, 153:L101, 1968.

Hans Wolter. Spiegelsysteme streifenden einfalls als abbildende optiken für röntgenstrahlen. *Annalen der Physik*, 445(1-2):94–114, 1952.

Riccardo Giacconi and Bruno Rossi. A "telescope" for soft x-ray astronomy. *Journal of Geophysical Research*, 65(2):773–775, 1960.

Koji Mori, Hiroshi Tomida, Hiroshi Nakajima, Takashi Okajima, Hirofumi Noda, Takaaki Tanaka, Hiroyuki Uchida, Kouichi Hagino, Shogo Benjamin Kobayashi, Hiromasa Suzuki, et al. Xtend, the soft x-ray imaging telescope for the x-ray imaging and spectroscopy mission (xrism). In *Space Telescopes and Instrumentation 2022: Ultraviolet to Gamma Ray*, volume 12181, pages 431–441. SPIE, 2022.

MC Weisskopf, B Brinkman, C Canizares, G Garmire, S Murray, and LP Van Speybroeck. An overview of the performance and scientific results from the chandra x-ray observatory. *Publications of the Astronomical Society of the Pacific*, 114(791): 1, 2002.

Fiona A Harrison, Steve Boggs, Finn Christensen, William Craig, Charles Hailey, Daniel Stern, William Zhang, Lorella Angelini, Hongjun An, Varun Bhalerao, et al. The nuclear spectroscopic telescope array (nustar). In *Space Telescopes and Instrumentation 2010: Ultraviolet to Gamma Ray*, volume 7732, pages 189–196. SPIE, 2010.

Herbert Friedman, SW Lichtman, and ET Byram. Photon counter measurements of solar x-rays and extreme ultraviolet light. *Physical Review*, 83(5):1025, 1951.

R Giacconi, H Gursky, et al. *X-ray astronomy*. Springer, 1974.

Andrea Santangelo, Rosalia Madonia, and Santina Piraino. A chronological history of x-ray astronomy missions. In *Handbook of X-ray and Gamma-ray Astrophysics*, pages 44–51. Springer, 2023c.

Victor Francis Hess. ü ber beobachtungen der durchdringenden strahlung bei sieben freiballonfahrten. *Z. Phys.*, 13:1084, 1912.

George W Clark. Balloon observation of the x-ray spectrum of the crab nebula above 15 kev. *Physical Review Letters*, 14(4):91, 1965.

F Arnold, B Ficht, E Kendziorra, W Pietsch, R Staubert, and J Trümper. Ballonbeobachtungen des crab im röntgenbereich. *Mitteilungen der Astronomischen Gesellschaft, Vol. 35, p. 223*, 35:223, 1974.

R Staubert, E Kendziorra, W Pietsch, RJ Proctor, C Reppin, H Steinle, J Trümper, and W Voges. Hard x-ray balloon observations of compact galactic and extragalactic x-ray sources. *Space Science Reviews*, 30(1):311–323, 1981.

Philip Morrison. Extrasolar x-ray sources. *Annual Review of Astronomy and Astrophysics, vol. 5, p. 325*, 5:325, 1967.

R Giacconi, H Gursky, and LP Van Speybroeck. Observational techniques in x-ray astronomy. *Annual Review of Astronomy and Astrophysics, vol. 6, p. 373*, 6:373, 1968b.

W Forman, C Jones, L Cominsky, P Julien, S Murray, G Peters, H Tananbaum, and R Giacconi. The fourth uhuru catalog of x-ray sources. *Astrophysical Journal, Suppl. Ser., Vol. 38, p. 357-412*, 38:357–412, 1978.

Hans Wolter. Spiegelsysteme streifenden Einfalls als abbildende Optiken für Röntgenstrahlen. *Annalen der Physik*, 445:94–114, 1952.

JE Grindlay, HL Marshall, P Hertz, A Soltan, MC Weisskopf, RF Elsner, P Ghosh, W Darbro, and PG Sutherland. Time-resolved imaging and spectral studies of an x-ray burst from the globular cluster terzan. *Astrophysical Journal, Part 2-Letters to the Editor, vol. 240, Sept. 15, 1980, p. L121-L125.*, 240:L121–L125, 1980.

P Gorenstein, FR Harnden, and DG Fabricant. In orbit performance of the einstein observatory/heao-2 imaging proportional counter. *IEEE Transactions on Nuclear Science*, 28(1):869–874, 1981.

R Giacconi, G Branduardi, U Briel, A Epstein, D Fabricant, E Feigelson, W Forman, P Gorenstein, J Grindlay, H Gursky, et al. The einstein/heao 2/x-ray observatory. *Astrophysical Journal, Part 1, vol. 230, June 1, 1979, p. 540-550.*, 230:540–550, 1979.

SS Holt. Si (li) x-ray astronomical spectroscopy. In *Symp. on the Techniques of Solar and Cosmic X-ray Spectroscopy*, number X-661-75-115, 1975.

Kenneth SK Lum, Claude R Canizares, George W Clark, Joan M Coyne, Thomas H Markert, Pablo J Saez, Mark L Schattenburg, and P Frank Winkler. The spectral archive of cosmic x-ray sources observed by the einstein observatory focal plane crystal spectrometer. *Astrophysical Journal Supplement Series (ISSN 0067-0049), vol. 78, Feb. 1992, p. 423-503.*, 78:423–503, 1992.

Eric M Schlegel. *The restless universe: understanding X-ray astronomy in the age of Chandra and Newton*. Oxford University Press, 2002.

BG Taylor, RD Andresen, A Peacock, and R Zobl. The exosat mission. In *X-Ray Astronomy: Proceedings of the XV ESLAB Symposium held in Amsterdam, The Netherlands, 22–26 June 1981*, pages 479–494. Springer, 1981.

Joachim Trümper. Rosat. *Physica Scripta*, 1984(T7):209, 1984.

Martin C Weisskopf, Harvey D Tananbaum, Leon P Van Speybroeck, and Stephen L O'Dell. Chandra x-ray observatory (cxo): overview. *X-ray optics, instruments, and missions iii*, 4012:2–16, 2000a.

Martin C Weisskopf. Chandra x-ray optics. *Optical Engineering*, 51(1):011013–011013, 2012.

Daniel A Schwartz. The development and scientific impact of the chandra x-ray observatory. *International Journal of Modern Physics D*, 13(07):1239–1247, 2004.

Martin C Weisskopf, J Jeff Hester, Allyn F Tennant, Ronald F Elsner, Norbert S Schulz, Herman L Marshall, Margarita Karovska, Joy S Nichols, Douglas A Swartz,

Jeffery J Kolodziejczak, et al. Discovery of spatial and spectral structure in the x-ray emission from the crab nebula. *The Astrophysical Journal*, 536(2):L81, 2000b.

FK Baganoff, MW Bautz, W Netal Brandt, G Chartas, ED Feigelson, GP Garmire, Y Maeda, M Morris, GR Ricker, LK Townsley, et al. Rapid x-ray flaring from the direction of the supermassive black hole at the galactic centre. *Nature*, 413(6851): 45–48, 2001.

RE Griffiths, A Ptak, ED Feigelson, G Garmire, L Townsley, WN Brandt, R Sambruna, and JN Bregman. Hot plasma and black hole binaries in starburst galaxy m82. *Science*, 290(5495):1325–1328, 2000.

M Pierre, F Pacaud, C Adami, Sinan Alis, B Altieri, N Baran, C Benoist, M Birkinshaw, ANGELA Bongiorno, MN Bremer, et al. The xxl survey-i. scientific motivations-xmm-newton observing plan- follow-up observations and simulation programme. *Astronomy & Astrophysics*, 592:A1, 2016.

H Barré, H Nye, and G Janin. An overview of the xmm observatory system. *ESA Bulletin*, 100:15–20, 1999.

Anil Bhardwaj, Ronald F Elsner, G Randall Gladstone, Thomas E Cravens, Carey M Lisse, Konrad Dennerl, Graziella Branduardi-Raymont, Bradford J Wargelin, J Hunter Waite Jr, Ina Robertson, et al. X-rays from solar system objects. *Planetary and Space Science*, 55(9):1135–1189, 2007.

SL Snowden, RF Mushotzky, KD Kuntz, and David S Davis. A catalog of galaxy clusters observed by xmm-newton. *Astronomy & Astrophysics*, 478(2):615–658, 2008.

Makoto Tashiro, Hironori Maejima, Kenichi Toda, Richard Kelley, Lillian Reichenthal, James Lobell, Robert Petre, Matteo Guainazzi, Elisa Costantini, Mark Edison, et al. Concept of the x-ray astronomy recovery mission. In *Space telescopes and instrumentation 2018: ultraviolet to gamma ray*, volume 10699, pages 520–531. SPIE, 2018.

Makoto Tashiro, Hironori Maejima, Kenichi Toda, Richard Kelley, Lillian Reichenthal, Leslie Hartz, Robert Petre, Brian Williams, Matteo Guainazzi, Elisa Costantini, et al. Status of x-ray imaging and spectroscopy mission (xrism). In *Space Telescopes and Instrumentation 2020: Ultraviolet to Gamma Ray*, volume 11444, pages 293–303. SPIE, 2020.

Makoto S Tashiro. Xrism: X-ray imaging and spectroscopy mission. *International Journal of Modern Physics D*, 31(02):2230001, 2022.

Yoshitaka Ishisaki, Richard L Kelley, Hisamitsu Awaki, Jesus C Balleza, Kim R Barnstable, Thomas G Bialas, Rozenn Boissay-Malaquin, Gregory V Brown, Edgar R Canavan, Renata S Cumbee, et al. Status of resolve instrument onboard x-ray imaging and spectroscopy mission (xrism). In *Space Telescopes and Instrumentation 2022: Ultraviolet to Gamma Ray*, volume 12181, pages 409–430. SPIE, 2022.

Kirpal Nandra, Didier Barret, Xavier Barcons, Andy Fabian, Jan-Willem den Herder, Luigi Piro, Mike Watson, Christophe Adami, James Aird, Jose Manuel Afonso, et al. The hot and energetic universe: A white paper presenting the science theme motivating the athena+ mission. *arXiv preprint arXiv:1306.2307*, 2013.

Marcos Bavdaz, Eric Wille, Mark Ayre, Ivo Ferreira, Brian Shortt, Sebastiaan Fransen, Mark Millinger, Maximilien J Collon, Giuseppe Vacanti, M Barrière, et al. The athena x-ray optics development and accommodation. In *International Conference on Space Optics—ICSO 2020*, volume 11852, pages 842–857. SPIE, 2021.

Xavier Barcons, Didier Barret, A Decourchelle, JW den Herder, Andrew C Fabian, H Matsumoto, D Lumb, K Nandra, LUIGI Piro, RK Smith, et al. Athena: Esa's x-ray observatory for the late 2020s. *Astronomische Nachrichten*, 338(2-3):153–158, 2017.

Yong Chen, WeiWei Cui, Wei Li, Juan Wang, YuPeng Xu, FangJun Lu, YuSa Wang, TianXiang Chen, DaWei Han, Wei Hu, et al. The low energy x-ray telescope (le) onboard the insight-hxmt astronomy satellite. *Science China Physics, Mechanics & Astronomy*, 63:1–13, 2020.

XueLei Cao, WeiChun Jiang, Bin Meng, WanChang Zhang, Tao Luo, Sheng Yang, ChunLei Zhang, YuDong Gu, Liang Sun, XiaoJing Liu, et al. The medium energy x-ray telescope (me) onboard the insight-hxmt astronomy satellite. *Science China Physics, Mechanics & Astronomy*, 63:1–14, 2020.

CongZhan Liu, YiFei Zhang, XuFang Li, XueFeng Lu, Zhi Chang, ZhengWei Li, AiMei Zhang, YongJie Jin, HuiMing Yu, Zhao Zhang, et al. The high energy x-ray telescope (he) onboard the insight-hxmt astronomy satellite. *Science China Physics, Mechanics & Astronomy*, 63:1–15, 2020.

Paul S Ray, Peter WA Roming, Andrea Argan, Zaven Arzoumanian, David R Ballantyne, Slavko Bogdanov, Valter Bonvicini, Terri J Brandt, Michal Bursa, Edward M Cackett, et al. Strobe-x mission overview. *arXiv preprint arXiv:2410.08342*, 2024.

Ronald A Remillard, Margarita Hernanz, Jean in' t Zand, Paul S Ray, Valter Bonvicini, Søren Brandt, Terri Brandt, Alex Carmona, Yuri Evangelista, Daniel Alvarez Franco,

et al. The strobe-x wide field monitor instrument. *Journal of Astronomical Telescopes, Instruments, and Systems*, 10(4):042505–042505, 2024.

Keith C Gendreau, Dominic Maes, Ronald A Remillard, Paul S Ray, Zaven Arzoumanian, Craig Markwardt, and Takashi Okajima. Strobe-x low-energy modular array (lema) instrument. *Journal of Astronomical Telescopes, Instruments, and Systems*, 10(4):042506–042506, 2024.

National Research Council, Division on Engineering, Physical Sciences, Board on Physics, and Committee on the Physics of the Universe. *Connecting quarks with the cosmos: eleven science questions for the new century*. National Academies Press, 2003.

E Haseltine. The 11 greatest unanswered questions of physics. *DISCOVER-NEW YORK-*, 23(2):36–43, 2002.

Kenji Fukushima and Tetsuo Hatsuda. The phase diagram of dense qcd. *Reports on Progress in Physics*, 74(1):014001, 2010.

Hao Tong. Pulsar braking: magnetodipole vs. wind. *Science China Physics, Mechanics & Astronomy*, 59:1–12, 2016.

M. Feroci, J. W. den Herder, E. Bozzo, D. Barret, S. Brandt, M. Hernanz, M. van der Klis, M. Pohl, A. Santangelo, L. Stella, A. Watts, J. Wilms, Zane, et al. LOFT: the Large Observatory For X-ray Timing. In Tadayuki Takahashi, Stephen S. Murray, and Jan-Willem A. den Herder, editors, *Space Telescopes and Instrumentation 2012: Ultraviolet to Gamma Ray*, volume 8443, page 84432D, September 2012. doi: 10.1117/12.926310.

Shuang-Nan Zhang, Andrea Santangelo, Yupeng Xu, Marco Feroci, Margarita Hernanz, Fangjun Lu, Yong Chen, Hua Feng, Kirpal Nandra, Weichun Jiang, et al. Enhanced x-ray timing and polarimetry mission: extp: an update on its scientific cases, mission profile and development status. In *Space Telescopes and Instrumentation 2022: Ultraviolet to Gamma Ray*, volume 12181, pages 466–495. SPIE, 2022.

O Citterio, G Conti, E Mattaini, B Sacco, and E Santambrogio. Optics for x-ray concentrators on board of the astronomy satellite sax. In *X-ray instrumentation in astronomy*, volume 597, pages 102–110. SPIE, 1986.

David N Burrows, JE Hill, JAea Nousek, JA Kennea, A Wells, JP Osborne, AF Abbey, A Beardmore, K Mukerjee, ADT Short, et al. The swift x-ray telescope. *Space science reviews*, 120:165–195, 2005.

Peter Predehl, Robert Andritschke, Werner Becker, Walter Bornemann, Heinrich Bräuninger, Hermann Brunner, Thomas Boller, Vadim Burwitz, Wolfgang Burkert, Nicolas Clerc, et al. erosita on srg. In *Space Telescopes and Instrumentation 2014: Ultraviolet to Gamma Ray*, volume 9144, pages 532–537. SPIE, 2014.

Mikhail Pavlinsky, V Akimov, V Levin, I Lapshov, A Tkachenko, N Semena, M Buntov, A Glushenko, V Arefiev, A Yaskovich, et al. Status of art-xc/srg instrument. In *Space Telescopes and Instrumentation 2014: Ultraviolet to Gamma Ray*, volume 9144, pages 538–548. SPIE, 2014.

BD Ramsey. Optics for the imaging x-ray polarimetry explorer. In *Optics for EUV, X-Ray, and Gamma-Ray Astronomy VIII*, volume 10399, pages 40–49. SPIE, 2017.

W Yuan, C Zhang, Y Chen, SL Sun, YH Zhang, et al. Scientia sinica physica. *Mechanica & Astronomica*, 48(3):039502, 2018.

Yuan Jin, Xin Feng, Duo Li, Jiadai Xue, Bo Wang, Yanji Yang, and Fei Ding. Full aperture super-smooth polishing and surface topology evolution of the mandrels for x-ray optics used in extp mission. *Optik*, 218:165022, 2020.

A Altmann, T Bechteler, R Strecker, P Lechner, R Andritschke, G Hauser, C Fiorini, and K Nandra. Silicon drift detectors for the spectroscopy focusing array of extp. In *Space Telescopes and Instrumentation 2024: Ultraviolet to Gamma Ray*, volume 13093, pages 1879–1887. SPIE, 2024.

Ronaldo Bellazzini, Franco Angelini, Luca Baldini, Alessandro Brez, Enrico Costa, Giuseppe Di Persio, Luca Latronico, MM Massai, Nicola Omodei, Luigi Pacciani, et al. Novel gaseous x-ray polarimeter: data analysis and simulation. In *Polarimetry in Astronomy*, volume 4843, pages 383–393. SPIE, 2003.

Fabio Muleri et al. The Gas Pixel Detector as an X-ray photoelectric polarimeter with a large field of view. *Proc. SPIE Int. Soc. Opt. Eng.*, 7011:70112A, 2008. doi: 10.1117/12.789621.

Ronaldo Bellazzini, Alessandro Brez, Enrico Costa, Massimo Minuti, Fabio Muleri, Michele Pinchera, Alda Rubini, Paolo Soffitta, and Gloria Spandre. Photoelectric x-ray polarimetry with gas pixel detectors. *Nuclear Instruments and Methods in Physics Research Section A: Accelerators, Spectrometers, Detectors and Associated Equipment*, 720:173–177, 2013.

Enrico Costa, Paolo Soffitta, Ronaldo Bellazzini, Alessandro Brez, Nicholas Lumb, and Gloria Spandre. An efficient photoelectric x-ray polarimeter for the study of black holes and neutron stars. *Nature*, 411(6838):662–665, 2001.

Ronaldo Bellazzini, Franco Angelini, Luca Baldini, F Bitti, A Brez, M Ceccanti, L Latronico, MM Massai, M Minuti, N Omodei, et al. Reading a gem with a vlsi pixel asic used as a direct charge collecting anode. *Nuclear Instruments and Methods in Physics Research Section A: Accelerators, Spectrometers, Detectors and Associated Equipment*, 535(1-2):477–484, 2004.

R Bellazzini, G Spandre, M Minuti, Luca Baldini, A Brez, F Cavalca, L Latronico, N Omodei, MM Massai, C Sgro, et al. Direct reading of charge multipliers with a self-triggering cmos analog chip with 105 k pixels at 50 $\mu$m pitch. *Nuclear Instruments and Methods in Physics Research Section A: Accelerators, Spectrometers, Detectors and Associated Equipment*, 566(2):552–562, 2006.

M Hernanz, S Brandt, M Feroci, P Orleansky, A Santangelo, S Schanne, Xin Wu, SN Zhang, YP Xu, E Bozzo, et al. The wide field monitor onboard the extp mission. In *Space Telescopes and Instrumentation 2018: Ultraviolet to Gamma Ray*, volume 10699, pages 1044–1059. SPIE, 2018.

Margarita Hernanz, Søren Brandt, Yuri Evangelista, Aline Meuris, Chris Tenzer, Gianluigi Zampa, Piotr Orleanski, Emrah Kalemci, Müberra Sungur, Stéphane Schanne, et al. The wide field monitor onboard the chinese-european x-ray mission extp. In *Space Telescopes and Instrumentation 2022: Ultraviolet to Gamma Ray*, volume 12181, pages 484–497. SPIE, 2022.

Margarita Hernanz, Marco Feroci, Yuri Evangelista, Aline Meuris, Stéphane Schanne, Gianluigi Zampa, Chris Tenzer, Jörg Bayer, Witold Nowosielski, Malgorzata Michalska, et al. The wide field monitor (wfm) of the china-europe extp (enhanced x-ray timing and polarimetry) mission. In *Space Telescopes and Instrumentation 2024: Ultraviolet to Gamma Ray*, volume 13093, pages 611–625. SPIE, 2024.

Marco Feroci, Giovanni Ambrosi, Filippo Ambrosino, Matias Antonelli, Andrea Argan, Viktor Babinec, Marco Barbera, Joerg Bayer, Pierluigi Bellutti, Bruna Bertucci, et al. The large area detector onboard the extp mission. In *Space Telescopes and Instrumentation 2022: Ultraviolet to Gamma Ray*, volume 12181, pages 466–483. SPIE, 2022.

A Rachevski, M Antonelli, P Bellutti, V Bonvicini, G Borghi, R Campana, F Ceraudo, D Cirrincione, E Del Monte, Y Evangelista, et al. eXTP large area detector: Qualification procedure of the mass production. *Nuclear Instruments and Methods in Physics Research Section A: Accelerators, Spectrometers, Detectors and Associated Equipment*, 1046:167750, 2023.

Zijian Zhao, Tao Luo, Francesco Ceraudo, Marco Feroci, Longhui Li, Jian Wang, Yupeng Xu, Hongwei Liu, Yuxuan Zhu, Yifan Zhang, et al. Characterization of the extp-lad collimators. *Experimental Astronomy*, 57(3):29, 2024.

Søren Brandt, M Hernanz, L Alvarez, P Azzarello, D Barret, E Bozzo, Carl Budtz-Jørgensen, R Campana, E Del Monte, I Donnarumma, et al. The loft wide field monitor. In *Space Telescopes and Instrumentation 2012: Ultraviolet to Gamma Ray*, volume 8443, pages 721–734. SPIE, 2012.

R. Campana, Y. Evangelista, F. Fuschino, M. Ahangarianabhari, D. Macera, G. Bertuccio, M. Grassi, C. Labanti, M. Marisaldi, P. Malcovati, A. Rachevski, G. Zampa, N. Zampa, L. Andreani, G. Baldazzi, E. Del Monte, Y. Favre, M. Feroci, F. Muleri, I. Rashevskaya, A. Vacchi, F. Ficorella, G. Giacomini, A. Picciotto, and M. Zuffa. Characterization of the VEGA ASIC coupled to large area position-sensitive Silicon Drift Detectors. *Journal of Instrumentation*, 9(8):P08008, August 2014. doi: 10.1088/1748-0221/9/08/P08008.

D Baudin, O Limousin, O Gevin, A Meuris, K Altenmüller, P Bausson, F Ceraudo, X Coppolani, D Maier, C Passeron, et al. IDeF-X HDBD: low-noise ASIC for imaging spectroscopy with semiconductor detectors in space science applications. *IEEE Transactions on Nuclear Science*, 69(3):620–626, 2022.

Florent Bouyjou, Olivier Gevin, Olivier Limousin, and Eric Delagnes. A 32-channel 13-b ADC for space applications. *IEEE Transactions on Nuclear Science*, 64(4): 1071–1079, 2017.

Hao Xiong, Jörg Bayer, Andrea Santangelo, Marco Feroci, Ettore Del Monte, Alejandro Guzman, Paul Hedderman, Gabriele Minervini, Samuel Pliego, Andreas Putz, et al. Preliminary design and development of the module back-end electronics for the large area detector onboard the extp mission. *Experimental Astronomy*, 59(1):1, 2025.

G Lombardi, V Mendes, A Trois, G Morgante, F Ceraudo, and R Piazzolla. The thermo-mechanical design of the module of the lad instrument onboard the extp mission. In *Space Telescopes and Instrumentation 2022: Ultraviolet to Gamma Ray*, volume 12181, pages 1690–1717. SPIE, 2022.

Ugo Lo Cicero, Marco Barbera, Nicola Montinaro, Fabio D' Anca, Michela Todaro, Elena Puccio, Luisa Sciortino, Filippo Ambrosino, Riccardo Campana, Tianxiang Chen, et al. Filters design and characterization for lad instrument onboard extp. In *Space Telescopes and Instrumentation 2022: Ultraviolet to Gamma Ray*, volume 12181, pages 1640–1653. SPIE, 2022.

Barry Richard. Freertos, 2025. URL https://www.freertos.org/.

S Zane, D Walton, T Kennedy, M Feroci, J-W Den Herder, M Ahangarianabhari, A Argan, P Azzarello, G Baldazzi, D Barret, et al. A large area detector proposed for the large observatory for x-ray timing (loft). In *Space Telescopes and Instrumentation 2012: Ultraviolet to Gamma Ray*, volume 8443, pages 706–720. SPIE, 2012.

Microchip. Samrh71 rad-hard 32-bit arm® cortex®-m7, microcontroller for aerospace applications, complete data sheet, ds60001593h, 2022.

# List of Figures

# List of Tables